Universidad Carlos III de Madrid

Escuela Politécnica Superior

A numerical study on the aerodynamic forces and the wake stability of flapping flight at low Reynolds number

Tesis Doctoral

Autor
Manuel Moriche Guerrero

Directores
Óscar Flores Arias
Manuel García-Villalba Navaridas

Dpto. de Bioingenería e Ingeniería Aeroespacial

Leganés, Febrero 2017

Dpto. de Bioingenería e Ingeniería Aeroespacial
Escuela Politécnica Superior

A numerical study on the aerodynamic forces and the wake stability of flapping flight at low Reynolds number

Autor
Manuel Moriche Guerrero

Directores de Tesis
Óscar Flores Arias
Manuel García-Villalba Navaridas

Leganés, Febrero 2017

A mi padre, a mi madre, a mi hermano y a Vero.
Esto es tan vuestro como mío.

Tesis doctoral

A numerical study on the aerodynamic forces and the wake stability of flapping flight at low Reynolds number

Autor: Manuel Moriche Guerrero

Directores de Tesis: Óscar Flores Arias, Manuel García-Villalba Navaridas

Firma del Tribunal Calificador:

Firma

Presidente: Ramón Fernández Feria

Secretario: Javier Rodríguez Rodríguez

Vocal: Jan Wissink

Calificación:

Leganés, 17 de Febrero de 2017

I'm afraid that the following syllogism may be used by some in the future.

Turing believes machines think
Turing lies with men
Therefore machines do not think

Yours in distress,

Alan

Abstract

The unsteady aerodynamics that govern flapping flight at low Reynolds number are not yet properly understood. This means that air vehicles that use flapping wings to generate both thrust and lift do not show the desired performance. Many works on the aerodynamic forces of flapping airfoils can be found in the literature, but still our capability to predict these forces is limited. Most of these studies focus on flapping airfoils, assuming infinite aspect ratio wings and Two Dimensional (2D) flow. To what extent the 2D assumption is valid is uncertain. Furthermore, a very few studies address the effect that Three Dimensional (3D) flow structures originated by flow instabilities in infinite aspect ratio wings have on the aerodynamic forces.

In this work we present Direct Numerical Simulations of heaving and pitching airfoils at low Reynolds number where the airfoil motion is prescribed by sinusoidal laws. The parameter space of this problem is huge, so only the mean pitch angle and the phase shift between the heaving and pitching motions are modified. We generate a database of 18 cases and analyze the integrated values of thrust and lift of each case. Also, a reference case is selected to perform a detailed analysis of the forces and decompose the total aerodynamic force in contributions from body motion, vorticity within the flow and surface vorticity. This analysis is extended to a subset of cases from the database in order to study the influence of the motion parameters on the aerodynamic forces. After that, we proceed to estimate the aerodynamic forces by existing models from the literature and, based on observations made through this work, we propose a modification to increase the accuracy of the predicted forces. Finally, we compute the total aerodynamic force as the combination of the contribution from body motion and vorticity within the flow, neglecting surface vorticity effects. This proposed model shows remarkable results for the prediction of thrust and good results for the lift.

After analyzing the aerodynamic forces of the 2D cases, we proceed to study the three-dimensionality of the flow of part of the database. First, we present a stability analysis of four of the cases from the database. Each case is studied by Floquet stability analysis. The four cases considered display different wake structures resulting in different mean aerodynamic forces. Two cases produce thrust and lift, one case only thrust (with symmetric heaving and pitching) and the remaining case mainly lift (with the highest mean pitch angle). In addition, the latter case displays a period doubling phenomenon, and it is found to be linearly unstable for long wavelengths, with an instability mode

that resembles that of mode A found in the wake of cylinders. Other cases, although being linearly stable, present a convective instability at smaller wavelengths. Finally, the unstable case has been studied with a fully 3D DNS to evaluate the effect of the three-dimensionality on the forces. The resulting flow structure is consistent with the linear stability analysis in the near wake. Further downstream nonlinearities lead to a fully 3D wake. Despite this, the aerodynamic forces on the 3D wing are very similar to those obtained in the 2D simulation.

Resumen

La aerodinámica no estacionaria que gobierna el vuelo de alas batientes a bajo número de Reynolds todavía no se entiende correctamente. Esto significa que los vehículos aéreos que usan alas batientes para generar empuje y sustentación no consiguen el rendimiento deseado. En la literatura, se pueden encontrar muchos trabajos sobre fuerzas aerodinámicas en perfiles batientes, pero aún así nuestra capacidad para predecir estas fuerzas es limitada. La mayoría de estos estudios se centran en perfiles, asumiendo un ala de relación de aspecto infinito y flujo bidimensional (2D). El rango de validez de la hipótesis 2D es es incierto. Además, muy pocos estudios abordan el efecto que tienen las estructuras tridimensionales (3D) originadas por inestabilidades del flujo en alas de relación de aspecto infinito sobre las fuerzas aerodinámicas. En este trabajo presentamos simulaciones numéricas directas de perfiles batientes a bajo número de Reynolds donde el movimiento del perfil aerodinámico es prescrito por leyes sinusoidales. El espacio de paramétrico de este problema es enorme, por lo que sólo se modifican el ángulo de ataque medio y la diferencia de fase entre los movimientos vertical y de cabeceo. Generamos una base de datos de 18 casos y analizamos los valores medios de empuje y sustentación para cada caso. También se selecciona un caso de referencia para realizar un análisis detallado de las fuerzas y, además, descomponer la fuerza aerodinámica total en las contribuciones de movimiento del cuerpo, de vorticidad contenida en el flujo y de vorticidad superficial. Este análisis se extiende a un subconjunto de casos de la base de datos con el fin de estudiar la influencia de los parámetros de movimiento sobre las fuerzas aerodinámicas. Posteriormente, se procede a estimar las fuerzas aerodinámicas por modelos de orden reducido presentes en la literatura y, a basándones en observaciones realizadas en este trabajo, se propone una modificación para aumentar la precisión de las fuerzas obtenidas. Finalmente, se calcula la fuerza aerodinámica total como la suma de la contribución de movimiento del cuerpo y de vorticidad contenida en el flujo, sin considerar efectos de la vorticidad superficial. Este modelo propuesto muestra resultados notables para la predicción del empuje y buenos resultados para la sustentación.

Contents

Glossary

ρ Density of the fluid

ν Dinaymic viscosity of the fluid

Re Reynolds number

$\mathrm{Re_b}$ Reynolds number based on bulk velocity

k Reduced frequency. $k = 2\,\pi\,f\,c/U_\infty$

St Strouhal number. $St = f\,A/U_\infty$

Δx Mesh width in x direction

Δy Mesh width in y direction

Δz Mesh width in z direction

ΔV Volume associated to a lagrangian marker

δ_h Regularized delta function

κ Unidimensional, continuous function used by the regularized delta function

$\vec{x}$ Position vector in the Eulerian frame

$\vec{X}$ Position vector in the Lagrangian frame

p Pressure field

u_i Component i of the velocity field. $i = x$, y or z

ϕ Pseudo-pressure field

$\vec{u}$ Velocity field vector in the Eulerian frame

$\vec{\omega}$ Vorticity field vector

$\vec{f}$ Volume force vector in the Eulerian frame

$\mathbf{L}$ Linear terms in Navier Stokes equations. $\mathbf{L} = \mathrm{Re}^{-1}\nabla^2\vec{u}$

$\mathbf{N}$ Non-linear terms in Navier Stokes equations. $\mathbf{N} = (\vec{u} \cdot \nabla)\,\vec{u}$

Q Second invariant of the velocity gradient tensor $\nabla \vec{u}$

$\vec{U}$ Velocity field vector in the the Lagrangian frame

$\vec{F}$ Volume force vector in the Lagrangian frame

C Advective velocity for the outflow boundary condition

L_2 Euclidean norm of a vector

$\vec{e}_x$ Unitary vector in x direction

$\vec{e}_y$ Unitary vector in y direction

$\vec{e}_z$ Unitary vector in z direction

t Time

Δt Time step

T Period of the oscillatory motion

T_{av} Time span selected for averaging calculations

L Lift

D Drag

F_x Force per unit length in x direction

F_y Force per unit length in y direction

F_z Force per unit length in z direction

$M_{y,s}$ Pitching moment per unit length at a distance s from the leading edge

W Mechanical work

η Propulsive efficiency defined as the ratio between the propulsive work (output) and the input work $\eta = \frac{W_o}{W_i}$

c_d Non-dimensional drag coefficient per unit length $c_d = \frac{2F_x}{\rho U_\infty{}^2 c}$

c_t Non-dimensional thrust coefficient per unit length $c_t = \frac{-2F_x}{\rho U_\infty{}^2 c}$

c_l Non-dimensional lift coefficient per unit length $c_l = \frac{2F_y}{\rho U_\infty{}^2 c}$

c_f Non-dimensional coefficient per unit length of the modulus of the force $c_f = \sqrt{c_t{}^2 + c_l{}^2}$

C_x Non-dimensional force coefficient in x direction

C_z Non-dimensional force coefficient in z direction

h Vertical displacement of heaving motion

$\dot{h}$ Vertical velocity of heaving motion

$\ddot{h}$ Vertical acceleration of heaving motion

θ Angular displacement of pitching motion

$\dot{\theta}$ Angular velocity of pitching motion

$\ddot{\theta}$ Angular acceleration of pitching motion

f Frequency of oscillation

h_0 Amplitude of heaving motion

θ_m Mean pitch value

θ_0 Amplitude of pitching motion

φ Phase shift between the heaving and pitching motions

x_p Pivoting point location for pitching motion (Distance to the leading edge)

D Cylinder diameter

c Airoil chord

e Airoil thickness

$\vec{n}$ Unitary normal vector pointing towards the fluid

ϵ Thickness ratio of an ellipse. $\epsilon = \frac{\text{minor axis length}}{\text{major axis length}}$

ξ Radial coordinate of elliptic coordinates

η Angular coordinate of elliptic coordinates

S Speed-up in parallel compuations

E Efficiency in parallel computations

t_u Unitary time

N Number of processes participating in a parallel computation

N_G Number of grid points

N_S Number of steps

ϕ_x Auxiliary potential in direction x

ϕ_z Auxiliary potential in direction z

δ_l Lift density

δ_t Thrust density

δ_x Force density in the x direction

δ_z Force density in the z direction

Γ Circulation

α_e Effective angle of attack

U_∞ Free stream velocity

$\vec{U}$ Incoming velocity seen by the airfoil

σ Deviation angle from Kutta-Joukowsky force prediction

G_T Translational coefficient in quasi-steady model for circulation

G_R Rotational coefficient in quasi-steady model for circulation

U_i Velocity of base flow in Floquet analysis

P Pressure of base flow in Floquet analysis

$\hat{\mathbf{u}}$ Vector of spanwise Fourier mode of perturbation velocity

$\hat{u}_i$ Spanwise Fourier mode of perturbation velocity

$\hat{p}$ Spanwise Fourier mode of perturbation pressure

β Spanwise wavenumber of Fourier modes

λ Spanwise wavelength of Fourier mode

μ Floquet multiplier

Operators

This glossary contains the operators used throughout the document. The function X is used as a dummy object.

$\overline{X}$ Mean operator

$X^{\mathbf{rms}}$ Root mean square operator

X^* Component with divergence

X' Fluctuation of a variable variable

ΔX Amplitude of a signal

$B(X)$ Boundary condition function.

X^m Body motion contribution

X^a Added mass contribution

X^v Contribution from vorticity within the flow

X^s Surface vorticity contribution

X_{KJ} Kutta Joukowsky estimation

Acronyms

DARPA Defense Advanced Research Projects Agency

MAV Micro Air Vehicle

HDF5 Hierarquical Data Format version 5

I/O Input/Output tasks

IBM Immersed Boundary Method

DNS Direct Numerical Simulation

MPI Message Parsing Interface

TUCAN Two(Three)-Dimensional Unsteady Code for Aerodynamics in Nature

CFL Courant Fredrich Levy number

rms root mean squared

TE Trailing Edge

LE Leading Edge

TEV Trailing Edge Vortex

LEV Leading Edge Vortex

2D Two Dimensional

3D Three Dimensional

AR Aspect Ratio

Publications

Reviewed articles

Some of the results obtained in this are contained in the following publications that have been published or submitted for publication during the course of this thesis.

Moriche, M., Flores, O., and García-Villalba, M. Generation of thrust and lift with airfoils in plunging and pitching motion. In *J. Phys.: Conf. Ser.*, volume 574, page 012163, 2015

Moriche, M., Flores, O., and García-Villalba, M. Three-dimensional instabilities in the wake of a flapping wing at low Reynolds number. In *Int. J. Heat Fluid Flow*, 2016b

Moriche, M., Flores, O., and García-Villalba, M. On the aerodynamic forces on heaving and pitching airfoils at low Reynolds number. In *J. Fluid Mech.*, 2017, Submitted

Conference presentations

Also, the following talks have been used to spread the progresses made through the period of the thesis.

Moriche, M., Flores, O., and García-Villalba, M. Analysis of the aerodynamivc forces on having and pitching airfoils at low Reynolds number. In *11th European Fluid Mechanics Conference, Sevilla, Spain*, 2016a

Raiola, M., Ianiro, A., Discetti, S., Moriche, M., Flores, O., and García-Villalba, M. Flow over flapping airfoils: qualitative and quantitative comparison between experiments and simulations. In *11th European Fluid Mechanics Conference, Sevilla, Spain*, 2016

Hernández-Hurtado, E., Moriche, M., Flores, O., and García-Villalba, M. The flow around a flapping-wing micro air vehicle in free flight. In *11th European Fluid Mechanics Conference, Sevilla, Spain*, 2016

Moriche, M., Flores, O., and García-Villalba, M. Flapping airfoil simulations at very low Reynolds. In *10th European Fluid Mechanics Conference, Copenhagen, Denmark*, 2014

CHAPTER

ONE

Introduction

1.1 Motivation

Driven by the recent development of Micro Air Vehicles (MAV), unsteady aerodynamics of flapping wings has attracted the interest of the scientific community during the past decades. Defense Advanced Research Projects Agency (DARPA) defines an MAV as an aerial vehicle with no dimension larger than 15cm. Indeed, MAVs operating conditions are similar to those in which insects and small birds fly, so these species can be use as prototypes for the design of flapping wing MAVs. By bio-mimicking birds and insects, their outstanding flight performance could be transferred to MAVs.

Furthermore, the reduced size of MAVs result in favorable scaling characteristics including structural strength, reduced stall speed, and low inertia [Shyy et al., 1999]. Unfortunately, there are some technical limitations in the development of MAVs, namely propulsion systems, navigation and sources of energy at the small scale of these devices. The Reynolds number (Re) of the flow is about 10 to 10^4 and the motion of the wings is characterized by moderate frequencies and high amplitudes [Shyy et al., 2013]. The fundamental difference of this flight regime compared to conventional fixed wing aerodynamics is the low lift to drag ratio, high coupling between fluid and structural dynamics and sensitivity to gusts. A deeper insight in the underlying phenomena of unsteady aerodynamics is a crucial step in the maturation process of MAVs design, a repeated statement in the literature on the aerodynamics of flapping wings as recently reviewed by several authors [Rozhdestvensky and Ryzhov, 2003, Platzer et al., 2008, von Ellenrieder et al., 2008, Shyy et al., 2010, 2013].

1.2 State of the art

The actual mechanisms that occur when birds and insects fly result in an incredibly complex problem. In the case of insects, wings are typically passive membranes with enough stiffness to support the aerodynamic loads, whereas birds have bones and muscles in their wings to actively adapt their shape to the flight conditions [Shyy et al., 1999].

Furthermore, the motion of the wing is a rather complex combination of translations and rotations of a deformable wing in the Three Dimensional (3D) space. For example, insects and hummingbirds are capable of rotating their wings to perform symmetric hover, in which forces are generated in both downstroke and upstroke. In a different manner, birds other than Hummingbirds perform asymmetric hover, generating forces in the downstroke and flexing their wings in the upstroke to avoid negative lift. Thus, in order to face the problem appropriately, scientists simplify the problem in a drastic, but useful manner. Many studies remove the elasticity from the wing structure and reduce the 3D character of the problem to the Two Dimensional (2D) space. This implies that the wing under study is an infinite aspect ratio, rigid wing, and that the flow is 2D. Also, sinusoidal laws are used to impose the motion of the wings. Unfortunately, even with these assumptions, the parameter space to be covered is huge, so the path to fully understand flapping wings flight is daunting.

Numerous authors have studied the problem of a 2D airfoil in pure heaving motion, in which the airfoil oscillates vertically with zero angle of attack [Jones and Platzer, 1997, Wang, 2000, Lewin and Haj-Hariri, 2003, Ashraf et al., 2011, Lua et al., 2007, Wei and Zheng, 2014, Choi et al., 2015, Martín-Alcántara et al., 2015]. Historically, heaving airfoils were regarded as an alternative to rotary propellers for thrust generation. The first authors who gave an explanation of the thrust generation by a flapping airfoil were Knoller [1909] and Betz [1912] in independent studies. Katzmayr [1922] confirmed this phenomena experimentally. Later, linear solutions from Glauert [1930] and Garrick [1937] were scientifically fruitful, but the fact that the maximum propulsive efficiency was obtained for zero frequencies indicated that results were incomplete. With the evolution of computers, the use of unsteady panel methods allowed to increase the complexity of the problem [Jones and Platzer, 1997]. Non-linearities from the actual geometry of airfoils and from wake interactions were included in these models but, still, these methods gave no optimum finite frequency for flapping flight. Direct Numerical Simulation (DNS) was capable of capturing key features of the flow in unsteady aerodynamics, namely the leading and trailing edge vortices. The Leading Edge Vortex (LEV) has been identified as the main lift enhancing mechanism of flapping wings [Ellington et al., 1996]. In steady aerodynamics, the generation of an LEV produces a high lift plateau for a short time span followed by a sudden drop of the aerodynamic force [Carr, 1988]. This process is known as dynamic stall. Flapping wings take advantage of the high lift generated during the formation of the LEV by consecutively generating an LEV in each stroke. With this cyclic mechanism, the wing experiences the high transient lift from the generation of an LEV and avoids entering in the dynamic stall region. Wang [2000] studied a heaving airfoil at $\mathrm{Re} = 1000$ by DNS. She found two conditions for optimal thrust generation. First, the Strouhal number (St) must be high enough to reach high values of the effective angle of attack and, second, the reduced frequency must be low enough for the LEV to

grow. In an extensive numerical analysis on heaving airfoils at Re = 500, Lewin and Haj-Hariri [2003] explain how the interaction between the LEV and the Trailing Edge Vortex (TEV) influences the propulsive efficiency of the airfoil. Although these studies gave insight in the unsteady aerodynamics of flapping flight, thrust values obtained by pure heaving at this Re are very low, so the next natural step was to include a rotation of the airfoil (pitching) as insects and small birds do [Wang, 2000].

If the rotation of the airfoil, or pitching, is considered, the problem is still under the 2D assumption, but the motion of the airfoil resembles that of an actual flapping wing [Anderson et al., 1998, Ashraf et al., 2011, Widmann and Tropea, 2015]. The proper combination of pitching and heaving motions result in a better performance in terms of aerodynamic forces, but introduces new parameters that increase the complexity of the problem. For example, with a mean pitch value in the motion law, the airfoil is capable of generating both thrust and lift. Furthermore, a non-zero pitching amplitude modifies the flow around the airfoil and can, for specific combination of the motion parameters, increase the net value of thrust and the propulsive efficiency. The phase shift between the heaving and pitching motion has a great influence in the aerodynamic force. Anderson et al. [1998] carried out a large number of experiments in which different motion parameters were modified. He observed that if the pitching motion is shifted more than 90° with respect to the heaving (pitching leads heaving), higher thrust is obtained. Dickinson et al. [1999] performed experiments with a robot to study the influence of wing rotation in a flapping motion. They imposed non-sinusoidal motion laws where the rotation of the wing is concentrated at the end of the strokes. They identified that advanced rotation benefits lift generation due to the Magnus effect and that wake capture was indeed used in insect-like flapping flight. So far, the main mechanisms in unsteady aerodynamics of flapping flight have been identified but, unluckily, the simplicity of the problem is being abandoned, so the path to fully understand the underlying physics is still undetermined.

To obtain a deeper insight in the generation of forces by flapping airfoils, several authors have decided to decompose the total aerodynamic force in different contributions [Wang et al., 2014, Martín-Alcántara et al., 2015]. An evaluation of different algorithms to decompose the aerodynamic force can be found in the work of Wang et al. [2014]. They perform DNS of a flat plate (2D) and a rectangular wing (3D) in heaving and pitching motion at Re = 300, pointing out two different aspects that make these algorithms attractive to scientits. First, these algorithms allow experimentalists to circumvent the implicit difficulties related to flow measurements and, second, post-processing data can be enhanced by analyzing each of the contributions to the total force seperately. For example, in an experiment at low Re, pressure fields are not easy to quantify, and also velocity gradients are easier to estimate than vorticity gradients, but the latter decay faster than the former with the distance to the body [Noca et al., 1999]. These

kind of suitability aspects make different algorithms present advantages with respect to others, as studied by Noca et al. [1999], who propose three different algorithms to decompose the total aerodynamic force. For post-processing data, a force decomposition algorithm where the terms have clear representation of underlying physics, is desired. Related to this point, Wang et al. [2014] observed that, in the flow regime they studied, accelerations due to the airfoil (or wing) motion and vortex force were dominant in the force generation process. This result is in agreement with the recent work of Martín-Alcántara et al. [2015], who performed the decomposition algorithm proposed by Chang [1992] on 2D DNS of a heaving airfoil at $\mathrm{Re} = 500$. They also analyzed their results by flow visualization, observing that vortical structures which are a few chords away from the airfoil generate little aerodynamic force.

One of outcomes of a deeper understanding of the underlying phenomena in unsteady aerodynamics is the prediction of forces by simplified algorithms, typically referred as reduced order models. Unfortunately, the flow obtained by large amplitude, moderate frequencies motions at low Re is far from Stokes regime and far from potential theory, so no complete theories are available. DNS is a powerful tool to extract information from flows, but its computational cost make it an inadequate approach to be used in the small computing devices of MAVs. Therefore, many scientists work on simplified models to predict the aerodynamic forces produced by flapping flight. As early as in 1972, Weis-Fogh [1972] proposed a quasi-steady model based in momentum theory under the 2D assumption, which was extended to 3D wings by a coarse blade element theory. Dickinson et al. [1999] extracted simple laws for the lift and drag coefficients in the translational phase of the wing motion based on experiments on a scaled fruit fly. They also identified wing rotation as an important lift enhancing mechanism and quantified its contribution to the mean lift, but no model was proposed about it. Pesavento and Wang [2004] performed DNS of free falling plates and proposed a model for the circulation of a 2D airfoil subjected to large angles of attack and fast rotations. Recently, Taha et al. [2014] proposed a fully unsteady model for the circulation based on Wagner's aerodynamic model. From the models cited above, the work of Pesavento and Wang [2004] is fairly simple (quasi-steady), easily related to underlying physics and gives good results in a highly demanding test for a 2D airfoil. More details about the aerodynamic modelling of flapping airfoils can be found in the review of Ansari et al. [2006] and Taha et al. [2012].

The assumption of two-dimensionality is invalid when the aspect ratio of the wing is small. Thus, there are many studies that investigate three-dimensional effects in the wake of low-aspect-ratio flapping wings [von Ellenrieder et al., 2003, Dong et al., 2006, Visbal et al., 2013]. However, even in the limit of infinite Aspect Ratio (AR), 3D instabilities might develop and lead to modifications of the flow around the airfoil and, consequently, to modifications of the aerodynamic forces. Visbal [2011] performed

3D large eddy simulations of a plunging wing of infinite AR in a broad range of Re ($10^3 \leq \mathrm{Re} \leq 1.2 \cdot 10^5$). Three-dimensional effects were absent at $\mathrm{Re} = 1000$, but clearly present at $\mathrm{Re} = 5000$ and beyond (see his figure 22). Generally, it is therefore assumed that at low Re, (say $\mathrm{Re} < 2000$), the flow is going to remain 2D. Note that in simpler flows the onset of three-dimensionality occurs at a lower Re. For example, for the flow over a fixed circular cylinder 3D effects occur already in the range $\mathrm{Re} \sim 200 - 300$ [Williamson, 1996b]. Hoarau et al. [2003] studied the incompressible flow over a fixed NACA0012 wing at a relatively large angle of attack of 20° and observed three dimensional effects at $\mathrm{Re} = 800$. Considering that in plunging and pitching airfoils the parametric space is very large, it is unclear in which parameter regime the flow actually remains 2D. A suitable tool to predict the onset of 3D instabilities in time-periodic flows is Floquet stability analysis. This method has been used to predict the onset of 3D effects in the flow over a fixed circular cylinder by Barkley and Henderson [1996] and in the flow over a fixed square cylinder by Robichaux et al. [1999]. It has also been employed for the case of flow over oscillating cylinders by Leontini et al. [2007]. Recently, Deng and Caulfield [2015] and Deng et al. [2015] used Floquet stability analysis to study the 3D transition in the wake of a pitching airfoil.

1.3 Objectives

The main goal of this thesis is to increase our knowledge in the unsteady aerodynamics that govern flapping flight at low Re. For that, we set two primary objectives: first, to investigate the aerodynamic forces generated by flapping airfoils and, second, to study the effects of 3D flow structures on infinite AR wings.

To study the forces generated by 2D flapping airfoils we will generate a database of 18 cases. These cases will have different motion parameters in order to characterize their influence on the aerodynamic forces. This database will also be used to analyze how reduced order models can be employed to predict the aerodynamic forces generated in flapping flight. For this purpose, we will use existing models from the literature and include some modifications in order to improve the accuracy of the predicted forces. The results of this part of the thesis can be applied to the control of MAVs, which lack of accurate reduced order models for the prediction of the forces generated during flight.

Regarding the three-dimensionality of infinite AR wings, we seek to isolate the effects of 3D flow instabilities on the aerodynamic forces. Most of the studies in the literature focus on the 3D effects originated by finite wings and there is little published data on the effects of 3D flow instabilities not related with geometric 3D features. This study will serve to define the validity of the widely used 2D assumption in flapping flight. Also, we will analyze how linear stability analysis can be used to predict the stability of the wake in the full non-linear solution of the flow. The nature of this part of the thesis is

more related to fundamental physics than to engineering applications.

Finally, there is one secondary objective originated by the needs of the previously commented primary objectives. We need to develop a computational tool to simulate the flow around moving objects in 2D and 3D. The code needs to be parallel and show an efficient parallel performance in large super computer centers in order to compute high demanding simulations in a reasonable time. The development of this code has some advantages from which we highlight the following: First, the total control of the code allows the research group to take any decision in the direction that benefit its own interests. Second, the implementation of the code implies a deep knowledge of the numerical methods used to represent the physics under study.

1.4 Structure of the document

This thesis is organized as follows. Chapter 2 contains the details of the algorithms used in the code developed in this work and some relevant aspects of its implementation. The validation of the code and data of its performance are shown in chapter 3. In chapter 4 the analysis of the aerodynamic forces of a database of 2D cases is presented. After that, in chapter 5, we apply a decomposition algorithm to analyze the different contributions to the total aerodynamic force of the cases presented in chapter 4. Also, in this chapter, we model the aerodynamic force by using reduced order models. In chapter 6 we explore the effects of 3D flow structures on the aerodynamic forces of infinite AR wings. Finally, some conclusions and proposals for future work are presented in chapter 7.

CHAPTER
TWO

Methodology

This chapter contains the methodology used to develop the code Two(Three)-Dimensional Unsteady Code for Aerodynamics in Nature (TUCAN), which is the tool used to perform the DNS of this work. The chapter has been divided into three parts. The first part is dedicated to describe the equations that govern an incompressible flow. The second deals with the numerical methods implemented in TUCAN and, finally, the third part describes the most relevant aspects of the actual implementation of TUCAN.

2.1 Governing equations

The Mach number of flows around birds and insects is typically 1/300 [Wang, 2005], so the governing equations are the Navier Stokes equations for an incompressible flow

$$\frac{\partial u_i}{\partial x_i} = 0, \tag{2.1a}$$

$$\frac{\partial u_i}{\partial t} + u_j \frac{\partial u_i}{\partial x_j} = -\frac{1}{\rho}\frac{\partial p}{\partial x_i} + \nu \frac{\partial^2 u_i}{\partial x_i^2}, \tag{2.1b}$$

$$B(u_i) = 0 \quad \text{at domain boundaries}, \tag{2.1c}$$

$$u_i = U_i \quad \text{at body surface}, \tag{2.1d}$$

where u_i is the flow velocity, p the pressure, ν the kinematic viscosity of the fluid, ρ the density of the fluid and U_i the velocity of an immersed body. Equation (2.1c) represents the boundary conditions and equation (2.1d) the no-slip condition at the surface of an immersed body. The main advantage of the incompressible flow assumption is the absence of pressure waves propagation, allowing for larger time steps and coarser grids. However, the decoupling of the continuity constraint (equation (2.1a)) with time makes this system of equations cumbersome to solve.

The force exerted by the fluid into a submerged solid is given by

$$\vec{F} = -\int_S p\vec{n}\,\mathrm{d}S + \nu \int_S \vec{\omega} \times \vec{n}\,\mathrm{d}S, \tag{2.2}$$

where S represents the surface of the solid, $\vec{\omega}$ is the flow vorticity and $\vec{n}$ is a unitary normal vector pointing towards the fluid.

Table 2.1: Coefficients of Runge-Kutta scheme

Stage	α	β	γ	ξ
1	4/15	4/15	8/15	0
2	1/15	1/15	5/12	−17/60
3	1/6	1/6	3/4	−5/12

2.2 Numerical methods

In TUCAN equations (2.1) are solved in a two or three dimensional cartesian domain, discretized by a uniform staggered grid. Spatial derivatives are approximated by centered finite differences with second order error convergence and time marching is performed with the low-storage, semi-implicit, three stages Runge-Kutta scheme presented by Rai and Moin [1991], although we use the notation of Spalart et al. [1991]. The only difference between these notations is that the latter allows for different values of the coefficients of the explicit and implicit part of the linear terms time scheme. To overcome the issue of the decoupling of the continuity constraint (equation (2.1a)) with respect to time, we use the fractional step method described by Brown et al. [2001], in which the divergence free velocity $\vec{u}$ is decomposed into the sum of a non-zero divergence velocity $\vec{u}^*$ and the gradient of a potential ϕ, called here pseudo-pressure. The algorithm for the k-th sub-step of the Runge-Kutta scheme is

$$\left(\nabla^2 - \frac{\mathrm{Re}}{\beta_k \Delta t}\right)\vec{u}^* = -\frac{\mathrm{Re}}{\beta_k \Delta t}\left(\vec{u}^{k-1} + \Delta t\left(\alpha_k \mathbf{L}^{k-1} + \gamma_k \mathbf{N}^{k-1} + \xi_k \mathbf{N}^{k-2} - (\alpha_k + \beta_k)\nabla p^{k-1}\right)\right) \tag{2.3a}$$

$$\nabla^2 \phi = \frac{\nabla \cdot \vec{u}^*}{\Delta t(\alpha_k + \beta_k)} \tag{2.3b}$$

$$p^k = p^{k-1} + \phi - \frac{\beta_k \Delta t}{\mathrm{Re}}\nabla^2 \phi \tag{2.3c}$$

$$\vec{u}^k = \vec{u}^* - (\alpha_k + \beta_k)\Delta t \nabla \phi, \tag{2.3d}$$

where α_k, β_k, γ_k and ξ_k are the coefficients of the Runge-Kutta scheme (table 2.1), Δt is the time step for the integration and the linear and non-linear operators are $\mathbf{L} = \mathrm{Re}^{-1}\nabla^2 \vec{u}$ and $\mathbf{N} = (\vec{u} \cdot \nabla)\,\vec{u}$, respectively. For further details of the fractional step method and more pressure projection algorithms, the reader is referred to the work of Brown et al. [2001].

2.2.1 Computational grid

The spatial discretization in TUCAN is done on a structured, uniform, staggered grid. In this type of grids the pressure and the velocity components are calculated in different positions. There are several reasons to use a staggered grid over of a collocated one. First of all, checker board oscillations that typically appear when equation (2.1b) is discretized by second order finite differences on a collocated grid, are eliminated. Also, the relative position of grid points of the different variables is more convenient for the spatial discretization. The cost of these advantages is that the implementation of a staggered grid is more demanding than that of a collocated one. An sketch of the actual implementation of the grid in TUCAN is shown in figure 2.1. The figure shows

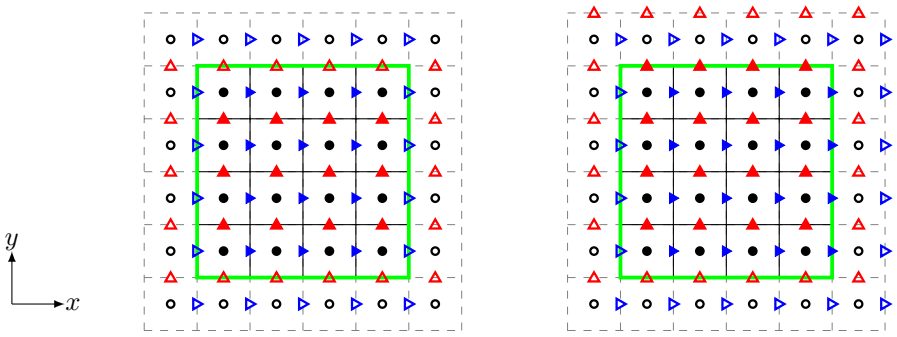

Figure 2.1: Sketch of the uniform staggered grid implemented in TUCAN. Physical boundaries (———) lie on the nodes of the velocity component perpendicular to the boundary. The nodes represented correspond to the streamwise (▶) and vertical (▲) velocities and the pressure (●) grid points.

that physical boundaries lie on nodes of the velocity component perpendicular to the boundary. This configuration is suitable for the typical applications of TUCAN, where Neumann type boundary conditions are set for the psuedo-pressure (calculated at the pressure points), free slip boundary conditions at the south and north boundaries and inflow-outflow boundary conditions at the west and east boundaries, respectively.

Another important aspect of the implementation of TUCAN is the presence of ghost points in the grid. Ghost points are grid points in which the solution is not calculated. Instead, they are used for the computations during execution or when an existing field is used as initial condition. The grid points represented in figure 2.1 by an empty symbol are ghost points.

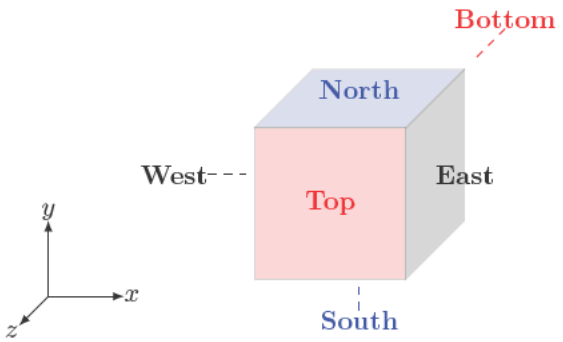

Figure 2.2: Domain boundaries.

2.2.2 Boundary conditions

Different boundary conditions are allowed in TUCAN. Dirichlet, Neumann and periodic type boundary conditions can be set in any of the boundaries.

Also, an advective type boundary condition can be set in the east boundary (see figure 2.2). This type of boundary condition is the natural choice when intense flow structures reach the outlet of the domain by an advection process. In this scenario, either Dirichlet or Neumann type boundary condition at the outlet would produce reflections that can affect the solution of the problem. With an advective type boundary condition at the outlet, flow structures leave the domain minimizing the reflections that can influence the solution. The equation solved at at the outflow boundary when the advective type boundary condition is set is

$$\frac{\partial \vec{u}}{\partial t} + \mathrm{C}\frac{\partial \vec{u}}{\partial x} = 0, \tag{2.4}$$

where C is the advective velocity, taken as constant along the boundary. Equation (2.4) is treated explicitly with the same scheme as the non-linear terms in equation (2.1b). The algorithm for the k-th substep of the Runge-Kutta scheme of the advective type boundary condition is

$$\vec{u}_{\mathrm{E}}^{k} = \vec{u}_{\mathrm{E}}^{k-1} - \Delta t \left(\gamma_k \, \mathrm{C}^{k-1} \left.\frac{\partial \vec{u}}{\partial x}\right|_E^{k-1} + \xi_k \, \mathrm{C}^{k-2} \left.\frac{\partial \vec{u}}{\partial x}\right|_E^{k-2} \right), \tag{2.5}$$

where the subscript E indicates that the term is evaluated at the east boundary and the right bar indicates that the appropriate discretization is performed. The spatial derivatives that appear in (2.5) are approximated by centered finite differences in the case of the x component of the velocity and by uncentered finite differences in the case of the other velocity components.

If periodic boundary conditions are used, the grid points that need to be calculated are different to those when Diritchlet or Neumann boundary conditions are used. Figure

2.1b shows the layout of the staggered grid when periodic boundary conditions are set in both x and y directions.

2.2.3 Submerged bodies

The previous section describes the algorithms used to solve Navier-Stokes equations without considering the presence of bodies in the flow. In this section we describe how the presence of bodies is modelled in TUCAN. There are many possibilities to simulate the flow around moving bodies, which, as expected, show different advantages and disadvantages if we compare them. In order to chose the appropriate algorithm to model the presence of bodies in the flow, one must find the compromised solution which better suits the problem under study. At the low Re of flapping flight, the Immersed Boundary Method (IBM) presents clear advantages compared to body-fitted algorithms. The cost associated with the size of the grid needed when using an IBM compensates the cost of remeshing and interpolating tasks in body-fitted grids. For more details of the IBM the reader is referred to the review of Mittal and Iaccarino [2005].

In TUCAN the presence of the body is modelled with the dircect forcing IBM proposed by Uhlmann [2005]. In this particular algorithm the flow is solved in the Eulerian frame and the no-slip boundary condition is not directly imposed, but enforced with an additional term in the right hand side of the momentum equation in Navier-Stokes. The algorithm can be summarized in the following steps:

1. Make an explicit estimation of the flow velocity $\vec{u}^e$ in the Eulerian frame.
2. Interpolate the estimated velocity $\vec{u}^e$ from the Eulerian frame to the Lagrangian frame to obtain the estimated velocity $\vec{U}^e$ at the Lagrangian points.
3. Calculate the forcing term $\vec{F}$ required to obtain the desired velocity $\vec{U}^d$ in order to fulfill the no-slip condition at every Lagrangian point.
4. Spread the forcing term $\vec{F}$ from the Lagrangian frame to the Eulerian frame to obtain the distributed volume force $\vec{f}$.
5. Solve Navier Stokes equations with the addition of the volume force $\vec{f}$ to the right hand side of the momentum equation.

The Eulerian and Lagrangian frames interact with each other via a regularized delta function δ_h. This regularized delta function is a discrete version of the Dirac's delta and was first introduced by Peskin [2002]. The regularized delta for two-dimensional problems is given by

$$\delta_h = \frac{1}{h^2}\kappa\left(\frac{r_x}{h}\right)\kappa\left(\frac{r_y}{h}\right), \tag{2.6}$$

where $\vec{r}_{ij,l} = r_x\vec{e}_x + r_y\vec{e}_y$ is the relative position vector of the Eulerian point $\vec{x}_{ij}$ with respect to the Lagrangian $\vec{X}_l$, h is the mesh width and the function κ is a continuous function which is built according to some constraints. The mesh width h must be equal in every cartesian coordinate ($h = \Delta x = \Delta y$). One of the main characteristics of the function κ is its scope, which is defined as the minimum number of grid points influenced by the function δ_h. In TUCAN there is one function κ implemented for a scope of 3 points and one for a scope of 4 points. For a scope of 3 points we use the function κ given by Roma et al. [1999]

$$\kappa(r) = \begin{cases} \frac{1}{3}\left(1 + \sqrt{-3r^2+1}\right) & \text{if} \quad |r| < 0.5 \\ \frac{1}{6}\left(5 + 3r - \sqrt{-3(1-|r|)^2+1}\right) & \text{if} \quad 0.5 \leq |r| < 1.5 \\ 0 & \text{if} \quad 1.5 \leq |r| \end{cases}, \tag{2.7}$$

and for a scope of 4 points, the one given by Peskin [2002]

$$\kappa(r) = \begin{cases} \frac{1}{8}\left(5 + 2r - \sqrt{-7-12r-4r^2}\right) & \text{if} \quad |r| < 1 \\ \frac{1}{8}\left(3 + 2r + \sqrt{1-4r-4r^2}\right) & \text{if} \quad 1 \leq |r| < 2 \\ 0 & \text{if} \quad 2 \leq |r| \end{cases}. \tag{2.8}$$

For further details of the IBM employed in this work, the reader is referred to the work of Uhlmann [2005] and for details about how the regularized delta is built, to the work of Peskin [2002] and Roma et al. [1999].

If we introduce the IBM calculations in the scheme described in equation (2.3) we obtain the full algorithm implemented in TUCAN. The substep k of the Runge-Kutta scheme is

$$\vec{u}^e = \vec{u}^{k-1} + \Delta t\left((\alpha_k + \beta_k)\mathbf{L}^{k-1} + \gamma_k\mathbf{N}^{k-1} + \xi_k\mathbf{N}^{k-2} - (\alpha_k + \beta_k)\nabla p^{k-1}\right) \tag{2.9a}$$

$$\vec{U}^e = \sum_{ij}\delta_h\left(\vec{X} - \vec{x}_{ij}\right)\vec{u}^e_{ij}\Delta x^2 \tag{2.9b}$$

$$\vec{F} = \frac{\vec{U}^d - \vec{U}^e}{\Delta t} \tag{2.9c}$$

$$\vec{f} = \sum_{l}\delta_h\left(\vec{X}_l - \vec{x}\right)\vec{F}_l\Delta V_l \tag{2.9d}$$

$$\left(\nabla^2 - \frac{\mathrm{Re}}{\beta_k\Delta t}\right)\vec{u}^* = -\frac{\mathrm{Re}}{\beta_k\Delta t}\left(\vec{u}^e - \beta_k\Delta t\mathbf{L}^{k-1} + \Delta t\,\vec{f}\right) \tag{2.9e}$$

$$\nabla^2\phi = \frac{\nabla\cdot\vec{u}^*}{\Delta t(\alpha_k + \beta_k)} \tag{2.9f}$$

$$p^k = p^{k-1} + \phi - \frac{\beta_k\Delta t}{\mathrm{Re}}\nabla^2\phi \tag{2.9g}$$

$$\vec{u}^k = \vec{u}^* - ((\alpha_k + \beta_k))\Delta t\nabla\phi, \tag{2.9h}$$

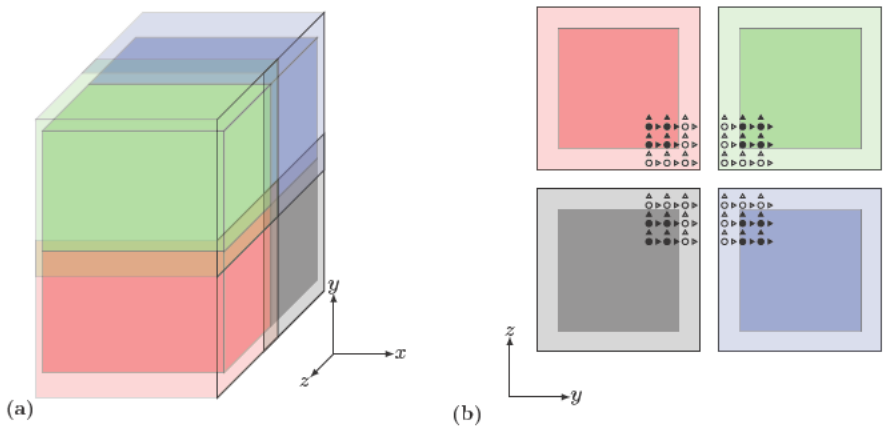

Figure 2.3: a) Domain decomposition of 3D problems in TUCAN. The domain region assigned to each process is highlighted with intense color and the overlapping region that exists because of the presence of ghost points is represented with transparency. b) Outline of the domain assigned to each process removing the overlapping region where the ghost points are located.

where Δx is the mesh width, ΔV the volume associated to each Lagrangian point, $\vec{x}$ and $\vec{X}$ are the position vectors of fluid and solid particles, respectively, and the subscripts ij and l represent the Eulerian and Lagrangian discretized domains, respectively.

2.3 Relevant aspects of the implementation of TUCAN

This section contains the most relevant aspects of the implementation of TUCAN. A detailed description of the code is out of the scope of this document, but the important decisions that have been made which determine in an important manner the performance of the code, are outlined.

2.3.1 Parallelization

The parallelization in TUCAN is based on the Message Parsing Interface (MPI) standard [Forum, 1994]. The main characteristic of the MPI standard is that memory is not shared by the processes participating in the run, even if they belong to the same machine. Therefore, when a process needs data assigned to other process, they must communicate with each other. The MPI standard presents some advantages compared to shared memory protocols like Open MP [Dagum and Menon, 1998], but the setup of communications between processes makes the implementation of MPI a more tedious

task. The main advantage of using MPI is the possibility of increasing the number of processes participating in a run "indefinitely" compared to shared memory applications, where the number of processes participating in a simulation is limited by the number of processors of a workstation. One could buy a machine with a large number of processors, but the cost of increasing this number in a single machine increases exponentially, making the MPI standard the preferred choice to handle large problems.

The work load in TUCAN is distributed following a domain decomposition strategy, assigning different portions of the physical domain (and the corresponding grid) to each process. The partition of the domain is carried out in the x and y (y and z) directions for 2D (3D) problems, without restrictions regarding the number of processes in which each direction is divided. Therefore each process is assigned a structured portion of the domain. Additionally, an extra cell[1] is included in every direction, resulting in an overlapping region between processes. The grid points of this overlapping region are also referred to as ghost points. Figure 2.3a shows the domain decomposition of a 3D problem, where the overlapping region containing ghost points can be appreciated. In figure 2.3b the overlapping is removed to highlight that every process has points where the solution is calculated (full symbols) and ghost points which need to obtain from other processes (empty symbols).

The most demanding communications in TUCAN correspond to the update of ghost points of the buffers where the components of the velocity and the pseudo-pressure are stored. In each sub-step, these communications are performed twice for each of these variables: after the solution of the linear systems (equations (2.9e) and (2.9f)) and after the correction step (equations (2.9h) and (2.9g)). These communications are performed by the non-blocking routines `MPI_ISEND` and `MPI_IRECV` for sending and receiving data, respectively.

2.3.2 Linear systems

The full algorithm implemented in TUCAN (equation (2.9)) to solve Navier-Stokes (equation (2.1)) involves the solution of one linear system for each component of the velocity (equation (2.9e)) and one for the pseudo-pressure (equation (2.9f)). More specifically, each velocity component results in a Helmholtz problem and the pseudo-pressure in a Poisson problem. The Helmholtz problem is easily handled by iterative solvers since it has a dominant diagonal, but the solution of the Poisson problem presents some difficulties. Because the spatial discretization of the problem is done with finite differences, the matrices of these linear systems are sparse. Hypre [2016 June] is an open source library of routines to solve linear systems with sparse matrices, which is conceived to

[1] The term cell refers to a set of one pressure grid point together with one grid point of each component of the velocity

work on massively parallel computers and has shown to be parallel efficient up to thousands of processors [Baker et al., 2012]. Therefore, we use the solvers available in the hypre libraries to find the solution of the linear systems.

We have already mentioned the importance of the performance of TUCAN, so the selection of the specific routines from the library is crucial. Due to the difficulties related to the Poisson problem, the linear system of the pseudo-pressure must be preconditioned with a solver based on multi-grid methods. These methods are typically computationally expensive, but give high converging rates. Helmholtz problems are solved by conjugate gradient solvers and the Poisson problem by a combination of a multigrid method (acting as a preconditioner) with a conjugate gradient method.

2.3.3 Input/Output tasks

The Input/Output tasks (I/O) are the actions performed by the code during execution to read and/or write data from/to a file. These operations are needed to store data for later post-processing and to read existing data to setup a simulation. We find two main issues related to I/O. First, the speed of accessing disk is much lower than the speed of accessing memory, the former being around one hundred times slower. Second, when the number of processes with access to the same file grows, the overhead time related to communications increases exponentially, so I/O become critical. This means that a trade off must be made between the information that the user wants to save and the performance of the simulations. It was decided that the best choice to be used for the I/O in TUCAN is the Hierarquical Data Format version 5 (HDF5) libraries [The HDF Group, 1997-2016]. HDF5 handles the MPI standard and provides routines for collective I/O. As a consequence, large buffers which are distributed among the processes are saved efficiently in an unique output file. Furthermore, the data structure provided by the HDF5 protocol results in a more versatile access to the stored data, independently of how the data was written to the file. Also, the main tools for post-processing scientific data (Matlab, Python or Paraview) include built-in routines for reading and writing files with the HDF5 protocol.

CHAPTER
THREE

Validation of TUCAN

After describing the methodologies used in TUCAN, we proceed to carry out the tests needed to validate the code. Validation is a mandatory step in the development cycle of any code intended to represent real world physics. TUCAN has around 60K lines of code and makes use of external libraries. Furthermore, it requires specific machine configuration, so a thorough evaluation of TUCAN must be carried out prior to its production stage. This chapter is divided into three parts. The first two parts of the chapter contain validation cases of 2D and 3D problems, respectively. The last part of the chapter is dedicated to show the performance of TUCAN.

3.1 Two dimensional cases

3.1.1 Poiseuille

TUCAN is first validated with the 2D Poiseuille flow. This flow is very simple, but the existence of a closed form solution allows us to obtain the error convergence of the spatial discretization. The computational domain size for this case is $2H$ in both the streamwise (x) and vertical (y) directions. The pressure gradient in the streamwise direction $\frac{\partial p}{\partial x}$ is imposed, and its value is set to have $\mathrm{Re} = H\,U_0/\nu = 200$, where U_0 is the maximum velocity of the flow. Periodic boundary conditions are used in the streamwise direction and no-slip boundary conditions in the cross-stream direction. The solution is given by

$$\frac{u_x(y)}{U_0} = 1 - (y/H)^2. \tag{3.1}$$

In this regime the flow is laminar and there are no fluctuations in the solution. Also, both convective and pressure terms in equation (2.1) are zero, so the validation scope of this test is limited to the diffusive terms of equation (2.1).

Figure 3.1a shows the solution of the Poiseuille flow obtained with TUCAN together with the exact solution (equation (3.1)). The results for the vertical component u_y shown in the figure are obtained by modifying the setup of the problem in the following manner: the horizontal and vertical directions are interchanged so that the vertical

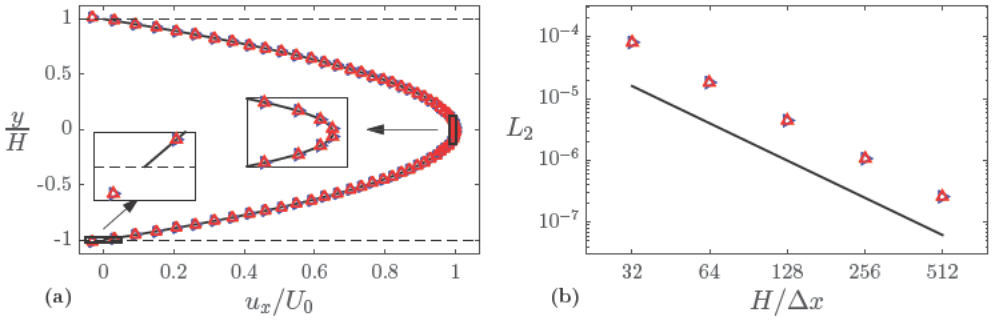

Figure 3.1: a) Analytical and numerical ($H/\Delta x = 32$) solution of the streamwise velocity u_x of Poiseuille flow and b) convergence of the L_2 norm of the error with the spatial resolution. The results shown in the figure correspond to the setup described in the text (▷) and a tilt of 90° of the problem (△) to check the implementation of both components of the velocity. The auxiliary line (——) represents the analytical solution in a) and a straight line with slope -2 in b).

direction y corresponds to the streamwise direction and the pressure gradient $\frac{\partial p}{\partial y}$ is impose accordingly. The figure also shows the boundary ghost points that fall outside the physical domain (see figure 2.1 for reference of the staggered grid). Figure 3.1b shows the error convergence of the numerical solution with the spatial resolution for each of the components of the velocity. The same number of steps are computed for all the cases, but modifying the time step Δt accordingly to keep the Courant Fredrich Levy number (CFL) constant. The figure shows that the order of the finite difference scheme $\mathcal{O}(\Delta x^2)$ is recovered, so we consider this test as successful.

3.1.2 Taylor-Green

Taylor-Green vortex flow in the 2D space is defined by the wavenumber of its vortices in the horizontal and vertical directions, k_x and k_y, respectively. In this test case we set $k_x = k_y$ for simplicity. The computational domain size is $[2\pi/k_x \text{ x } 2\pi/k_y]$ in the horizontal and vertical directions, respectively. Periodic boundary conditions are set in both directions. The maximum velocity at the beginning of the simulation U_0 is selected to have $\mathrm{Re} = U_0/k_x\,\nu = 200$. The solution is given by

$$\frac{u_x}{U_0} = \sin(k_x\,x)\cos(k_y\,y)\mathrm{e}^{-(k_x^2+k_y^2)\nu\,t}, \tag{3.2a}$$

$$\frac{u_y}{U_0} = -\frac{k_x}{k_y}\cos(k_x\,x)\sin(k_y\,y)\mathrm{e}^{-(k_x^2+k_y^2)\nu\,t}, \tag{3.2b}$$

$$\frac{p}{\rho U_0^2} = -\frac{1}{2}\left(\cos^2(k_x\,x)\frac{k_x^2}{k_y^2} - \sin^2(k_y\,y)\right)\mathrm{e}^{-2(k_x^2+k_y^2)\nu\,t}. \tag{3.2c}$$

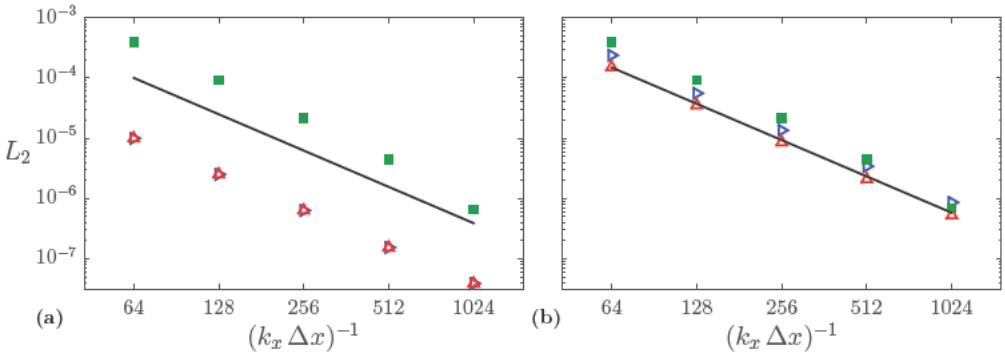

Figure 3.2: Convergence of the L_2 norm of the error with the spatial resolution for Taylor-Green vortex flow at $\mathrm{Re} = U_0/k_x\nu = 200$ a) without embedded boundaries and b) with embedded boundaries. Horizontal (▷) and vertical (△) velocities are represented together with the pressure (■). Auxiliary lines (——) with slope -2 are represented to support the discussion.

This solution is unsteady and non-linear and pressure terms are not zero, so this test complements the previous analysis of Poiseuille flow. Furthermore, two configurations of the problem are studied. The first configuration has no immersed boundaries in order to check the base flow solver, whereas the second, has a circle of diameter $D = 1/k_x$ represented by Lagrangian markers in order to check the implementation of the algorithm. Note that the velocity imposed in the embedded circle is the solution of the flow (equation (3.2)), instead of the typical no-slip condition. Figures 3.1a and b show the error convergence for the case without immersed boundaries and with immersed boundaries, respectively. In both configurations the error diminishes as $\mathcal{O}(\Delta x^2)$, which is the order of the finite differences scheme used. Also, the configuration with immersed boundaries confirms the accuracy of the regularized delta for smooth fields, so both tests are considered as successful.

3.1.3 Stationary cylinder

We continue increasing the complexity of the tests. Now we test the capability of TUCAN to simulate flows around bodies with the classical case of cross flow over a stationary cylinder. The configuration under study is a cylinder of diameter D submerged in a uniform stream of velocity U_∞. The computational domain size is $26.7D$ in both streamwise and cross-stream directions, discretized with 1024 grid points in each of them. This results in a resolution of 38 points per each diameter length in the Eulerian frame. The 3-point κ function (equation (2.7)) is used for the IBM calculations. Free slip boundary conditions are set at the cross-stream boundaries of the domain, an inflow

Table 3.1: Non-dimensional force coefficients for the stationary cylinder at Re = 100. The size of the enlarged domain is $40D \times 40D$.

Case	$\overline{c_d}$	Δc_d	Δc_l	St
Present work	1.501	0.011	0.349	0.172
Uhlmann 2005	1.501	0.011	0.349	0.172
Present work (Enlarged domain)	1.453	0.011	0.339	0.168
Uhlmann 2005 (Enlarged domain)	1.453	0.011	0.339	0.169
Liu et al.	1.350	0.012	0.339	0.165

velocity U_∞ at the inlet and an advective boundary condition at the outlet. The center of the cylinder is located at the origin and the inflow boundary at a distance of $6.17D$ upstream. This leaves $20D$ between the cylinder and the outlet boundary. The time step Δt is selected to have CFL < 0.6 and the Re number of the flow based on the cylinder diameter and the free stream velocity is $\mathrm{Re}_D = D\,U_\infty/\nu = 100$. In this regime the flow is 2D and the wake is the known Von-Karman vortex street.

We compare the results obtained with TUCAN against the results from Uhlmann [2005] and Liu et al. [1998]. The former presents DNS with the same IBM implemented in TUCAN, so it is of high interest for this validation process, and the latter presents DNS with a body-fitted grid. Table 3.1 shows the non-dimensional coefficients of drag and lift obtained with TUCAN and the results from the reference. It can be seen that the oscillating part of the signal is very well captured by the method, but a little overestimation (around 10%) is found in the mean drag coefficient. This overprediction was also seen by Lai and Peskin [2000], who also used an IBM, and attribute this overprediction to the confinement of the flow in the cross-stream direction. In a different work Linnick and Fasel [2005] eliminated this overestimation by increasing the domain size in the cross-stream direction from $18D$ to $43D$. Overall, the results match perfectly with Uhlmann's work (as expected) and there is a good agreement with the work of Liu et al. Therefore, we consider this test case as successful.

3.1.4 Oscillating cylinder

An important feature of TUCAN is the simulation of the flow around arbitrarily moving bodies, so the next step in the validation process of TUCAN is to compute the flow around a transversely oscillating cylinder. The computational setup is the same as in the stationary cylinder case except for the Re, which is set to Re = 185. The motion of the cylinder is defined by

$$y_c(t) = A \sin\left(2\pi\, f\, t\right), \tag{3.3}$$

Table 3.2: Non-dimensional force coefficients for oscillating cylinder at Re = 185. The 3-point κ function is the one from Roma et al. [1999] and the 4 point κ from Peskin [2002].

Case	$\overline{c}_d$	Δc_d	${c_l}^s$
Present work (3 point κ)	1.378	0.063	0.174
Uhlmann 2005 (3 point κ)	1.380	0.063	0.176
Present work (4 point κ)	1.400	0.063	0.171
Uhlmann 2005 (4 point κ)	1.402	0.064	0.172
Lu and Dalton	1.25		0.18

where y_c is the vertical position of the cylinder center, A is the amplitude of the motion, which is set to $0.2D$, and f is the oscillating frequency, which is set to 0.8 times the vortex shedding frequency of the stationary case. The reduced frequency is $k = 2\pi\, f\, D/U_\infty = 0.98$. In this case, where the Lagrangian grid (the cylinder) moves relative to the Eulerian grid (the fluid), the selection of the function κ becomes important. The larger scope of the 4-point κ defined by Peskin [2002] results in a slightly wider blurry region where the forcing term actuates, but smoother results when the lagrangian points move relative to the Eulerian grid.

Table 3.2 shows the non-dimensional force coefficients obtained with TUCAN together with the results from Uhlmann [2005] and Lu and Dalton [1996]. The latter presents DNS of a body-fitted grid in circumferential coordinates. Our results and the work of Uhlmann have differences smaller than 0.15% in the mean value of drag coefficient and smaller than 1.5% in the oscillating part of the drag and lift signals. Good agreement is obtained with the results of Lu and Dalton [1996], although the drag coefficient is a little overestimated, and the root mean squared (rms) value of the lift a little underestimated. Also, if we compare the results obtained with the different κ functions, it can be seen how the mean drag coefficient obtained with the 4-point κ is a little higher than the obtained with the 3-point κ, while the lift is underestimated. The differences between the two κ functions is shown in figure 3.3, where the drag coefficient c_d versus the vertical position of the cylinder y_c is represented for the case with the 3-point κ (figure 3.3a) and the 4-point κ (figure 3.3b). The agreement between the work of Uhlmann [2005] and the results of TUCAN is very good. It can be seen the overestimation of the drag by the 4-point κ and the smoother evolution of the force compared to the 3-point κ. We also consider this test case as successful.

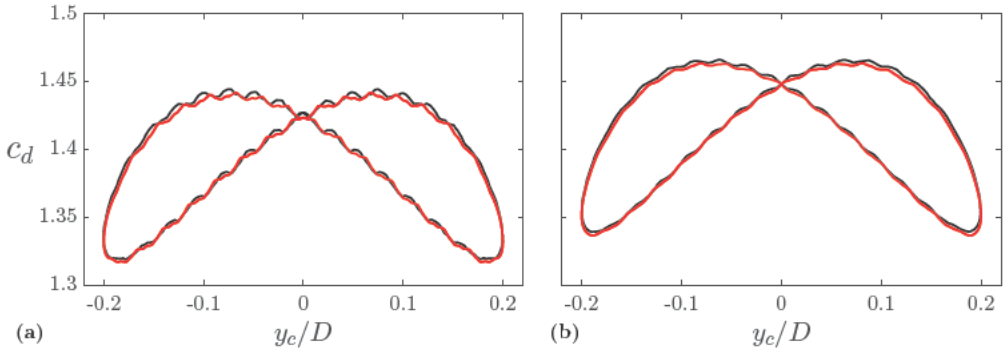

Figure 3.3: Drag versus vertical position for cross flow over oscillating cylinder using the function κ defined a) by Peskin Peskin [2002] with a scope of 3 points and b) by Roma et al. Roma et al. [1999] with a scope of 4 points. Curves represented correspond to the results obtained with TUCAN (——) and the work of Uhlmann [2005] (——).

3.2 Three dimensional cases

3.2.1 Laminar channel

In this section we present the validation case for a laminar channel flow. The computational domain size is $[2H \times 2H \times H]$ in the streamwise, vertical and spanwise direction, respectively. Periodic boundary conditions are set in the streamwise and spanwise directions and no-slip boundary conditions in the vertical direction. The pressure gradient in the streamwise direction $\frac{\partial p}{\partial x}$ is imposed, and its value is selected to obtain a maximum velocity U_0 such that $\mathrm{Re} = HU_0/\nu = 100$. The spatial resolution $H/\Delta x$ is set 8, 16 and 32 in order to check the order of error convergence. The time step is selected to keep $\mathrm{CFL} < 0.5$ and we use the same spatial resolution in every direction ($\Delta x = \Delta y = \Delta z$). Furthermore, two cases in which the pressure gradient is oriented in the vertical and spanwise directions, respectively, are analyzed. These two cases have the coarsest resolution ($H/\Delta x = 8$) and their boundary conditions are modified accordingly. Figure 3.4a shows the numerical solution obtained with TUCAN together with the exact solution (equation (3.1)). It can be seen that for the three components of the velocity the parabola is captured with an error not perceptible by visual inspection. Figure 3.4b shows the evolution of the L_2 norm of the error of the numerical solution with the spatial resolution. The second order convergence with spatial resolution of the scheme is confirmed, so we consider the test as successful.

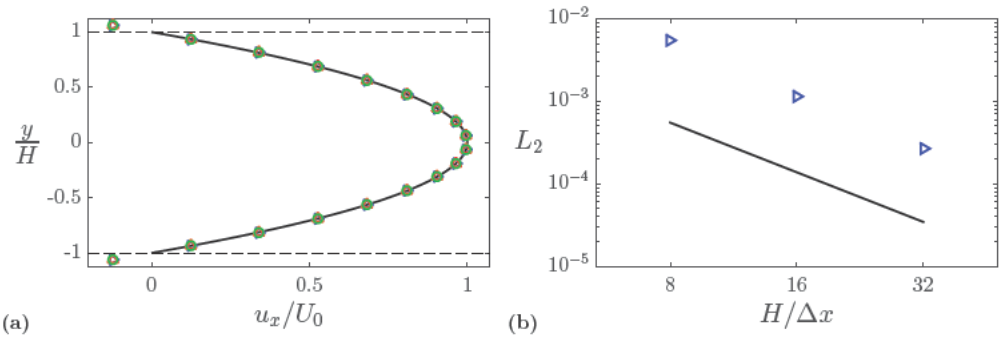

Figure 3.4: a) Analytical and numerical ($H/\Delta x = 8$) solution of the streamwise velocity of a laminar channel at Re = 100 and b) evolution of the L_2 norm of the error with spatial resolution. The results shown in the figure correspond to the setup described in the text (▷) and a tilt of the problem to check the implementation of the implementation of the y (△) and z (○) components of the velocity. The auxiliary line (——) represents the analytical solution in a) and a straight line with slope -2 in b)

3.2.2 Turbulent channel

As it was mentioned before, the power of the laminar channel as a validation test case is the existence of a closed form solution, but it is a steady case in which neither the non-linear nor the pressure terms are evaluated. Taylor Green vortex flow cannot be used because it is unstable in its 3D configuration, so we have decided to continue the validation process of TUCAN with a turbulent channel. This problem has been widely studied in the literature and data is available from reliable sources, which makes this case even more suitable for testing purposes. The configuration under study is taken from Kim et al. [1987]. The computational domain has a semi-height of H and the streamwise and spanwise dimensions are set to $4\pi H$ and $4\pi H/3$, respectively. The domain size in the spanwise domain is 2/3 smaller than the reference of Kim et al. [1987]. The pressure gradient in the streamwise direction is selected to have a Re based on the friction velocity u_τ of $\mathrm{Re}_\tau = u_\tau H/\nu = 180$, which results in a Re number based on the mean center velocity U_c of $\mathrm{Re}_c = U_c H/\nu \approx 3300$. We use 128, 96 and 128 grid points in the streamwise, vertical and spanwise directions, respectively, giving a resolution of $H/\Delta x = 10.2$, $H/\Delta y = 48$ and $H/\Delta z = 30.6$. The mesh width in wall units is $\Delta x^+ = 17.7$, $\Delta y^+ = 3.75$ and $\Delta z^+ = 5.5$. Note that $\Delta y^+ = 3.75$ is not enough resolution near the wall, but in this configuration, the first point of streamwise and spanwise components of the velocity is located at 1.875 wall units from the boundary because of the layout of the grid, which is sufficient for the purposes of this test. Regarding the time step, it has been selected to keep CFL < 0.2.

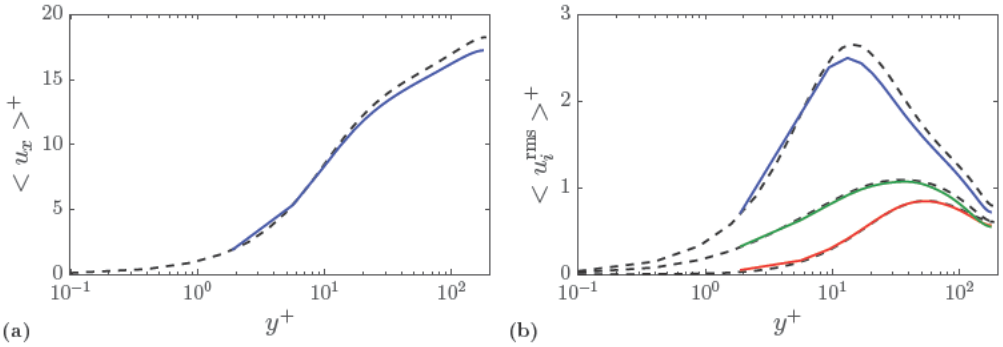

Figure 3.5: a) Mean and b) rms velocity profiles. The results obtained from TUCAN for the streamwise u_x (——), vertical u_y (——) and spanwise u_z (——) velocities are shown together with the reference from del Álamo and Jiménez [2003] (- - -) [1].

Figure 3.5 shows the averaged mean and rms values of the velocities for the turbulent channel once the case is statistically converged. The operator $< \cdot >$ in figure 3.5 indicates averaging in time and in the homogeneous space coordinates (x and z). It can be seen that rms values for the vertical and spanwise components of the velocity (figure 3.5b) are very well captured by TUCAN and mean (figure 3.5a) and rms (figure 3.5b) values of the streamwise component of the velocity are only a little underestimated. We attribute this small discrepancy to the fact that our simulation is slightly under-resolved and the compuational domain is smaller than the one used in the reference. In the work of del Álamo and Jiménez [2003] the computaional domain is $[8\pi H \,\mathrm{x}\, 4\pi H]$ in the streamwise and spanwise directions, respectively, and our computaional domain is $[4\pi H \,\mathrm{x}\, 4\pi/3H]$. Furthermore, we use a spatial discretization based on finite differences whereas the reference uses spectral methods. Therefore, we consider the validation succesful.

3.2.3 Sphere in channel

The last case in the validation process of TUCAN consists of a channel flow with a sphere located at the center of the domain [Uhlmann, 2006]. The computational domain is $[2H \,\mathrm{x}\, 2H \,\mathrm{x}\, 2H]$ in the streamwise, vertical and spanwise directions, where H is the semi-height of the channel. The sphere has a diameter $D/H = 0.4844$ and it is located in the center of the domain. Periodic boundary conditions are imposed in the streamwise and spanwise directions and no-slip boundary conditions in the vertical direction. We use 128 grid points in every direction, resulting in a resolution of $H/\Delta x = 96$. The time step Δt is selected to have CFL < 0.5.

Figure 3.6 shows velocity profiles along straight paths that pass through the center

[1] The reference data is published online [Fluid Dynamics Group, 2016]

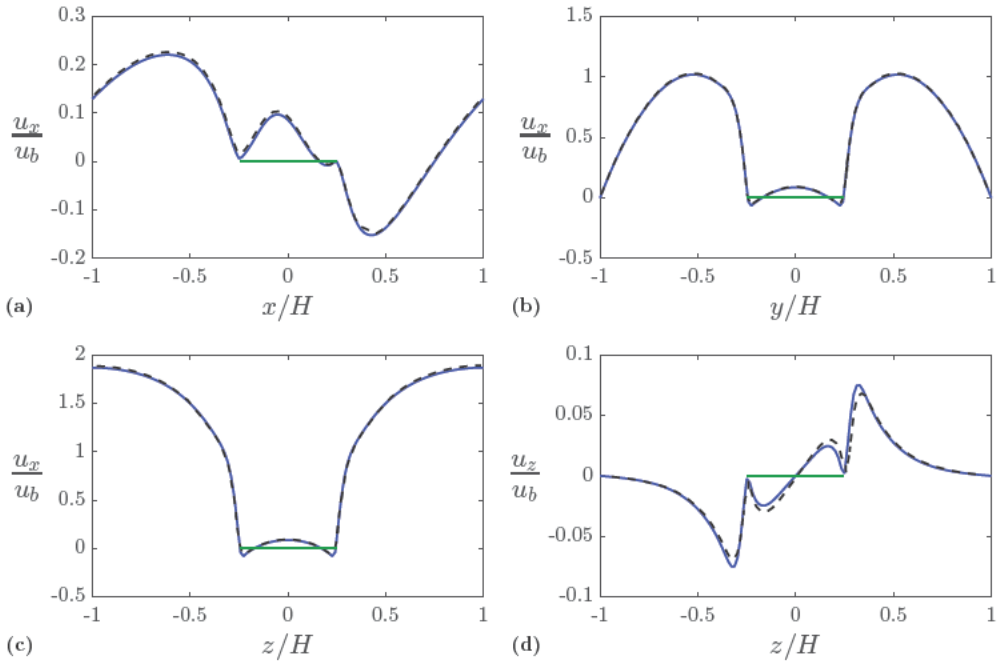

Figure 3.6: Profiles of streamwise velocity along the a) streamwise, b) vertical and c) spanwise direction and of d) spanwise velocity along the spanwise direction. All profiles pass through the center of the sphere (——). The results obtained with TUCAN (——) are represented together with the results from Uhlmann [2006] (- - -).

Table 3.3: Mean drag coefficient for the validation case of a sphere inside a channel

Case	$\mathrm{Re_b}$	$\overline{c_d}$
Uhlmann [2006]	269.9	0.7211
TUCAN	275.4	0.7109

of the sphere. In the figure, results obtained with TUCAN are plotted together with the results from Uhlmann [2006]. Figures 3.6a, b and c show profiles of streamwise velocity along the streamwise, vertical and spanwise coordinate, respectively. Figure 3.6d shows a profile of spanwise velocity along the spanwise direction. The agreement between the present results and the reference is very good. Note that in figures 3.6a and d, where the differences observed are slightly more pronounced, the velocity is smaller, so errors become more noticeable. Regarding the integrated values of the force, table 3.3 shows the mean drag coefficient obtained with TUCAN and the results from Uhlmann [2006]. The difference between the two values is smaller than 1.5%. We believe that this small difference is attributed to the small difference in the $\mathrm{Re_b}$ of the two cases.

To conclude with the test cases, we use this configuration to evaluate the influence of the distribution of Lagrangian points on the surface of the body. When simple geometries are used in the simulations, it is possible to distribute equi-distant points on their surfaces but, this is only true for a limited number of cases. A sphere is one example where distribute equidistant points in its surface is an open problem. In these situations the approach is to distribute the points as uniformly as possible. To analyze the influence of the small non-uniformity present in these situations, we repeat the case of the channel flow with a small modification. We carry out two simulations in which the pressure gradient is set in y and z directions, respectively. The boundary conditions are modified accordingly, but the discretized geometry of the sphere is fixed. In both cases the relative error in the non-dimensional drag coefficient compared to the x oriented case was smaller than 0.003%. With this test, apart from the validation of the implementation of TUCAN it is shown that the slight non-uniformity in the distribution of points within the geometry does not affect the integral of forces.

3.3 Performance

In this section we analyze the parallel performance of TUCAN in terms of time. For a simulation that takes t_N time to complete with N processes the speedup and parallel

Table 3.4: Unitary time of 2D cases of cross flow over a cylinder and 3D cases of laminar channel with a sphere in the middle and turbulent channel. The total time (t_u) is shown together with the time spent in solving the linear systems for the velocity (${t_u}^A$), the pseudo pressure (${t_u}^B$) and the calculations of the immersed boundaries (${t_u}^C$).

Case	Dim.	N	$t_u[\mu s]$	${t_u}^A[\mu s]$	${t_u}^B[\mu s]$	${t_u}^C[\mu s]$
Moving cylinder ($\kappa 3$)	2D	12	11.0	1.1(10.4%)	8.0(72.7%)	0.0(0.0%)
Moving cylinder ($\kappa 4$)	2D	12	11.1	1.1(10.1%)	8.2(73.1%)	0.0(0.0%)
Stationary cylinder	2D	12	11.6	1.2(10.7%)	8.4(73.0%)	0.0(0.0%)
Stationary cylinder 2	2D	12	12.7	1.6(12.3%)	9.1(71.6%)	0.0(0.0%)
Sphere in channel 1	3D	48	27.1	3.8(14.2%)	17.7(65.3%)	1.8(6.5%)
Sphere in channel 2	3D	12	20.6	2.5(12.4%)	12.6(61.4%)	1.0(4.9%)
Sphere in channel 3	3D	24	20.8	2.3(10.9%)	13.2(63.4%)	0.9(4.3%)
Turbulent channel	3D	48	45.3	2.5(5.6%)	24.5(54.1%)	0.0(0.0%)

efficiency are defined as

$$S = \frac{t_0\, N_0}{t_N}, \tag{3.4a}$$

$$E = \frac{t_0\, N_0}{t_N\, N}, \tag{3.4b}$$

where t_0 is the time that it takes to complete the simulation with N_0 processes [2] and t_N the time with N processes. We also define the unitary time

$$t_u = \frac{t\, N}{N_G N_S}, \tag{3.5}$$

where N is the number of processors, N_G the number of grid points and N_S the number of steps. For an ideal parallel efficiency ($E = 1$), the unitary time is independent of the grid size N_G and number of processors N. In reality, the time performance depends on the aforementioned quantities because the parallel efficiency is influenced by both the grid size and the partition of the domain.

Some of the validation cases presented in previous sections of this chapter are used here to evaluate the performance of TUCAN. Table 3.4 shows the time performance of these cases. The solution of the Poisson problem of the pseudo pressure is the most demanding part of the algorithm, requiring more than 70% of the total time for its computation in the 2D version of the code and approximately 60% in the 3D version. Conversely, the Helmhotz problem of the velocities is computed much faster, using only 10% of the total time in the solution of the two components of the velocity field in the

[2] $t_0\, N_0$ is the estimated time to complete the simulation with one process under the assumption of ideal parallel efficiency from one process to N_0 processes

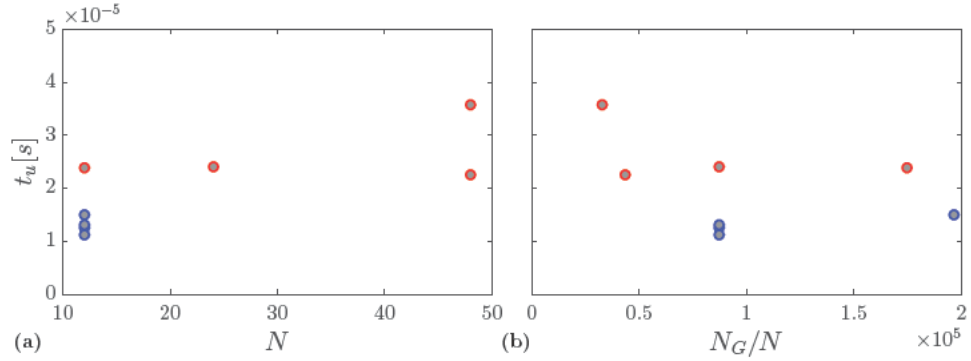

Figure 3.7: Unitary time for 2D (●) and 3D (●) cases versus a) the number of processors and b) the number of grid points per processor.

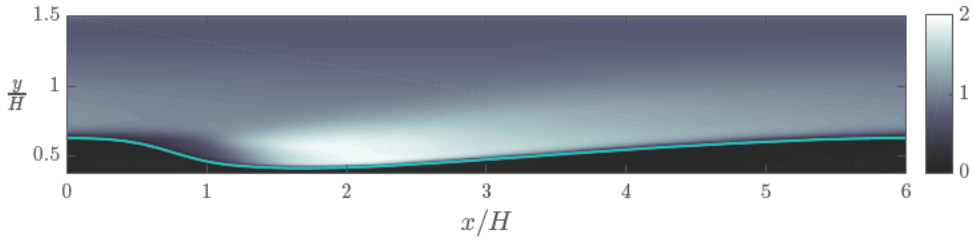

Figure 3.8: Root mean squared values of the spanwise velocity fluctuations ${u_z}'^{\text{rms}}$ for the original dune used for the scalability test.

2D version of the code and little more than 10% in the solution of the three components of the velocity in the 3D version. The time spent in the immersed boundary calculations is negligible in the 2D version of the code. Figure 3.7 shows the unitary time of 2D and 3D cases.

In addition to the validation cases presented above we have performed a scalability test in a super computer center. We have selected a large problem to carry out different runs varying the number of processes participating from 1024 to 8192. The problem is based on an already converged case: the flow over a dune. The original domain size was $[6H \text{ x } 1.125H \text{ x } 6H]$ in the streamwise, vertical and spanwise direction, respectively, where H is the height of the domain measured from the lowest point of the dune. This domain was discretized with $[1024 \text{ x } 192 \text{ x } 1024]$ grid points in the steramwise, vertical and spanwise directions, respectively. Figure 3.8 shows the spanwise velocity fluctuations averaged in time and in the spatially homogeneous coordinates. The actual problem used for the scaling test is built by repeating one time the dune in the streamwise (x) and

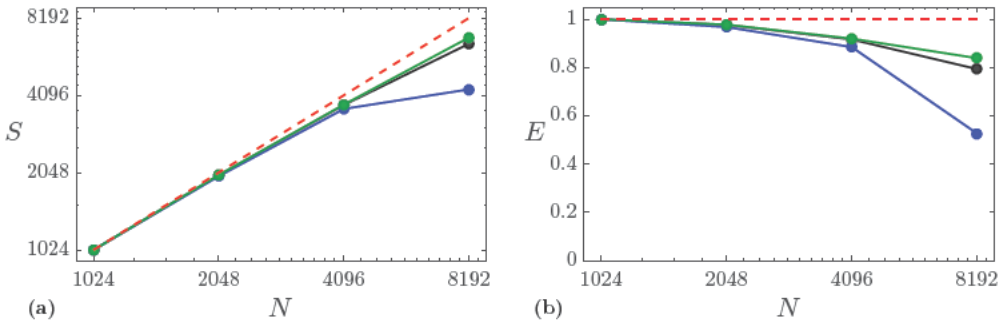

Figure 3.9: a) Speed up and b) parallel efficiency of TUCAN obtained in the case of dune. The data represented correspond to the time spent in all the solvers (●—●), in the Helmholtz problem for the velocities (●—●) and in the Poisson problem for the pseudo-pressure (●—●). The ideal performance of a parallel code is also represented (- - -).

Table 3.5: Parallel performance of TUCAN in the scaling test of the dune.

N	Unitary time (s)	Percentage in $\vec{u}$	Percentage in ϕ
1024	$2.002 \cdot 10^{-5}$	9.61%	90.39%
2048	$2.048 \cdot 10^{-5}$	9.70%	90.30%
4096	$2.177 \cdot 10^{-5}$	9.96%	90.04%
8192	$2.387 \cdot 10^{-5}$	14.48%	85.52%

spanwise (z) directions, resulting in a domain of $[12H \times 1.25H \times 12H]$ discreteized with $[2048 \times 192 \times 2048]$ grid points. This way the problem is large enough to be handled properly by large number of processes.

Figures 3.9a and b show the speed-up and parallel efficiency, respectively, with respect to the number of processors for the enlarged dune problem. It can be seen that the combination of multigrid with al light solver used to solve the pseudo-pressure has a good performance, obtaining a parallel efficiency of 0.84 from 1024 processes to 8192 processes. Apparently, the light solvers used for the velocities do not perform so well but, the time spent in this part of the code is so small, that the overhead that implies the communication starts to dominate. If we combine both times in the same calculation, it can be seen that the parallel performance is barely affected by the loss of parallel efficiency of the solvers used for the velocity.

CHAPTER
FOUR

Aerodynamic forces on airfoils [1]

In this chapter we analyze the aerodynamic forces produced by flapping airfoils at low Re. It was decided that the best approach to adopt for this specific problem was to perform DNS. This approach is particularly useful when no theories are available to describe the flow field. The low Re in which small birds and insects fly and the large amplitude of their motions result in a flow regime which is far from Stokes theory and also from potential theory [Wang, 2005]. In the chapter, first, the physics that govern the problem are outlined and the numerical model used to represent the phenomena at play, is defined. Then, we describe the database of cases generated by varying some of the parameters participating in the problem. The results of these cases are analyzed and a reference case is selected to perform a detailed analysis. Finally, a subset of cases from the database is studied in order to understand the influence that the different parameters have on the aerodynamic performance of the airfoils.

4.1 Problem definition

We present DNS of the flow around a symmetric airfoil NACA 0012. The Re number of the flow based on the airfoil chord c and the free stream velocity U_∞ is $\mathrm{Re} = cU_\infty/\nu = 1000$, where ν is the kinematic viscosity of the fluid. The simulations have been performed using TUCAN, which has been described in chapter 2.

The prescribed heaving and pitching motion of the airfoil is given by

$$h(t) = h_0 \cos(2\pi f t), \tag{4.1a}$$

$$\theta(t) = \theta_m + \theta_0 \cos(2\pi f t + \varphi), \tag{4.1b}$$

where h_0 and θ_0 are the heaving and pitching amplitude, respectively, θ_m is the mean pitch value, φ is the phase shift between the heaving and pitching motion and f is

[1] Partial content of this chapter can be found in the following articles
Moriche, M., Flores, O., and García-Villalba, M. Generation of thrust and lift with airfoils in plunging and pitching motion. In *J. Phys.: Conf. Ser.*, volume 574, page 012163, 2015
Moriche, M., Flores, O., and García-Villalba, M. On the aerodynamic forces on heaving and pitching airfoils at low Reynolds number. In *J. Fluid Mech.*, 2017, Submitted

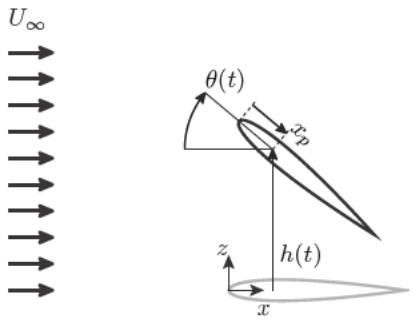

Figure 4.1: Sketch of the heaving and pitching motion of the airfoil.

the frequency of motion. The pitching motion is a rotation around a point located at a distance x_p from the Leading Edge (LE), as it can be observed in the sketch shown in figure 4.1. The set of non-dimensional parameters which define the problem $(h_0/c, \theta_m, \theta_0, \varphi, k, x_p/c, \mathrm{Re})$ results in a large parametric space, so we only vary two of them. The Reynolds number is $\mathrm{Re} = 1000$ and the pivoting point is located at the quarter of the chord ($x_p = c/4$). The heaving amplitude is $h_0 = c$, the pitching amplitude is $\theta_0 = 30°$ and the reduced frequency is $k = 2\pi f c/U_\infty = 1.41$, resulting in a period of oscillation $T = 4.44\, c/U_\infty$. The effect of the mean pitch angle and the phase shift between heaving and pitching are explored, varying θ_m in the range 0° to 20° in steps $\Delta\theta_m = 10°$ and φ from 30° to 130° in steps $\Delta\varphi = 20°$. This results in a database of 18 simulations as summarized in table 4.1. Note that each case is identified by a letter, A, B or C, corresponding to the value of θ_m, followed by three digits that correspond to the value of φ.

4.2 Computational setup

All simulations are performed in a computational domain of dimensions $25c \times 15c$ in the streamwise and vertical directions, respectively. The resolution used in this study is 128 points per chord, yielding a total of 3200 x 1920 grid points in the streamwise and vertical directions, respectively. This resolution has been selected based on a grid refinement study for a NACA 0012 at $\mathrm{Re} = 1000$ set in pure heaving motion. The free stream condition is modelled by an inflow velocity U_∞ at the inlet boundary, located $5c$ upstream of the airfoil. The outflow is modelled with an advective boundary condition at the outlet, located $19c$ downstream of the airfoil. A free slip boundary condition is imposed at the lateral boundaries (see figure 4.2).

The NACA0012[2] airfoil is discretized by a uniform distribution of points along its

[2]A slight modification of the geometry of the airfoil is introduced to remove the finite thickness that

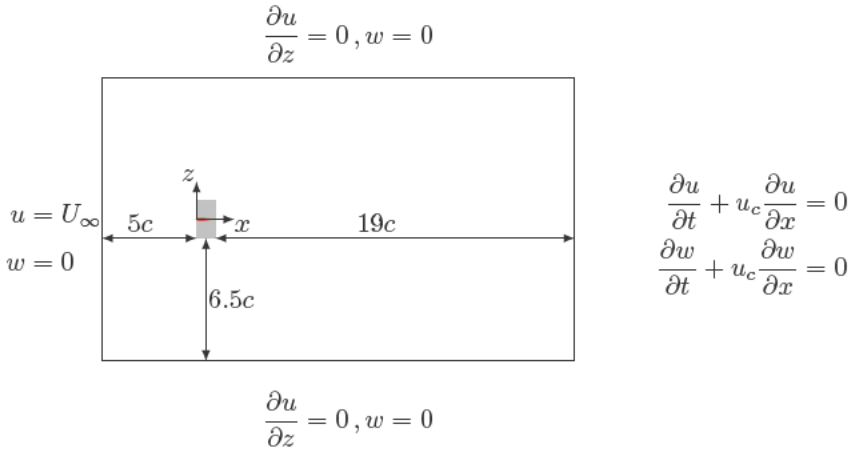

Figure 4.2: Computational setup of the problem.

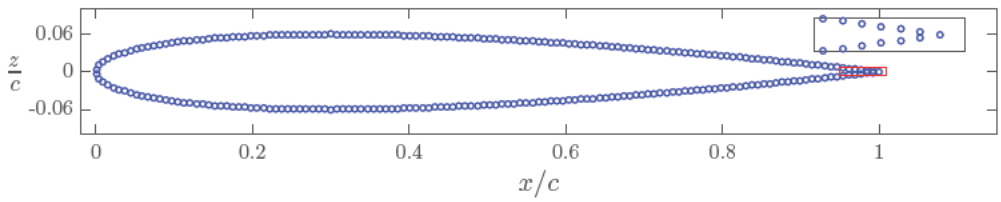

Figure 4.3: Lagrangian markers distribution along the NACA 0012 surface for a resolution of 128 points per chord. The associated volume for each marker is $\Delta V/c^2 = 6.105 \cdot 10^{-5}$.

surface (Figure 4.3). The procedure to distribute points along a circumference is detailed in the appendix A.1 of the work of Uhlmann [2005]. We keep here the requirement of having the volume associated to each Lagrangian point ΔV as close as possible to Δx^2, but we adapt the procedure to the airfoil geometry. We use a total of 261 point along the airfoil surface resulting in an associated volume of $\Delta V/c^2 = 6.105 \cdot 10^{-5}$, which is only 0.023% larger than Δx^2. With this configuration the maximum thickness of the airfoil ($e_{\mathrm{MAX}} = 0.12c$) is represented in the Eulerian frame by 15 grid points and the chord by 128 points. The function κ selected for the interaction between the Eulerian and the Lagrangian frames is the 3-point κ from Roma et al. [1999] (equation (2.7)).

Throughout the rest of the document we evaluate the performance of the airfoil in terms of the non-dimensional coefficients of thrust (c_t) and lift (c_l), expressed as

$$c_t = \frac{-2\,F_x}{\rho {U_\infty}^2 c}, \quad c_l = \frac{2\,F_z}{\rho {U_\infty}^2 c}, \tag{4.2}$$

where F_x and F_z are the total streamwise and vertical forces, respectively, that the fluid exerts on the airfoil. These forces are easily obtained from the direct forcing IBM used in this work (see appendix A.2.2 in Uhlmann [2003]). Also, to support the following discussion we define the average operator $\overline{(\cdot)}$ on a dummy function g as

$$\overline{g} = \frac{1}{T_{av}} \int_{T_{av}} g(t) \mathrm{d}t, \tag{4.3}$$

where T_{av} is the time span for the averaging process. Finally, the rms is defined as

$$g^{\mathrm{rms}} = \sqrt{\frac{1}{T_{av}} \int_{T_{av}} (g(t)^2 - \overline{g}^2)\, \mathrm{d}t}. \tag{4.4}$$

4.3 Results

Eighteen cases have been analyzed by means of 2D DNS. First, we evaluate the performance of the whole database in terms of the non-dimensional coefficients of thrust (c_t) and lift (c_l). Most of the cases present periodicity with a period equal to the motion period $TU_\infty/c = 4.44$, but there are two cases with a doubling period phenomena, and four aperiodic, so the time span for the averaging T_{av} each case has been selected accordingly (see table 4.1 and appendix A.1). This aperiodic or quasi-periodic behavior has been also observed by other authors for a pure heaving configuration, for example [Lewin and Haj-Hariri, 2003]. Table 4.1 shows the averaged and rms values of non-dimensional thrust and lift coefficients together with the propulsive efficiency, η, which is defined as

$$\eta = \frac{T_{av}\, \overline{F}_x\, U_\infty}{\int_0^{T_{av}} \left(F_z\, \dot{h} + M_{y,c/4}\, \dot{\theta}\right) \mathrm{d}t}, \tag{4.5}$$

NACA airfoils have at the Trailing Edge (TE) for manufacturing purposes. In the expression for the half thickness of the airfoil we have set the coefficient of the term $(x/c)^4$ to -0.1036 instead of -0.1015.

Table 4.1: Motion parameters and integrated values of non-dimensional force coefficients of thrust and lift of all the cases. The periodicity of the flow is indicated with P for periodic, D for periodic with period $2T$ and A for aperiodic.

Case	θ_m	φ	$T_a v$	Per.	$\overline{c_t}$	${c_t}^{\mathrm{rms}}$	$\overline{c_l}$	${c_l}^{\mathrm{rms}}$	η
A030	0	30	10	A	−0.4382	0.6144	0.0041	3.3181	-
A050	0	50	1	P	0.1566	0.7184	0.0000	2.6276	0.0834
A070	0	70	1	P	0.8062	0.7550	0.0000	2.4396	0.3374
A090	0	90	1	P	0.9957	0.9751	0.0000	2.7164	0.3644
A110	0	110	1	P	1.0439	1.2878	0.0000	3.7486	0.2933
A130	0	130	1	P	0.9582	1.4988	0.0046	5.2013	0.1937
B030	10	30	5	A	−0.3202	0.7715	0.2662	3.0791	-
B050	10	50	1	P	0.0972	0.7235	0.4163	2.6734	0.0519
B070	10	70	1	P	0.5718	0.7054	0.8452	2.7008	0.2467
B090	10	90	1	P	0.7245	0.9224	1.5507	2.7743	0.2620
B110	10	110	1	P	0.8635	1.2008	1.6032	3.7622	0.2348
B130	10	130	1	P	0.7547	1.4351	1.6678	5.0979	0.1539
C030	20	30	10	A	−0.9957	1.1545	1.2519	3.1465	-
C050	20	50	1	P	−0.8843	0.7999	2.2511	2.3009	-
C070	20	70	15	A	−0.0468	0.5790	1.7455	2.7850	-
C090	20	90	2	D	−0.1419	0.9511	2.7850	2.9327	-
C110	20	110	1	P	0.1425	1.0816	3.0268	3.7850	0.0392
C130	20	130	2	D	0.1167	1.2621	3.1868	4.8437	0.0250

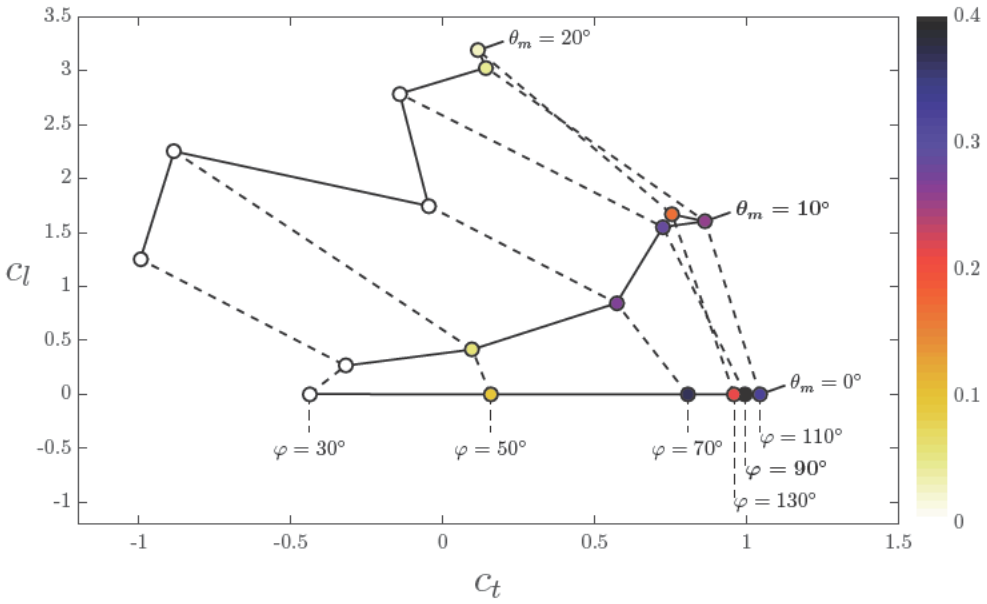

Figure 4.4: Averaged c_l versus averaged c_t. The color corresponds to the propulsive efficiency

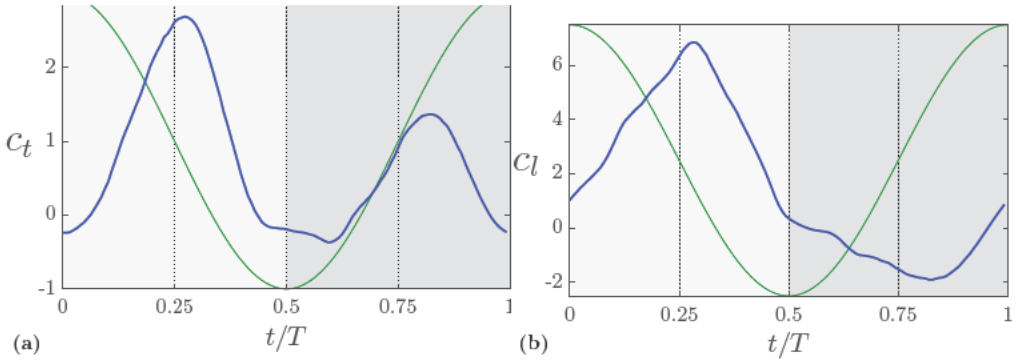

Figure 4.5: Non-dimensional coefficiencts of a) thrust and b) lift for the optimum case B090. The downstroke ($0 < t/T < 0.5$) is represented in lighter gray and upstroke ($0.5 < t/T < 1$) in darker grey. The evolution of the force is represented (——) together with the vertical position of the pivoting point h (——). The downstroke (upstroke) is indicated by a light (dark) grey background.

where $M_{y,c/4}$ is the spanwise moment about the quarter of the chord. In figure 4.4 each case is represented by a point whose coordinates are given by its time averaged values of non-dimensional thrust and lift coefficients and coloured by its propulsive efficiency. Solid (dashed) lines connect cases with constant mean pitch value θ_m (phase shift φ). It can be seen that when the phase shift is fixed, an increase of the mean pitch value results in an increase of lift and a reduction of thrust (dashed lines in figure 4.4). Conversely, when the mean pitch value is fixed, there is an optimum value of phase shift to generate thrust (solid lines in figure 4.4). More specifically, for a mean pitch value θ_m equal to 0° and 10°, the maximum thrust is obtained for a phase shift φ of 110°. The highest propulsive efficiency is 36%, obtained for $\theta_m = 0°$ and a phase shift $\varphi = 90°$. Also, cases with $\theta_m = 10°$ and $\varphi = 90 - 110°$ obtain relatively high c_t and c_l, with propulsive efficiencies higher than 20%. Finally, note that for $\theta_m = 20°$ the propulsive efficiencies are low, although lift coefficients are higher, with a tendency to lose periodicity (see appendix A.1). For the rest of the manuscript we use case B090 as a reference case to perform a more detailed analysis. We select this case because it generates thrust and lift with an associated propulsive efficiency of 26%, so it is interesting in terms of aerodyanmic performance. Also, by varying the phase shift or the mean pitch value, a subset of the database can be studied in order to understand the effects of the motion parameters on the aerodynamic forces.

4.3.1 Analysis of a reference case

Case B090 generates net thrust ($\overline{c}_t = 0.72$) and lift ($\overline{c}_l = 1.55$). The rms value of the force is slightly higher than the mean in the case of thrust (${c_t}^{\text{rms}} = 0.92$) and almost double in the case of lift (${c_l}^{\text{rms}} = 2.77$). This reflects that in this type of flows, the oscillatory component of the force is as important as its mean value. Figures 4.5a and b show the evolution of the aerodynamic thrust and lift, respectively, of case B090 during one period. Two peaks of thrust (figure 4.5a) are generated during the period, one in the downstroke and one in the upstroke, presenting a higher peak of thrust in the former. Regarding the lift (figure 4.5b), the large amount of lift generated in the downstroke is reduced partially by the negative lift produced in the upstroke.

We continue the analysis of case B090 by performing flow visualization of the vorticity field. Figure 4.6 shows contours of spanwise vorticity ω_y of case B090 at eight equispaced time instants during one period. The most noticeable structure is the big LEV, which is created and shed into the wake every motion period. The LEV is created before the middle of the downstroke (figure 4.6b) and remains attached to the upper surface of the airfoil until the end of the stroke (figures 4.6c and 4.6d). At the end of the downstroke the LEV starts to detach from the airfoil (figure 4.6e) and it is shed into the wake approximately after the transition from downstroke to upstroke (figure 4.6f). After being shed (figure 4.6g), the LEV is advected into the wake suffering a diffusion process that is not detectable by visual inspection. Although there are no more vortex generated during the downstroke, the shear layer created at the lower surface of the airfoil ($\omega_y < 0$) is shed into the wake forming small vortices (figures 4.6d, e and f), some of which interact with the LEV (figures 4.6 g and h). During the upstroke the airfoil moves with a low effective angle of attack and, as a result, no vortices are generated. Instead, similarly as in the downstroke, the shear layer created in the lower part of the airfoil is shed into the wake forming small vortices (figure 4.6a, b and c).

4.3.2 Extension of the analysis to the database

We proceed now to analyze the subset of cases A090, B090, C090, B070 and B110. The mean pitch influence is analyzed with cases A090, B090 and C090, which have a constant phase shift φ of 90° and a mean pitch value θ_m of 0°, 10° and 20°, respectively. The phase shift influence is analyzed with cases B070, B090 and B110, which have a constant mean pitch value θ_m of 10° and a phase shift φ of 70°, 90° and 110°, respectively. Figure 4.7 shows the cases selected in the thrust-lift representation.

Starting with integrated values, we analyze the values of $\overline{c}_t$ and $\overline{c}_l$ summarized in table 4.1. If the mean pitch value θ_m is set to zero (case A090), the performance of the airfoil is improved with respect to case B090 ($\theta_m = 10°$) in terms of thrust, but at the cost of producing zero lift. The $\overline{c}_t$ generated by case A090 is increased by 37.5% with

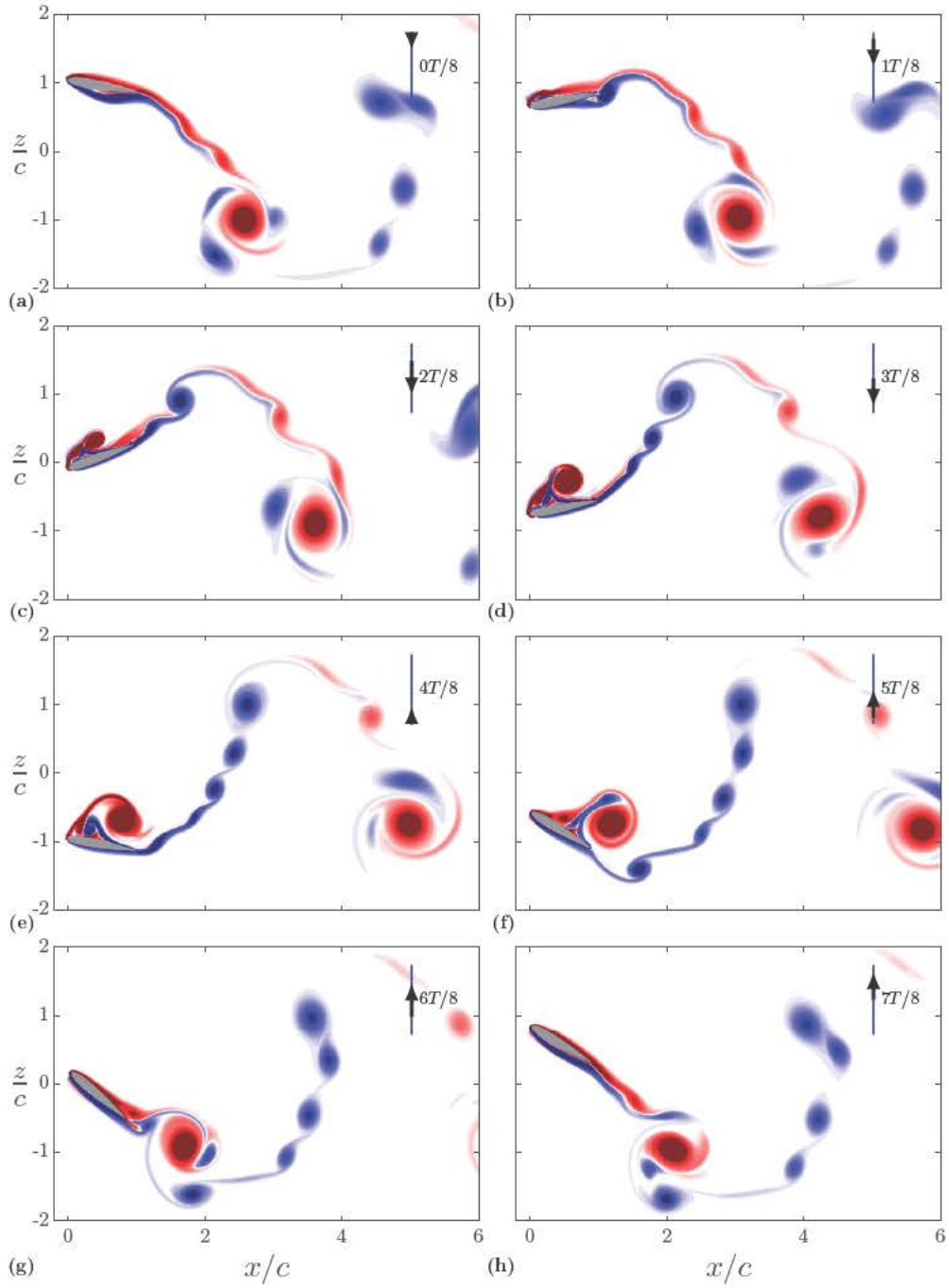

Figure 4.6: Spanwise vorticity ω_y of case B090 at a) beginning of downstroke $t/T = 0$, b) $t/T = 0.125$, c) middle of downstroke $t/T = 0.25$, d) $t/T = 0.375$, e) transition from downstroke to upstroke $t/T = 0.5$, f) $t/T = 0.625$, g) middle of upstroke $t/T = 0.75$ and h) $t/T = 0.875$. Blue corresponds to $\omega_y c/U_\infty = -15$ and red corresponds to $\omega_y c/U_\infty = 15$.

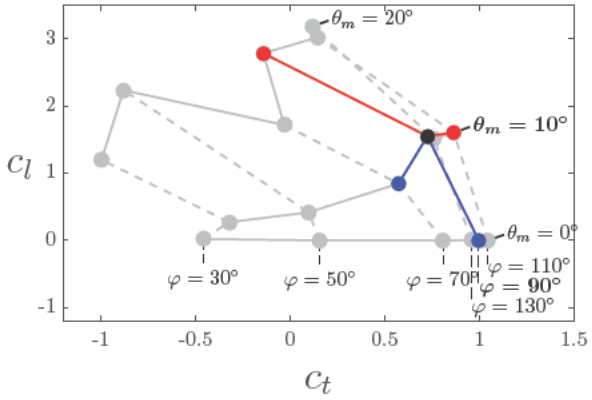

Figure 4.7: Cases selection to study the influence of the motion parameters on the aerodynamic performance.

respect to B090 and the propulsive efficiency by 40%. Conversely, if the mean pitch value θ_m is increased to 20° (case C090), a large lift is generated ($\overline{c}_l = 2.8$), at the cost of producing a small net drag ($\overline{c}_t = -0.15$). The phase shift has a less intuitive effect. A lag in the pitching motion ($\varphi < 90°$, as in case B070) results in lower performance, specially for the lift, whereas an advance of the pitching motion ($\varphi > 90°$, as in case B110) gives more thrust and lift, but a small reduction in the propulsive efficiency. Concerning the variation of the force during the period, rms values are comparable to mean values. Thrust rms values are insensitive to variations of the mean pitch value, as shown by cases A090, B090 and C090, where ${c_t}^{\mathrm{rms}} \approx 0.9$. Advancing the pitching motion increases the variation of the thrust, with ${c_t}^{\mathrm{rms}} = 0.7$, 0.9 and 1.2 for cases B070, B090 and B110, respectively. Regarding the lift, rms values are not affected by reducing the mean pitch value or lagging the pitching motion, ${c_l}^{\mathrm{rms}} \approx 2.7$ for cases A090, B070 and B090. Conversely, the rms value for the lift is slightly influenced by an increase in the mean pitch value (${c_l}^{\mathrm{rms}} = 2.9$ for case C090), and considerably affected by an advance of the pitching motion (${c_l}^{\mathrm{rms}} = 3.8$ for case B110).

After the evaluation of the average values from table 4.1, we analyze the evolution of the aerodynamic force during one period. We start analyzing the influence of the mean pitch value. Figures 4.8a and b show the evolution of thrust and lift, respectively, for cases A090, B090 and C090 during one period. Also, in order to support the following discussion, the pitch angle, θ, and the effective angle of attack, α_e, are shown in figures 4.8c and d, respectively. Case A090 generates a similar amount of thrust than case B090 during the downstroke and, notably higher during the upstroke. Conversely, case C090 ($\theta_m = 20°$) generates less thrust during the whole period, with negative values of $c_t(t)$ at

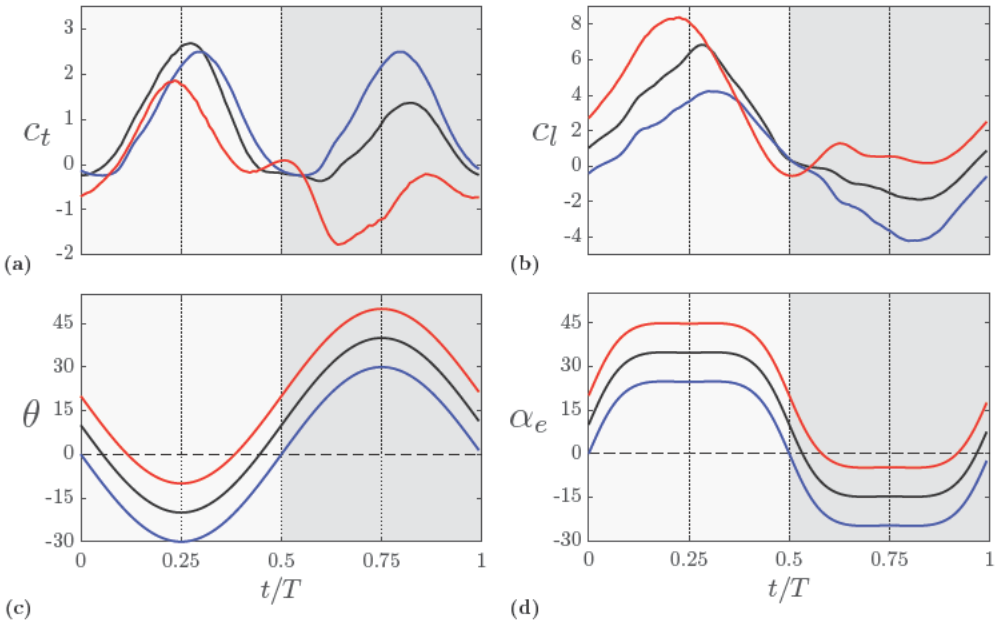

Figure 4.8: a) Thrust and b) lift coefficient, c) pitch angle and d) effective angle of attack (in degrees) of the optimum case B090 (——) with the selected cases by varying θ_m, A090 (——) and C090 (——). The downstroke (upstroke) is indicated by a light (dark) grey background.

the beginning of the upstroke, resulting in net drag ($\bar{c}_t = -0.1419$). Regarding the lift, it increases with θ_m during the whole period except in the transition from downstroke to upstroke. This transition is marked by a sudden drop in c_l associated to the detachment of the LEV, which occurs earlier for the cases with higher θ_m. This variation of c_l with θ_m is consistent with the increase of α_e with θ_m, as observed in figure 4.8d.

Concerning the effect of the phase shift, it is helpful to consider the time evolution of α_e (figure 4.9d). When $\varphi > 90°$ (B110), the profile of α_e shows a peak after the mid-downstroke, resulting in higher values of the peak force coefficients (figures 4.9a and b). When $\varphi < 90°$ (B070), the profile of α_e peaks earlier and the resulting peaks of the force coefficients are lower and broader. As a consequence, both cases B070 and B110 produce a larger thrust in the upstroke than case B090.

To increase our knowledge we continue the analysis with flow visualization. Figure 4.10 shows contours of spanwise vorticity ω_y for cases A090 (figures 4.10a, b, c and d) and C090 (figures 4.10e, f, g and h) at four equispaced time instants during one motion period. At the begining of the downstroke ($t/T = 0$), case A090 presents an LEV at the lower surface of the airfoil (figure 4.10a) due to its (negative) effective angle

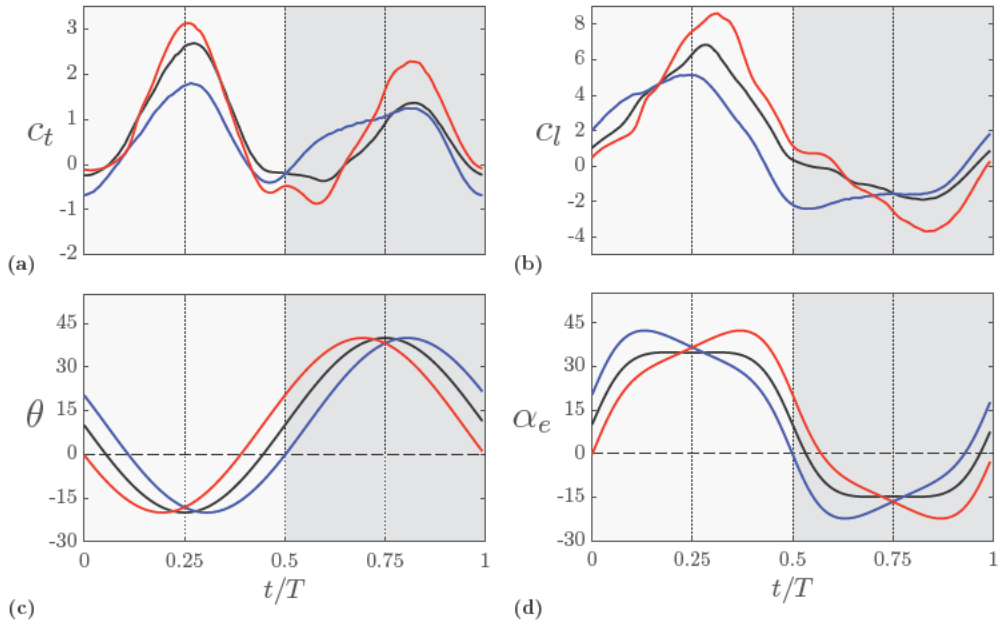

Figure 4.9: a) Thrust and b) lift coefficient, c) pitch angle and d) effective angle of attack (in degrees) of the optimum case B090 (——) with the selected cases by varying φ, B070 (——) and B110 (——). The downstroke (upstroke) is indicated by a light (dark) grey background.

of attack during this stroke (figure 4.8d). For higher mean pitch value ($\theta_m = 20°$) the effective angle of attack during the upstroke becomes smaller (in absolute value) and, as a consequence, no LEV is generated for case C090 (figure 4.10e). Instead, the shear layer created at the lower surface of the airfoil is shed into the wake forming a small vortex (figure 4.10f). As the motion of the airfoil evolves ($t/T = 0.25$), the LEV starts to grow and remains attached to the airfoil. At this moment the LEV of case A090 is starting to grow (figure 4.10b), whereas the LEV of case C090 has already a noticeable size (figure 4.10f). At the end of the downstroke ($t/T = 0.5$), the LEV of both cases is detached (figures 4.10c and g). At this time instant it can be seen that the size of the LEV increases as the mean pitch value θ_m is varied from 0° to 20°. Additionally, there is vorticity formed in the lower surface of the airfoil which is shed into the wake forming small vortex in both cases (figures 4.10c and g) and, also, a TEV created at the end of the downstroke in case C090 (figure 4.10g). Finally, at the middle of the upstroke ($t/T = 0.75$), attached flow is found in case C090 (figure 4.10h) whereas a small LEV is present in case A090 (figure 4.10d).

We now study the differences in the flow field of cases B070 and B110. Figure 4.11 shows contours of spanwise vorticity ω_y for cases B070 (figures 4.11 a, b, c and d) and

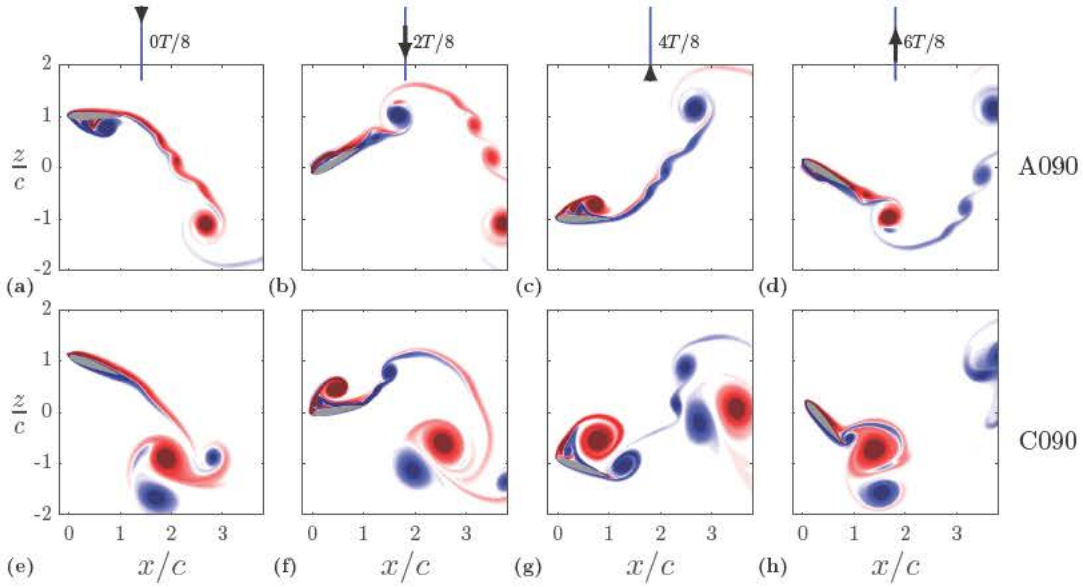

Figure 4.10: Contours of spanwise vorticity ω_y of cases with $\varphi = 90°$ A090 ($\theta_m = 0°$, top) and C090 ($\theta_m = 20°$, bottom) at four equispaced time instants. Blue corresponds to $\omega_y c/U_\infty = -15$ and red corresponds to $\omega_y c/U_\infty = 15$.

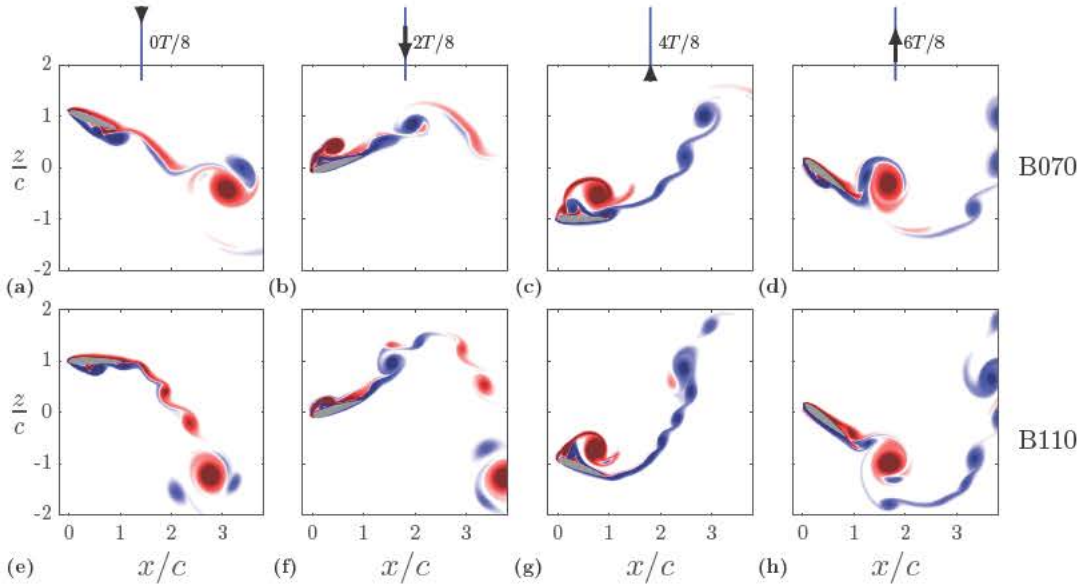

Figure 4.11: Contours of spanwise vorticity ω_y of cases with $\theta_m = 10°$ B070 ($\varphi = 70°$, top) and B110 ($\varphi = 110°$, bottom) at four equispaced time instants. Blue corresponds to $\omega_y c/U_\infty = -15$ and red corresponds to $\omega_y c/U_\infty = 15$.

B110 (figures 4.11 e, f, g and h) at four equispaced time instants during one motion period. At the begining of the downstroke, both cases present an LEV in the lower part of the airfoil (figures 4.11a and e, respectively). These cases have a (negative) peak in the effective angle of attack during the upstroke (figure 4.9d) sufficient to generate an LEV. Recall that in case B090 no LEV was generated in the upstroke (figure 4.6h). During the first half of the downstroke the effective angle of attack increases as the phase shift is reduced from 110° to 70°, so at the middle of the downstroke ($t/T = 0.25$), the size of the LEV increases as the phase shift is reduced from 110° to 70° (figures 4.11b and f). During the second half of the downstroke ($0.25 < t/T < 0.5$) the behavior of the effective angle of attack with the phase shift is changed, α_e increases as φ is increased from 70° to 110° (figure 4.9f). As a result, when the LEV is being detached at the end of the downstroke ($t/T = 0.5$), the size of the LEV of the two cases is similar (figures 4.11c and g). Once the LEV is shed into the wake, the LEV of both cases presents different interactions with the vorticity shed through the TE, but the flow structure is similar (figures 4.11d and h). Finally, the (negative) peak of α_e of cases B070 and B110 occurs before the middle of the upstroke ($t/T < 0.75$) in the former and after the middle of the upstroke ($t/T > 0.75$) in the latter. Therefore, only the LEV of case B070 is present at the middle of the upstroke (figures 4.11d and h), although at the end of the downstroke both cases present an LEV in the lower part of the airfoil (figures 4.11a and e).

CHAPTER
FIVE

Force decomposition and modelling [1]

The aerodynamic forces produced by flapping airfoils were studied in the previous chapter. Now, the total value of the force is decomposed in different contributions in order to get insights of the mechanisms at play. This chapter has been organised in the following way. First, the algorithm used to decompose the force is described. Then, the reference case selected in the previous chapter is analyzed in detail. Also, the influence of the motion parameters on the different contributions of the force is studied. Finally, we make use of an existing model from the literature to estimate the aerodynamic forces and, based on observations made through this chapter, propose a modification of the model to improve its performance.

5.1 Numerical method

The total aerodynamic force is decomposed using the algorithm proposed by Chang [1992] and recently used by Martín-Alcántara et al. [2015]. The total aerodynamic force components in the streamwise (x) and vertical (z) directions are expressed as

$$\begin{aligned} F_x = &- \rho \int_S \frac{\phi_x}{U_\infty} \frac{\partial \vec{u}}{\partial t} \cdot \vec{n} \, \mathrm{d}S + \frac{\rho}{2} \int_S |\vec{u}|^2 \vec{n} \cdot \vec{e}_x \, \mathrm{d}S \\ &- \rho \int_V (\vec{u} \times \vec{\omega}) \cdot \frac{\nabla \phi_x}{U_\infty} \, \mathrm{d}V + \mu \int_S (\vec{\omega} \times \vec{n}) \cdot (\frac{\nabla \phi_x}{U_\infty} + \vec{e}_x) \, \mathrm{d}S, \end{aligned} \tag{5.1a}$$

$$\begin{aligned} F_z = &- \rho \int_S \frac{\phi_z}{U_\infty} \frac{\partial \vec{u}}{\partial t} \cdot \vec{n} \, \mathrm{d}S + \frac{\rho}{2} \int_S |\vec{u}|^2 \vec{n} \cdot \vec{e}_z \, \mathrm{d}S \\ &- \rho \int_V (\vec{u} \times \vec{\omega}) \cdot \frac{\nabla \phi_z}{U_\infty} \, \mathrm{d}V + \mu \int_S (\vec{\omega} \times \vec{n}) \cdot (\frac{\nabla \phi_z}{U_\infty} + \vec{e}_z) \, \mathrm{d}S, \end{aligned} \tag{5.1b}$$

where $\vec{u}$ is the velocity of the flow, $\vec{\omega}$ is the vorticity, μ is the dynamic viscosity of the fluid, S the surface of the airfoil, V the fluid domain, $\vec{n}$ the unitary vector normal to

[1] The content of this chapter is contained in the following publication:
Moriche, M., Flores, O., and García-Villalba, M. On the aerodynamic forces on heaving and pitching airfoils at low Reynolds number. In *J. Fluid Mech.*, 2017, Submitted

the surface of the airfoil, pointing towards the fluid and $\vec{e}_x$ and $\vec{e}_z$ the unitary vectors in the x and z directions, respectively. The auxiliary potentials ϕ_x and ϕ_z that appear in equation (5.1) depend only on the geometry of the airfoil and on the directions in which they are computed. For details of the calculations of these functions, the reader is referred to the appendix C.1.

Following Chang [1992], we group the terms of equation (5.1) to identify different mechanisms in the force generation process. The first two terms of the right hand side in equation (5.1) are the contribution due to the motion of the body, ${F_x}^m$ and ${F_z}^m$. The contribution of the vorticity within the flow, ${F_x}^v$ and ${F_z}^v$, is given by the third term. Finally, the surface vorticity contribution, ${F_x}^s$ and ${F_z}^s$, is the last term. This decomposition presents some advantages with respect to other algorithms from the literature. First, the contribution of the body motion is calculated with surface integrals which only involve the velocity of the flow and the auxiliary potential functions, both on the surface of the airfoil, and hence prescribed by the geometry and the kinematics of the airfoil. Second, the only time derivative of the fluid velocity in equation (5.1) appears in a surface integral, so that $\frac{\partial \vec{u}}{\partial t}$ can be evaluated from the kinematics of the airfoil. This means that this force decomposition algorithm can be applied to isolated snapshots of the velocity field, e.g. obtained from particle image velocimetry measurements. Finally, the integrand of the contribution of the vorticity within the flow can be interpreted as a force density, allowing a direct evaluation of how specific regions of the flow contribute to the total aerodynamic force.

In accordance with the decomposition explained above, the total non-dimensional force coefficients are expressed in terms of the different contributions shown in equation (5.1).

$$c_t = {c_t}^m + {c_t}^v + {c_t}^s \tag{5.2a}$$

$$c_l = {c_l}^m + {c_l}^v + {c_l}^s \tag{5.2b}$$

Furthermore, we define the spatial distribution of thrust δ_t and lift δ_l density as the integrand of the contribution of the vorticity within the flow to the total aerodynamic force in equation (5.1). After non-dimensionalization, the definitions of δ_t and δ_l read

$$\delta_t = \frac{2\,(\vec{u} \times \vec{\omega}) \cdot \nabla \phi_x}{{U_\infty}^3 c^2}, \tag{5.3a}$$

$$\delta_l = \frac{-2\,(\vec{u} \times \vec{\omega}) \cdot \nabla \phi_z}{{U_\infty}^3 c^2}. \tag{5.3b}$$

5.2 Force decomposition of a reference case

In this section we decompose the total aerodynamic force of case B090, as described in section 5.1, and model each contribution separately. Figure 5.1 shows the evolution of the

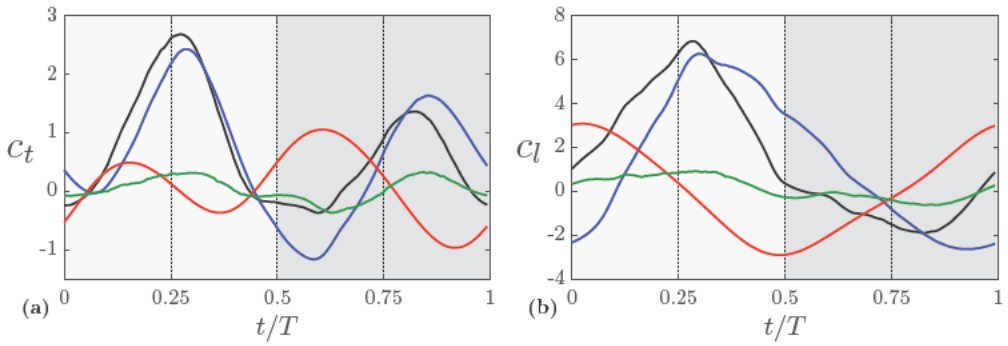

Figure 5.1: a) Thrust and b) lift coefficient of case B090. Curves represented correspond to the total aerodynamic force (——) and contributions from body motion (——), vorticity within the flow (——) and surface vorticity (——). The downstroke (upstroke) is indicated by a light (dark) grey background.

total thrust and lift, together with the contributions from body motion, vorticity within the flow and surface vorticity during one period of case B090. The main contribution to the total aerodynamic force corresponds to the vorticity within the flow, with peak values of the same order of magnitude as the total value of the force. Body motion has also an important role in the generation of force, producing peak values around half of the peak values of the total aerodynamic force. Finally, surface vorticity (viscous effects) is the least important contribution, with peak values approximately ten times smaller than the total force peak values. Therefore, in the following we will focus in the analysis of the contributions from body motion and the vorticity within the flow.

We start with the contribution of the body motion to the total force, $\vec{F}^m$, which is the force produced by the fluid to counteract the motion of the airfoil. This is easily observed in figure 5.1b: when $\ddot{h} < 0$, ${c_l}^m$ is a positive vertical force, and viceversa. The thrust (figure 5.1a) is influenced by both the vertical acceleration and the projected area of the airfoil perpendicular to the streamwise direction. For the motion parameters of this case ($\theta_m = 10°$, $\varphi = 90°$), the projected area during the downstroke is smaller than the projected area during the upstroke, resulting in higher peaks of ${c_t}^m$ in the latter.

In potential theory, the contribution of the body motion is referred to as added mass or non-circulatory effects. To highlight the difference between this contribution and added mass, we obtain the analytic solution of ${c_t}^m$ and ${c_l}^m$ for a flat plate of chord c

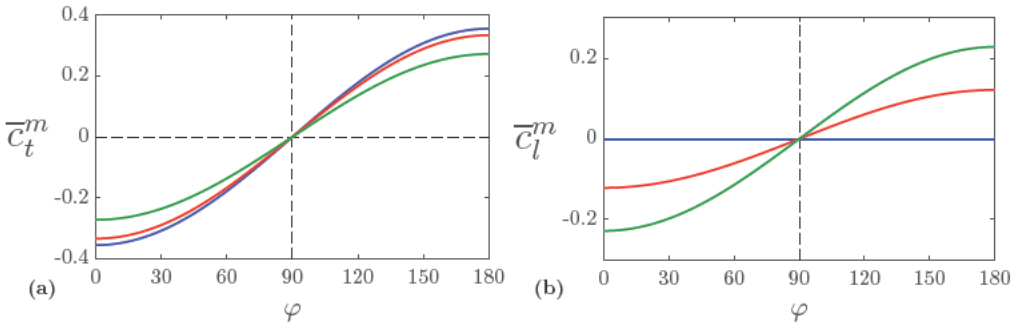

Figure 5.2: Mean a) thrust and b) lift coefficients from body motion contribution for a flat plate with respect to the phase shift φ (in degrees). The values shown correspond to different values of mean pitch angle, $\theta_m = 0°$ (——), $\theta_m = 10°$ (——) and $\theta_m = 20°$ (——).

pivoting aroung the middle of the chord

$$c_t{}^m = \frac{\pi}{4}\frac{\ddot{h}}{{U_\infty}^2/c}\sin(2\theta)\,, \tag{5.4a}$$

$$c_l{}^m = -\frac{\pi}{2}\frac{\ddot{h}}{{U_\infty}^2/c}\cos^2(\theta)\,, \tag{5.4b}$$

and compare them with the expressions for the added mass forces, $c_t{}^a$ and $c_l{}^a$, given by Sedov et al. [1965]

$$\begin{aligned} c_t{}^a =& \frac{\pi}{4}\frac{\ddot{h}}{{U_\infty}^2/c}\sin(2\theta) + \frac{\pi}{2}\frac{\dot{h}}{U_\infty}\frac{\dot{\theta}}{U_\infty/c}\cos(2\theta) \\ &- \frac{2\pi}{9}\left(\frac{\dot{\theta}^2}{{U_\infty}^2/c^2}\cos\theta + \frac{\ddot{\theta}}{{U_\infty}^2/c^2}\sin\theta\right), \end{aligned} \tag{5.5a}$$

$$\begin{aligned} c_l{}^a =& -\frac{\pi}{2}\frac{\ddot{h}}{{U_\infty}^2/c}\cos^2\theta + \frac{\pi}{2}\frac{\dot{h}}{U_\infty}\frac{\dot{\theta}}{U_\infty/c}\sin(2\theta) \\ &+ \frac{\pi}{9}\left(\frac{\ddot{\theta}}{{U_\infty}^2/c^2}\cos\theta - \frac{\dot{\theta}^2}{{U_\infty}^2/c^2}\sin\theta\right). \end{aligned} \tag{5.5b}$$

The auxiliary potentials used for the calculations are those of an ellipse with a minor axis of length zero and a major axis of length c [Martín-Alcántara et al., 2015]. It can be seen that when the pitching motion is not included ($\dot{\theta} = 0$), the body motion contribution is equal to the added mass but, in general, they are different. Furthermore, for periodic motions both $c_t{}^a$ and $c_l{}^a$ integrate to zero over one motion period, whereas this does not happen, in general, for $c_t{}^m$ and $c_l{}^m$. Figures 5.2a and b show the mean values of equation (5.4) integrated over one motion period. All the motion parameters used are the same as in the database presented in chapter 4, except for the pivoting point, which is located at the middle of the chord $x_p = c/2$. It can be seen that when the phase shift

is lower than 90°, mean drag and mean negative lift are generated. Conversely, both thrust and lift are generated when the phase shift is higher than 90°. It is therefore shown that the body motion contribution does not, in general, integrate to zero for a periodic motion. Note that, although we cannot use the expressions of added mass to calculate the body motion contribution, this term needs not to be modelled. The velocity on the surface of the airfoil is known from the kinematics and the potentials need only to be computed once (see appendix C.1). Furthermore, for the NACA 0012 airfoil used in this work, the values for the auxiliary potentials ϕ_x and ϕ_z are given in figure C.2.

Now we are going to analyze the effect that the contribution of the vorticity within the flow has on the total aerodynamic force. Figures 5.1a and b show the evolution of ${c_t}^v$ and ${c_l}^v$, respectively, for case B090 during one period. It is clear that the (positive) peaks of total thrust and lift are dominated by the contribution of the vorticity within the flow. The first peak of ${c_t}^v$ ($t/T \approx 0.25$) represents 90% of the total thrust, the second ($t/T \approx 0.75$) 120%, and the peak of ${c_l}^v$ ($t/T = 0.25$) 92% of the total lift. Also, the contribution of the vorticity with the flow is maximum when the vertical velocity of the airfoil $\dot{h}$ and the effective angle of attack α_e are maximum. Therefore, two peaks of positive thrust are observed in figure 5.1a at the middle of the downstroke ($t/T = 0.25$) and at the middle of the upstroke ($t/T = 0.75$), respectively. Regarding the lift, the peak of force generated at the middle of the downtroke ($t/T = 0.25$) is positive and the one generated at the middle of the upstroke ($t/T = 0.75$), negative. The assymetry introduced by the mean pitch angle $\theta_m = 10°$ results in lower peak values in the upstroke compared to the downstroke, which is detrimental for the thrust, but favourable for the lift.

In order to obtain a better understanding, we continue the analysis of case B090 by comparing the vorticity and force density fields at four equispaced time instants during one period, shown in figure 5.3. Each row of figure 5.3 is composed of the contours of ω_y, δ_t and δ_l at the same time instant, which is indicated at the right of each row. The first thing to observe is how both thrust δ_t and lift δ_l densities (figures 5.3b, e, h, k and 5.3c, f, i, l, respectively) decay fast with the distance to the airfoil for any time instant, as previusly observed by other authors [Chang, 1992, Martín-Alcántara et al., 2015]. This occurs because the force density is the projection of the Lamb's vector on the gradient of the potentials ϕ_x and ϕ_z, which decay quadratically with the distance to the airfoil [Martín-Alcántara et al., 2015]. Regarding the evolution of vorticity (figures 5.3a, d, g and j) the LEV is created during of the downstroke (5.3d) and shed into the wake approximately in the transition from downstroke to upstroke (5.3j). After being shed (5.3j), the LEV is advected into the wake (5.3a, d and g). The evolution of thrust (figures 5.3b, e, h and k) and lift (5.3c, f, i and l) densities show that vortical structures have a negligible effect on the aerodynamic force once they have been shed into the wake.

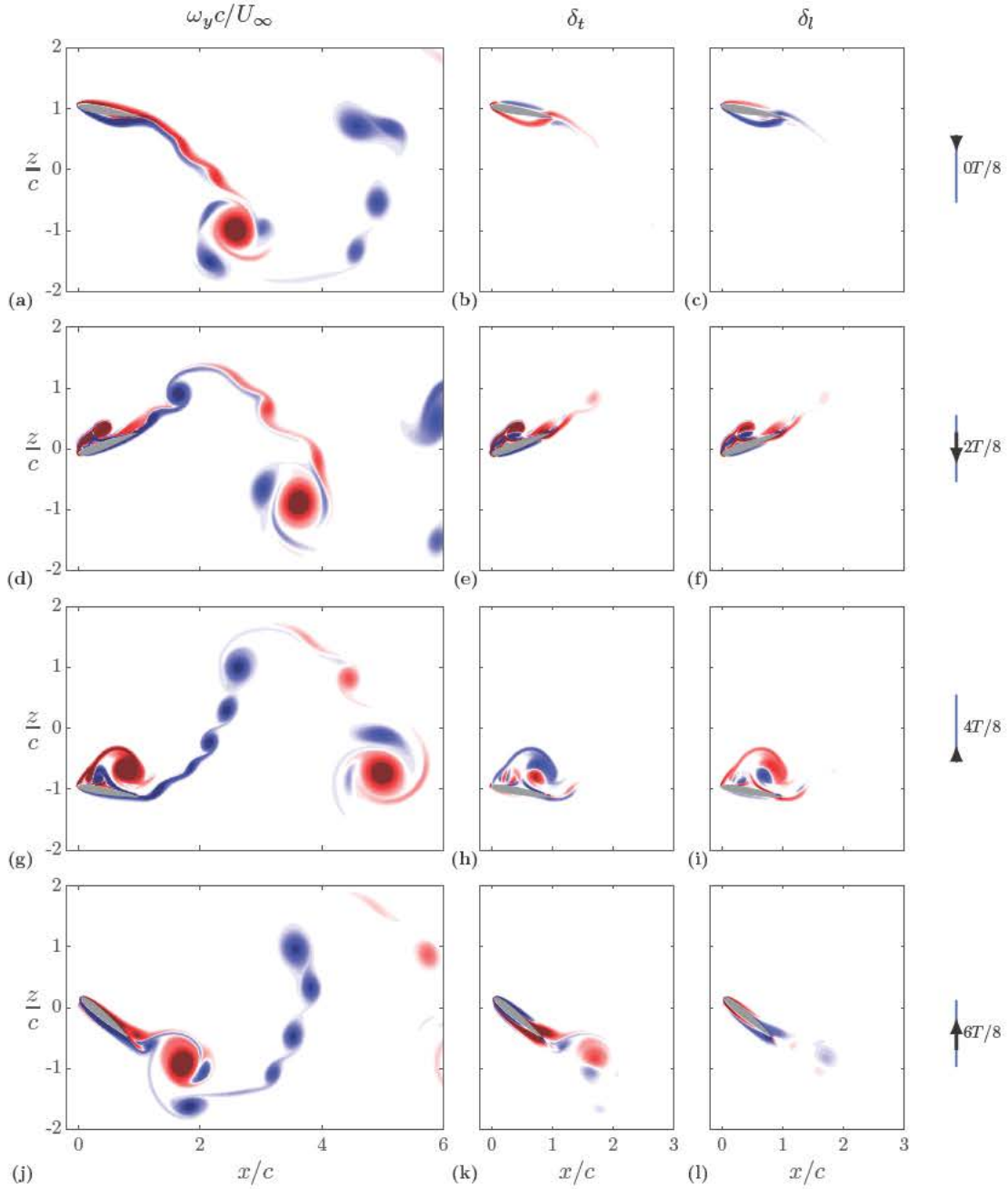

Figure 5.3: Contours of spanwise vorticity ω_y (a, d, g and j), thrust density δ_t (b, e, h and k) and lift density δ_l (c, f, i and l) of case B090 at four time instants. Blue corresponds to $\omega_y c/U_\infty = -15$, $\delta_t = -10$ and $\delta_l = -50$ and red corresponds to $\omega_y c/U_\infty = 15$, $\delta_t = 10$ and $\delta_l = 50$.

Note how the contribution of the LEV to the thrust (5.3e and h) and lift (5.3f and i) is partially positive and negative. This is an inherent property of any vortex, as indicated by Chang [1992] in his work. The center of a vortex is characterized by a change of direction of the Lamb's vector while the gradient of the auxiliary potentials is locally smooth, so a line where the sign of the force density changes its sign must pass through the center of the vortex. Which part of the vortex (positive and negative contribution to the force) dominates, depends on the vorticity field and on the gradients of the auxiliary potentials, which are determined only by the geometry of the airfoil. This is an interesting fact since one may think that with a smart modification of the geometry, a better performance in terms of aerodynamic forces could be obtained. Finally, when the LEV starts to detach ($t/T = 0.5$), there is a change in its contribution to the thrust (figures 5.3e and h), while its contribution to the lift is maintained (figures 5.3f and i).

It is clear from the previous discussion that the contribution of the vorticity within the flow is the dominant contribution to the total aerodynamic force. Therefore it is of great interest to understand how this part of the force behaves. In steady-state aerodynamics, Kutta-Joukowsky theorem predicts the aerodynamic force due to the vorticity within the flow on a body with circulation Γ is

$$\vec{F}_{KJ} = \rho\left(\vec{U} \times \Gamma\, \vec{e}_y\right), \tag{5.6}$$

where the subscript KJ denotes Kutta-Joukowsky estimation and $\vec{U}$ is the free stream velocity seen by the airfoil. The force estimated by Kutta-Joukowsky theorem is perpendicular to the incoming effective velocity, which can be estimated for a heaving and pitching airfoil as the sum of the free stream ($U_\infty \vec{e}_x$) and heaving ($\dot{h}\vec{e}_z$) velocities, as described in Pesavento and Wang [2004], Andersen et al. [2005] and Taha et al. [2014]. In this work, we proceed to verify if Kutta-Joukowsky theorem still holds in these flow conditions. For that, we define σ as the angle between $\vec{F}^v$ and the direction of the force predicted by Kutta-Joukowsky, perpendicular to the effective incoming velocity (see figure 5.4). Note that a zero value for σ would mean that Kutta-Joukowsky theorem is fulfilled. Figure 5.5a shows the evolution of the angle σ for case B090 during one period. The line representing the angle σ in figure 5.5a is coloured with a grey scale according to the modulus of $\vec{F}^v$. The colour scale employed to represent σ is used to avoid confusion of the reader by the discontinuities that take place when the modulus of $\vec{F}^v$ approaches zero, a situation where σ is ill defined. The evolution of the effective angle of attack $\alpha_e = \theta - \text{atan}(\dot{h}/U_\infty)$ has been also included in the figure, and it can be clearly seen that the angle σ is approximately equal to the effective angle of attack α_e, except for specific time instants where the force is small. This means that $\vec{F}^v$ is not normal to the incoming effective velocity, but to the airfoil chord. This observation is consistent with the results of Dickinson et al. [1999], where the aerodynamic forces were normal to the wing section (a flat plate). All the periodic cases of our database show the same

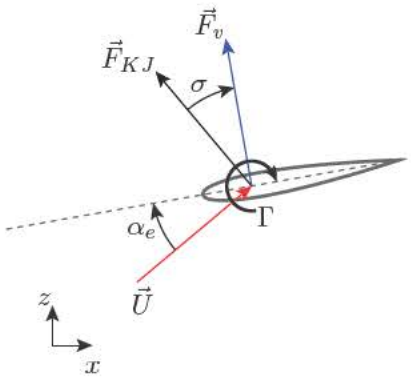

Figure 5.4: Sketch of the deviation angle σ and effective angle of attack.

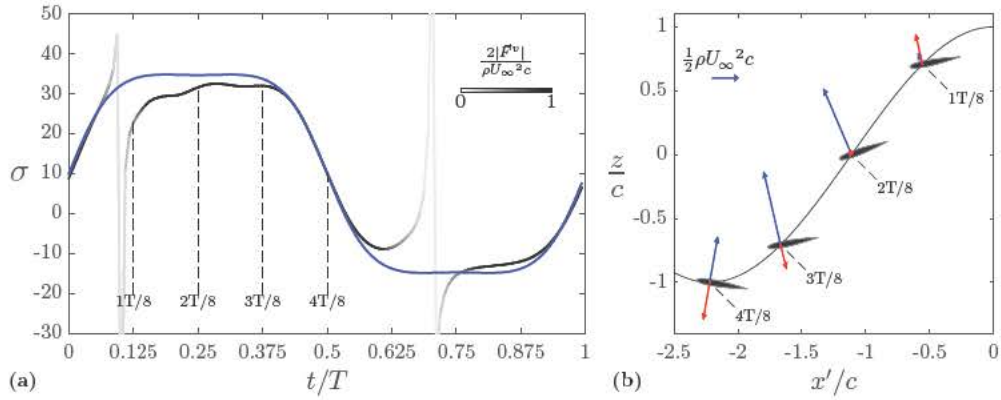

Figure 5.5: a) Evolution of angle σ (in degrees) of case B090 during one period. The curves represented are the angle σ in gray scale to indicate the modulus of the $\vec{F}^v$ and the effective angle of attack (——). b) Vectors of $\vec{F}^v$ (——) and $\vec{F}^m$ (——) at four time instants during the downstroke of case B090.

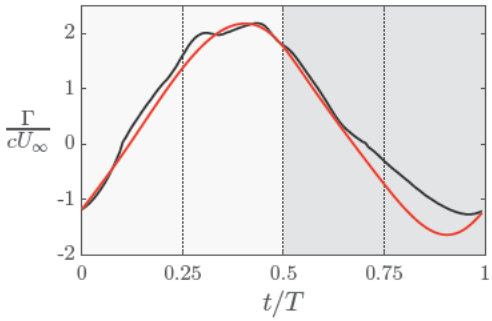

Figure 5.6: Circulation of the airfoil for case B090. The curves represented correspond to the values obtained from the DNS (——) and the model best fit (——) with $G_T = 1.65$ and $G_R = 3.73$. The downstroke (upstroke) is indicated by a light (dark) grey background.

orthogonality of $\vec{F}^v$ and the airfoil chord (see figures A.3, A.4 and A.5). Figure 5.5b shows a sketch of $\vec{F}^v$ acting on the airfoil at four equispaced time instants. In the sketch, the airfoil trajectory represented is seen by an observer travelling with the free stream, so the horizontal coordinate is defined as $x' = x - U_\infty t$. It can be seen that when $\vec{F}^v$ is not perpendicular to the airfoil ($t/T = 0.125$) the modulus of the force is small and, when the modulus is large enough, $\vec{F}^v$ tends to be perpendicular to the airfoil.

From the point of view of modelling the contribution of the vorticity within the flow to the aerodynamic force, the results of figure 5.5 provide the direction, so an estimation of the modulus is still needed. Based on potential theory, we choose to model the circulation Γ of the airfoil and, then, obtain the modulus of the contribution of vorticity within the flow to the force as

$$|\vec{F}^v| = \rho\Gamma|\vec{U}|. \tag{5.7}$$

We use the model of Pesavento and Wang [2004] to estimate the circulation Γ of the airfoil. They propose that the circulation of an airfoil is given by

$$\Gamma = \frac{1}{2}G_T\, c \left|\vec{U}\right| \sin(2\alpha_e) + \frac{1}{2}G_R\, c^2\dot{\theta}, \tag{5.8}$$

where G_T and G_R are constants that need to be set by a fitting procedure. We fit the circulation given by the model to the circulation obtained from the DNS of case B090 to obtain values for G_T and G_R. We use the L_2 norm of the difference between the circulation obtained from the DNS and the circulation predicted by the model as the objective function to minimize in the fitting procedure. The circulation from the DNS is calculated using equation (5.7) and the appropriate sign. Figure 5.6 shows the circulation obtained from the DNS and the best fit of the model for case B090. It can

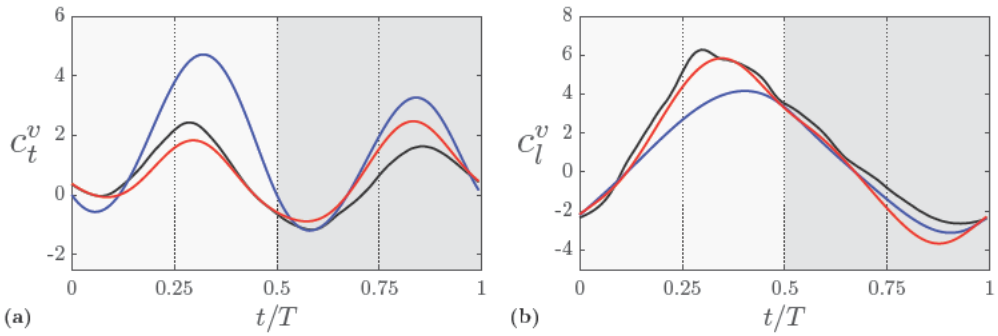

Figure 5.7: Evolution of a) $c_t{}^v$ and b) $c_l{}^v$ of case B090 during one period. The curves represented correspond to the values obtained from the DNS (——), the Kutta-Joukowsky estimation (——) and the chord-normal estimation (——). The circulation in both estimations is given by the model from Pesavento and Wang with $G_T = 1.65$ and $G_R = 3.73$, The downstroke (upstroke) is indicated by a light (dark) grey background.

be seen that the agreement is very good, so the circulation, and hence the modulus of $\vec{F}^v$ is very well captured by the model of Pesavento and Wang [2004].

Therefore, we propose that a good estimate of $\vec{F}^v$ is a force oriented normal to the chord whose modulus is calculated with equation (5.7) (using equation (5.8) for the circulation Γ). Figure 5.7a shows the evolution of the $c_t{}^v$ obtained from the DNS together with the chord-normal estimation for case B090. Kutta-Joukowsky prediction is also included in the figure for comparison purposes. The results show that peak values of thrust are properly predicted by the chord-normal force, but overestimated by Kutta-Joukowsky theorem. Regarding the lift, figure 5.7b shows that the value of $c_l{}^v$ obtained in case B090 is very well represented by the chord-normal estimation.

5.3 Extension of the analysis to the database

In this section we extend the analysis performed in the previous section to case B090 to a subset of cases from the database. The objective of extending the analysis is to see how the different contributions to the total aerodynamic force are influenced by the motion parameters θ_m and φ. We select the cases A090, C090, B070 and B110 and use the results of case B090 as a reference.

We start describing the evolution of the contribution of vorticity within the flow to the total aerodynamic force. Figures 5.8a and b show the evolution of $c_t{}^v$ and $c_l{}^v$, respectively, for the selected cases. An increase of the mean pitch value (case C090) results in a reduction of the contribution of the vorticity within the flow to the thrust

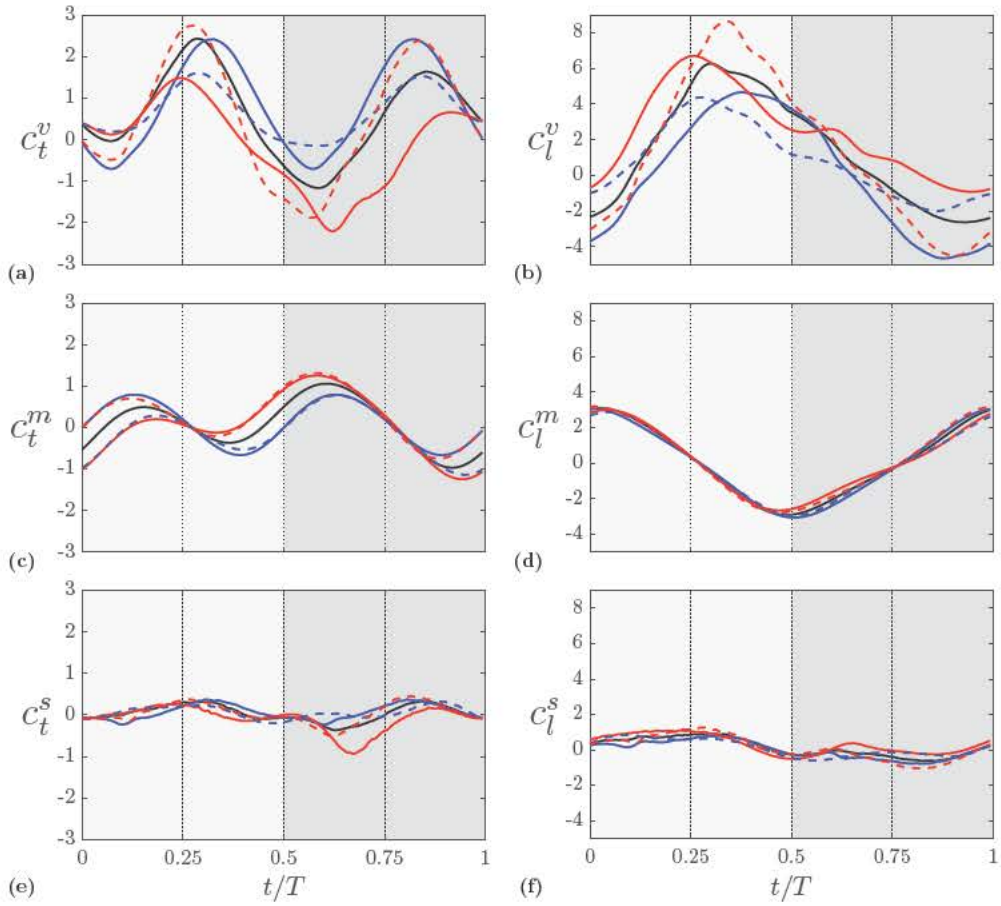

Figure 5.8: Contribution of a) vorticity within the flow, c) body motion and e) surface vorticity to the total aerodynamic thrust. The lift contributions are shown in b), d) and f), respectively. Four cases with different motion parameters are represented: case B090 (——), case A090 (——), case C090 (——), case B070 (- - -) and case B110 (- - -). The downstroke (upstroke) is indicated by a light (dark) grey background.

(figure 5.8a) and an increase of the contribution to the lift (figure 5.8b). The reduction of θ_m (case A090) produces the opposite effect, except for the first half of the downstroke ($0 < t/T < 0.25$) in the case of thrust, and for the transition from downstroke to upstroke ($t/T \approx 0.5$) in the case of lift. This means that the mean pitch value θ_m introduces an offset in the contribution of the vorticity with in the flow to the aerodynamic forces. The variation of phase shift produces a different effect, affecting mainly to the peak values of $\vec{F}^v$. An advance of the pitching motion (case B110) results in more pronounced peak values (positive and negative) in both the thrust (figure 5.8a) and lift (figure 5.8b), whereas lagging the pitching motion (case B070) results in a reduction of the peak values.

Figures 5.8c and d show the evolution of ${c_t}^m$ and ${c_l}^m$, respectively, for the selected cases. For the motion under study, the heaving acceleration $\ddot{h}(t)$ dominates the contribution of body motion to the lift, independently of the parameters θ_m and φ (figure 5.8d). Concerning the thrust, both the heaving acceleration $\ddot{h}(t)$ and the projected area of the airfoil perpendicular to the streamwise direction, influence the amount of ${c_t}^m$. Therefore, ${c_t}^m$ vanishes at points where the heaving acceleration $\ddot{h}(t)$ is zero ($t/T = 0.25, 0.75$) and, at points where the heaving acceleration $\ddot{h}(t)$ is maximum ($t/T = 0, 0.5$), the amount of ${c_t}^m$ depends on the area of the airfoil projected perpendicular to the streamwise direction. This area is related to the value of the pitch angle θ (figures 4.8c and 4.9c). At the beginning of the downstroke ($t/T = 0$), cases A090 and B110 have a pitch angle θ of $0°$, so they generate almost no ${c_t}^m$ (figure 5.8c). At this time instant, if the pitch angle increases, ${c_t}^m$ increases accordingly to the value of the pitch angle, so case B090 generates more thrust than cases A090 and B110 and less than cases C090 and B070. The same analysis holds at the beginning of the upstroke ($t/T = 0.5$), except that, in this part of the period, cases with different phase shift (B070 and B110) interchange their role.

To conclude the analysis of the different contributions to the total aerodynamic force, figures 5.8e and f show the evolution of the surface vorticity contribution to the total aerodynamic thrust and lift, respectively. It can be seen that the effects that surface vorticity has on the forces is small compared to the other contributions for both thrust and lift, except for a peak of viscous drag in the upstroke of case C090.

After describing the evolution of the different contributions to the total aerodynamic force, we proceed to investigate the capability of the chord-normal model to predict the contribution of the vorticity within the flow to the total aerodynamic force of the subset of cases A090, C090, B070 and B110. In order to do that, we follow the same approach as we did with case B090 in section 5.2, calculating the coefficients G_T and G_R by a fitting process. Table 5.1 shows the values of the L_2 norm of the difference between the circulation obtained from the DNS and the estimated by the model. Ideally, fixed values for G_T and G_R are desired, so we show the results obtained with coefficients obtained

Case	θ_m	φ	G_T	G_R	$L_2(\Gamma_{DNS} - \Gamma)$	
					Specific	Fixed
B090	0.00°	90.00°	1.65	3.73	0.26	0.32
A090	10.00°	90.00°	1.44	4.48	0.13	0.43
C090	20.00°	90.00°	1.95	2.14	0.42	0.50
B070	10.00°	70.00°	1.65	2.46	0.14	0.20
B110	10.00°	110.00°	1.34	4.58	0.35	0.50

Table 5.1: Coefficients of Pesavento and Wang [2004] model for circulation (equation (5.8)) obtained from the best fit with the data from the DNS for the selected cases. The errors shown correspond to the circulation obtained with the coefficients obtained specifically for each case (next-to-last) column and fixed coefficients $G_T = 1.85$ and $G_R = \pi$ (last column).

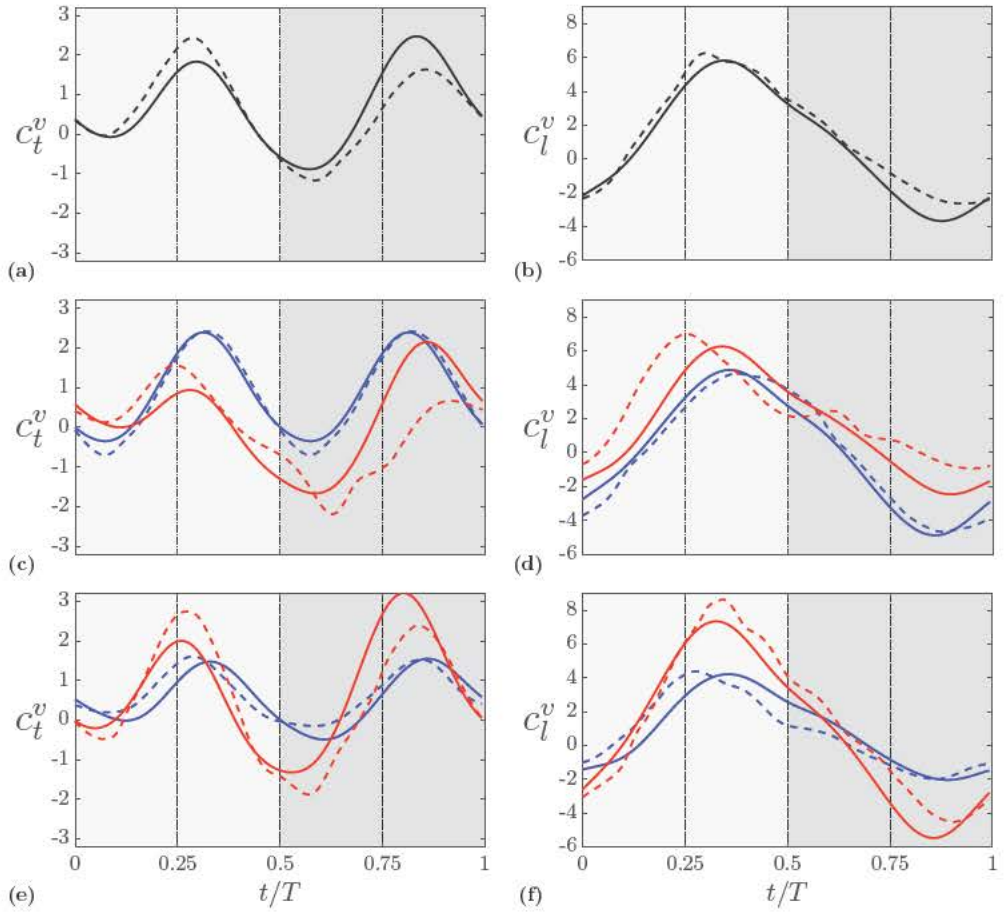

Figure 5.9: Chord-normal estimation of the contribution of vorticity within the flow for the selected cases. The circulation is given with the model (equation (5.8)) with coefficients $G_T = 1.85$ and $G_R = \pi$. a) Thrust and b) lift of case B090 (DNS - - - and model ——). c) Thrust and d) lift of cases A090 (DNS - - - and model ——) and C090 (DNS - - - and model ——). e) Thrust and f) lift of cases B070 (DNS - - - and model ——) and B110 (DNS - - - and model ——). The downstroke (upstroke) is indicated by a light (dark) grey background.

by fitting process independent for each case (next-to-last column in table 5.1, "specific") and fixed coefficients for all the cases under study (last column in table 5.1, "fixed"). The procedure to obtain the fixed coefficients is described briefly below. If we look at the expression for the circulation given in equation (5.8), the rotational term is easily related to the expression for rotational circulation obtained from potential theory for a thin airfoil

$$\Gamma_{ROT} = \pi\, c^2 \dot{\theta} (\frac{3}{4} - \frac{x_p}{c}). \tag{5.9}$$

Therefore, we set $G_R = \pi$ and then obtain $G_T = 1.85$ by a fitting process of all the periodic cases with phase shift between $\varphi = 50°$ and $130°$, both included. The L_2 norm of the difference between the fitted and the DNS circulations are of the same order of the magnitude for specific and fixed coefficients. Hence, from now on we use the fixed coefficients to calculate the circulation of all the selected cases.

Figures 5.8a and b show the evolution of ${c_t}^v$ and ${c_l}^v$ given by the chord-normal estimation with fixed coefficients for the circulation, respectively, for case B090. The resulting forces are similar to those when using specific coefficients for this case (figure 5.7). Figures 5.8c and d show the evolution of ${c_t}^v$ and ${c_l}^v$, respectively, for cases A090 and C090. Both ${c_t}^v$ and ${c_l}^v$ are properly predicted for case A090, but higher differences between the chord-normal estimation and the results obtained from the DNS are found for case C090. For the latter, peaks of thrust predicted by the model present differences of more than 50% with respect to the results from the DNS. Also, the (positive) peak of lift at $t/T = 0.25$ presents a phase shift of approximately $T/8$. Figures 5.8e and f show the evolution of ${c_t}^v$ and ${c_l}^v$, respectively, of the chord normal estimation together with the results obtained from the DNS for cases B070 and B110. The prediction of ${c_t}^v$ of case B070 is very good, although the peak of thrust predicted in the downstroke is a little advanced with respect to the result of the DNS. Regarding the lift, peak values of ${c_l}^v$ of case B070 obtained from the DNS and the predictions from the model are similar, only presenting a small phase shift between them. Finally, ${c_t}^v$ of case B110 (figure 5.8e) is underestimated in the downstroke and overestimated in the upstroke. The prediction of ${c_l}^v$ for case B110 (figure 5.8f) is a little underestimated from the middle of the downstroke to the middle of the upstroke ($0.25 < t/T < 0.75$).

5.4 Prediction of total values

Finally, we estimate the total aeordynamic force taking into account the results obtained throughout the manuscript. We present two different models, namely S+PW+KJ (Sedov, Pesavento and Wang and Kutta-Joukousky) and CH+PW+CN (Chang, Pesavento and Wang and chord-normal). Both models are the result of combining a term that

Table 5.2: Mean thrust and lift coefficients obtained from the DNS and an estimation taken from the literature (S+PW+KJ, model 1) and the estimation proposed in the present work (CH+PW+CN, model 2).

	$\overline{c}_t - \overline{c}_{tDNS}$		$L_2\left(c_t - c_{tDNS}\right)$		$\overline{c}_l - \overline{c}_{lDNS}$		$L_2\left(c_l - c_{lDNS}\right)$	
Case	mod. 1	mod. 2	mod. 1	mod. 2	mod. 1	mod. 2	mod. 1	mod. 2
A030	0.226	1.109	0.444	1.168	0.004	0.004	1.426	2.428
A050	0.106	0.785	0.402	0.994	0.000	0.000	0.689	1.793
A070	−0.066	0.513	0.131	0.808	−0.000	−0.000	0.268	1.004
A090	0.116	0.835	0.471	1.173	0.000	0.000	0.796	0.316
A110	0.246	1.400	0.876	1.654	−0.000	−0.000	1.245	1.040
A130	0.287	2.096	1.181	2.221	0.005	0.005	1.896	2.235
B030	0.065	0.864	0.395	1.196	0.102	−0.011	1.503	2.368
B050	0.042	0.724	0.355	1.195	−0.108	−0.043	1.038	1.953
B070	−0.018	0.634	0.236	1.109	0.024	0.256	0.766	1.658
B090	0.166	0.995	0.620	1.377	0.557	0.913	0.699	1.182
B110	0.209	1.467	0.852	1.766	0.597	1.014	1.107	1.404
B130	0.311	2.179	1.181	2.396	0.805	1.209	1.934	2.511
C030	0.628	1.176	1.077	1.717	0.984	0.732	2.593	2.859
C050	0.693	1.358	0.874	1.683	1.345	1.388	2.118	2.427
C070	0.094	0.926	0.223	1.647	0.307	0.637	1.409	2.179
C090	0.432	1.544	1.075	2.026	1.032	1.587	1.617	2.400
C110	0.336	1.861	1.136	2.271	1.240	1.919	1.569	2.415
C130	0.457	2.470	1.405	2.890	1.642	2.324	2.239	3.159

represents the contribution from body motion and a term that represents the contribution from vorticity within the flow. Viscous terms are neglected in both models. The body motion contribution in the first model (S+PW+KJ) is calculated with expressions from Sedov et al. [1965] for the added mass terms of a flat plate. In the second model (CH+PW+KJ) we use the expressions derived by Chang [1992] (first and second terms in the right hand side of equation (5.1)). The modulus of the contribution from vorticity within the flow is estimated in both models by the quasi-steady model of Pesavento and Wang [2004] with fixed coefficients $G_T = 1.85$ and $G_R = \pi$. The orientation of this contribution is given by Kutta-Joukowsky theorem in the model S+PW+KJ, and by the chord-normal direction in the model CH+PW+CN.

Table 5.2 shows the mean and the L_2 norm of the difference between the forces obtained from the DNS and the predictions of both models, for the whole database (see table 4.1). The error produced in mean values is useful to know how good the resultant force is captured but, if positive and negative errors compensate each other, this metric

will not make it visible. For that, we also show error in L_2, which measures how similar is the evolution of both signals during the cycle.

Starting with the thrust, predicted mean values are consistently improved with the model CH+PW+CN with respect to the model S+PW+KJ. Continuing the analysis of the predictions made with the model CH+PW+CN, mean values show remarkable agreement with respect to the values obtained from DNS. Most of the cases present differences lower than 20% of the rms of the total thrust. The estimate become less accurate for cases with $\theta_m = 20°$, although differences between the model and the DNS are lower than 50% of the signal. Interestingly, case C070 shows a difference of 17% of the rms of the total thrust. Furthermore, cases with low or high phase shift, A030 and B130, respectively, show errors larger than 20% of the total thrust.

Regarding the lift, cases B030, B050 and C030 present worse predictions of the mean lift by the model CH+PW+CN compared to the model S+PW+KJ, although the differences are small. Note that, even though the mean lift is better predicted by model S+PW+KJ for these cases, the L_2 norm of the difference between the model and the DNS obtained with model CH+PW+CN is approximatley one half of the value obtained with the model S+PW+KJ. For the rest of the cases the predictions obtained with the model CH+PW+CN are improved compared with the model S+PW+KJ. Continuing the analysis with model CH+PW+CN, mean lift is directly zero for the symmetric cases. The differences that appear in case A130 arise from the averaging process carried out because of the aperiodic nature of this case. For cases with mean pitch angle $\theta_m = 10°$ the results are very good. Cases with lower phase shift B030, B050 and B070 present differences in mean lift lower than 5% of the rms of total lift and cases B090, B110 and B130, lower than 20%. Again, when the mean pitch angle is increased to $\theta_m = 20°$, errors tend to increase. Case C070 presents an error in the mean lift of 10% of the rms of the total lift and cases C030, C090, C110 and C130 of approximately 30%. Case C050 presents a higher error.

In addition to the mean and L_2 norm values presented above, we show the evolution of the total thrust for all the cases in figure 5.10. It can be seen that the results obtained with the model CH+PW+CN are consistently improved compared to the model S+PW+KJ. Furthermore, for mean pitch values of $\theta_m = 0, 10°$ and phase shift $\varphi \geq 30°$ and $\varphi \leq 90°$, the model CH+PW+CN captures with high fidelity the values obtained from the DNS. For the highest phase shift values evaluated, $\varphi \geq 110°$, the model presents a small phase shift with respect to the DNS. Higher errors appear when the mean pitch angle is set to $\theta_m = 20°$, except when the phase shift is $\varphi = 70°$.

The evolution of the total lift (figure 5.11) also presents a consistent improvement of the estimation with model CH+PW+CN with respect to S+PW+KJ. Note that case B050 (figure 5.11e) presented a worse estimation of the mean lift with model CH+PW+CN compared to model S+PW+KJ but, as the L_2 norm predicted, its evo-

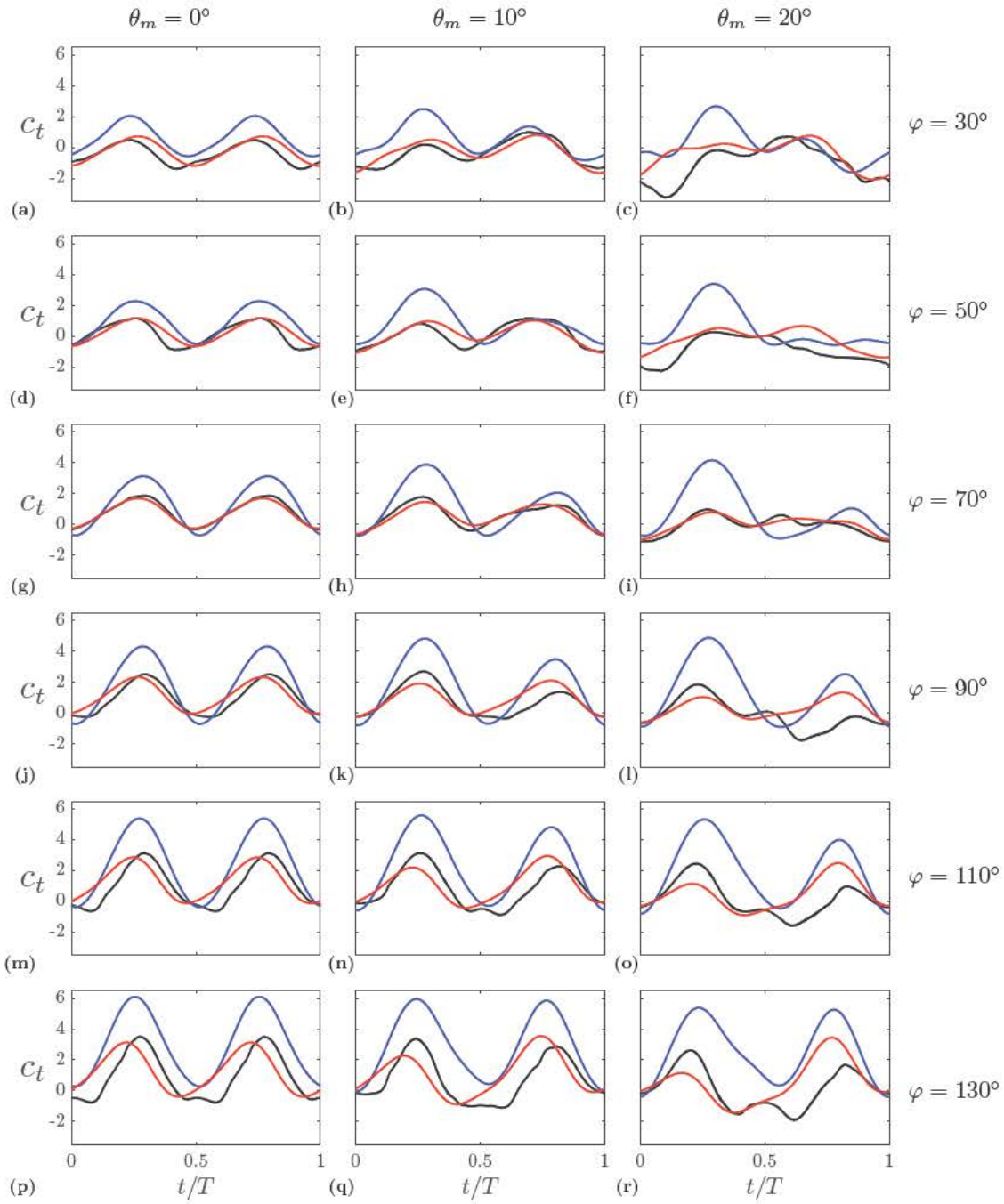

Figure 5.10: Total thrust obtained from the DNS (——) together with the estimations with model S+PW+KJ (——) and CH+PW+CN (——).

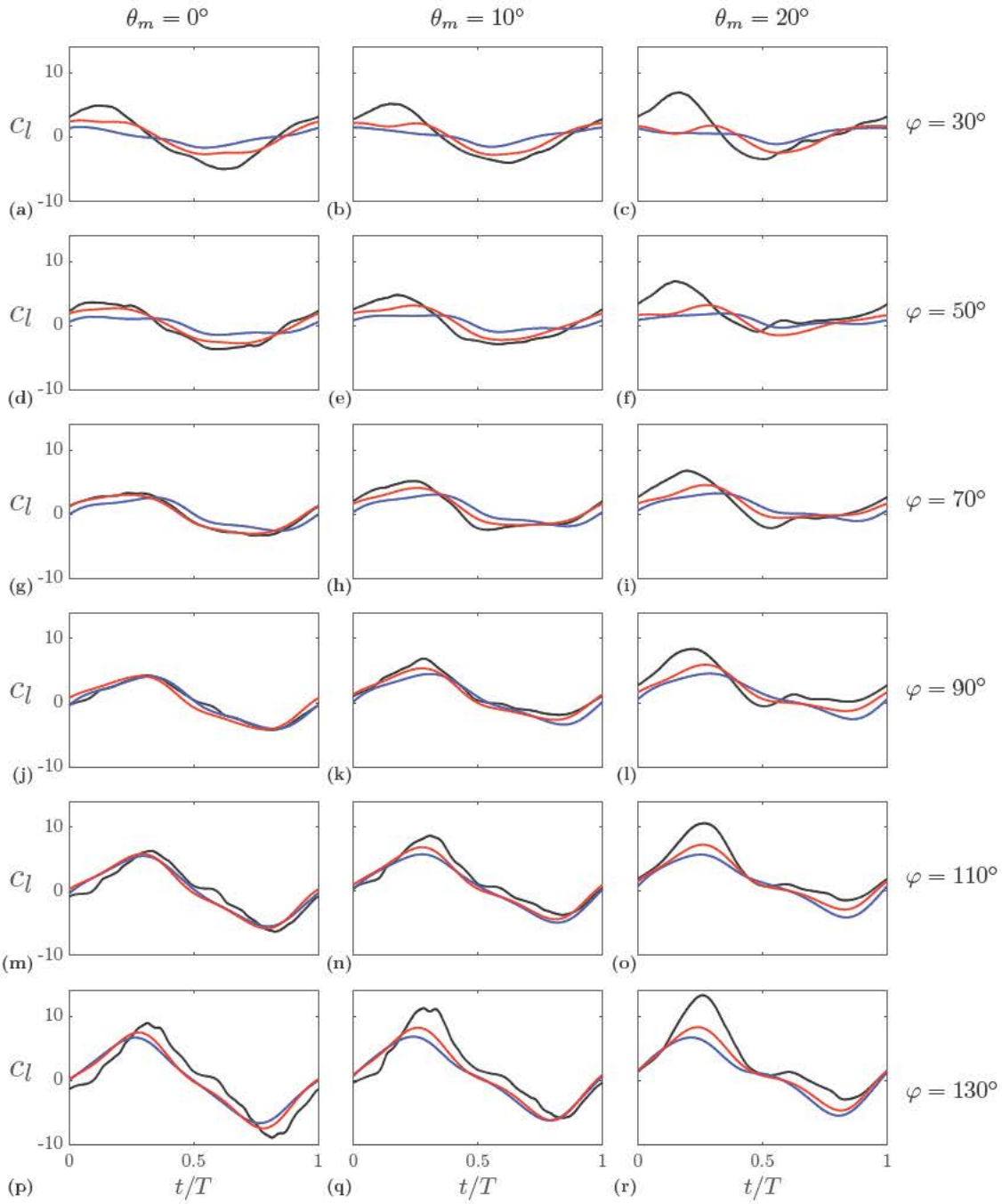

Figure 5.11: Total lift obtained from the DNS (——) together with the estimations with model S+PW+KJ (——) and CH+PW+CN (——).

lution is better captured by the former. The model CH+PW+CN presents very good estimations in cases with mean pitch value $\theta_m = 0, 10^\circ$ and phase shift $\varphi \geq 50^\circ$ and $\varphi \leq 110^\circ$. Again, a small phase shift appears for higher phase shift $\varphi = 130^\circ$, and a clear underestimation of the lift for the lower phase shift $\varphi = 30^\circ$. For mean pitch angle $\theta_m = 20^\circ$, the model is not able to predict the peak of lift that takes place during the downstroke. Note that in this case the circulation and, hence, the modulus of the force is not well captured by the model of Pesavento and Wang [2004] with fixed coefficients (see figure 5.12).

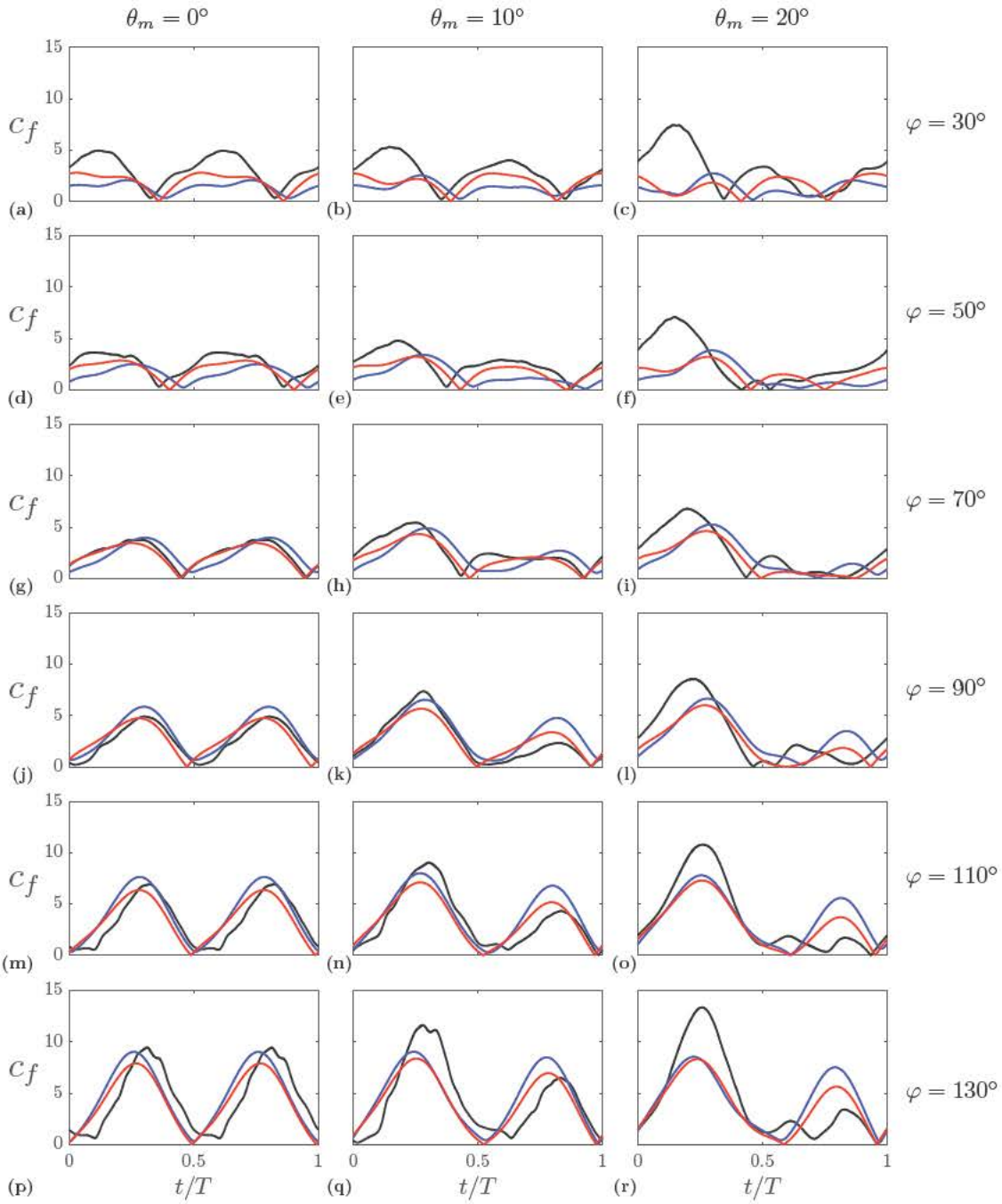

Figure 5.12: Modulus of force obtained from the DNS (——) together with the estimations with model S+PW+KJ (——) and CH+PW+CN (——).

CHAPTER
SIX

Onset of three dimensional wakes [1]

In the previous chapters we have analyzed by means of 2D DNS an actual 3D problem. In this chapter we study de stability of the wake of heaving and pitching airfoils subjected to 3D perturbations. We pretend to obtain a deeper knowledge on the onset of these instabilities and how they affect the aerodynamic performance of the airfoils. The 3D calculations presented in this chapter are performed with an infinite AR wing. Geometric 3D features introduced by finite wings are out of the scope of this work.

6.1 Methodology

We use Floquet stability analysis to study the stability of a 2D time-periodic base flow subjected to 3D perturbations. We follow the same approach as Barkley and Henderson [1996], Robichaux et al. [1999], Leontini et al. [2007] and others. The velocity and pressure fields (u_i, p) are decomposed into a time periodic 2D base flow (U_i, P) and a 3D perturbation (u_i', p'):

$$u_i(x,y,z,t) = U_i(x,z,t) + u_i'(x,y,z,t), \tag{6.1a}$$

$$p(x,y,z,t) = P(x,z,t) + p'(x,y,z,t). \tag{6.1b}$$

Under the assumption of small perturbations, the evolution equations of u_i' can be linearised. The governing equations for the perturbation (u_i', p') after linearisation are

$$\frac{\partial u_i'}{\partial x_i} = 0, \tag{6.2a}$$

$$\frac{\partial u_i'}{\partial t} + u_j'\frac{\partial U_i'}{\partial x_j} + U_j'\frac{\partial u_i'}{\partial x_j} = -\frac{1}{\rho}\frac{\partial p'}{\partial x_i} + \nu\frac{\partial^2 u_i'}{\partial x_i^2}. \tag{6.2b}$$

These equations are suplemented with boundary conditions for the perturbation velocities. At all boundaries we impose $u_i' = 0$, except at the outlet, where an advective

[1] The content of this chapter is published in
Moriche, M., Flores, O., and García-Villalba, M. Three-dimensional instabilities in the wake of a flapping wing at low Reynolds number. In *Int. J. Heat Fluid Flow*, 2016b

boundary condition is imposed as in other studies Barkley and Henderson [1996]. At the body surface we also impose $u_i' = 0$, since the base flow already fulfills the no slip condition at the body surface.

Since the problem is homogeneous in the spanwise direction, we can express the velocity and pressure fields as Fourier integrals

$$u_j'(x,y,z,t) = \int_{-\infty}^{\infty} \hat{u}_j(x,\beta,z,t) e^{i\beta y} d\beta, \tag{6.3a}$$

$$p'(x,y,z,t) = \int_{-\infty}^{\infty} \hat{p}(x,\beta,z,t) e^{i\beta y} d\beta, \tag{6.3b}$$

where $\hat{u}_j$ and $\hat{p}$ are the spanwise Fourier modes of the perturbation velocity and pressure, respectively. Introducing equation (6.3) into equation (6.2)) we obtain a 2D problem for each β. The advantage of this approach is the computational savings of solving a set of 2D problems instead of a 3D one.

Once the spanwise wavenumber is fixed, obtaining all the Floquet modes and their corresponding Floquet multipliers requires solving an eigenvalue problem. However, since we are only interested in obtaining the most unstable Floquet mode, it is sufficient to advance the solution of the perturbation during several periods, tracking the growth of the norm of the perturbation velocity. Then, the leading Floquet multiplier can be approximated by

$$\mu(\beta,t) = \frac{\|\hat{\mathbf{u}}(x,\beta,z,t+T)\|}{\|\hat{\mathbf{u}}(x,\beta,z,t)\|}, \tag{6.4}$$

where $\hat{\mathbf{u}}$ is the vector of spanwise Fourier mode of the perturbation velocity and $\|\cdot\|$ is the L_2 norm over spatial coordinates x and z. Appendix B shows the validation of the linear stability calculations of TUCAN and the capability of equation (6.4) to approximate the leading Floquet multiplier in this stability analysis.

6.2 Results

Four sets of mean pitch angle, θ_m, and phase shift, φ, have been analyzed by means of a 2D DNS and Floquet stability analysis. These cases have been selected from the database presented in chapter 4, which was developed to analyse the efficiency of heaving and pitching airfoils generating lift and thrust. The first two cases selected for this study (see table 6.1) are the cases with maximum propulsive efficiency at $\theta_m = 0°$ and $10°$ (cases A090 and B090, respectively). Cases C090 and B070 are selected to exemplify the effect of larger θ_m, and lagged pitching motion. Additionally, one case where the Floquet stability analysis predicts the onset of a 3D wake has been studied by means of 3D DNS.

Table 6.1: Motion parameters and integrated values of non-dimensional force coefficients of thrust and lift of the cases selected to analyze the 3D instabilities in the wake. The periodicity of the flow is indicated with P for periodic and D for periodic with period $2T$.

Case	θ_m	φ	Periodicity	$\overline{c_t}$	$\overline{c_l}$	η
A090	0	90	P	0.9957	0.0000	0.3644
B090	10	90	P	0.7245	1.5507	0.2620
B070	10	70	P	0.5718	0.8452	0.2467
C090	20	90	D	−0.1419	2.7850	-

6.2.1 2D wakes

We start by analyzing the wake of the 2D simulations. The configuration of the vortices in the wake can be observed in the flow visualizations of the spanwise vorticity shown in figure 6.1. Case A090 (shown in figure 6.1a) produces a reversed von Karman street, characteristic of thrust producing wakes. In this wake the upper (lower) row of vortices presents anticlockwise (clockwise) rotation, corresponding to LEVs generated in the upstroke (downstroke). Vorticity shed through the trailing edge forms less intense vortices in the central region of the street. Cases B090 and B070 (figures 6.1b and c, respectively) produce a non-symmetrical wake, in which the upper row of vortices is composed of (weak) vorticity generated at the lower surface of the airfoil during the upstroke, and shed into the wake at the end of the stroke. In the lower row of vortices, the strong LEV and TEV pairs generated during the downstroke form a dipole with net clockwise rotation, consistent with a predominance of the LEV. This dipole is advected downstream similar to the LEVs in A090. The asymmetry of the wake of cases B070 and B090 is also reflected in the aerodynamic performance of these cases, which generate both thrust and lift. However for case C090 (shown in figure 6.1d), we observe that the TEV intensity is closer to the LEV than in the other cases and a dipole with both TEV and LEV is formed. As a consequence, the dipole moves with a self-induced velocity through the wake following a path (indicated in the figure by solid lines) that depends on the relative intensity of each vortex. The dipoles shed at odd periods follow curved paths where the TEV rotates around the LEV (black path). Alternatively, dipoles shed at even periods follow straight paths inclined upwards (green path). Note also that in C090 there is almost no vorticity generated during the upstroke.

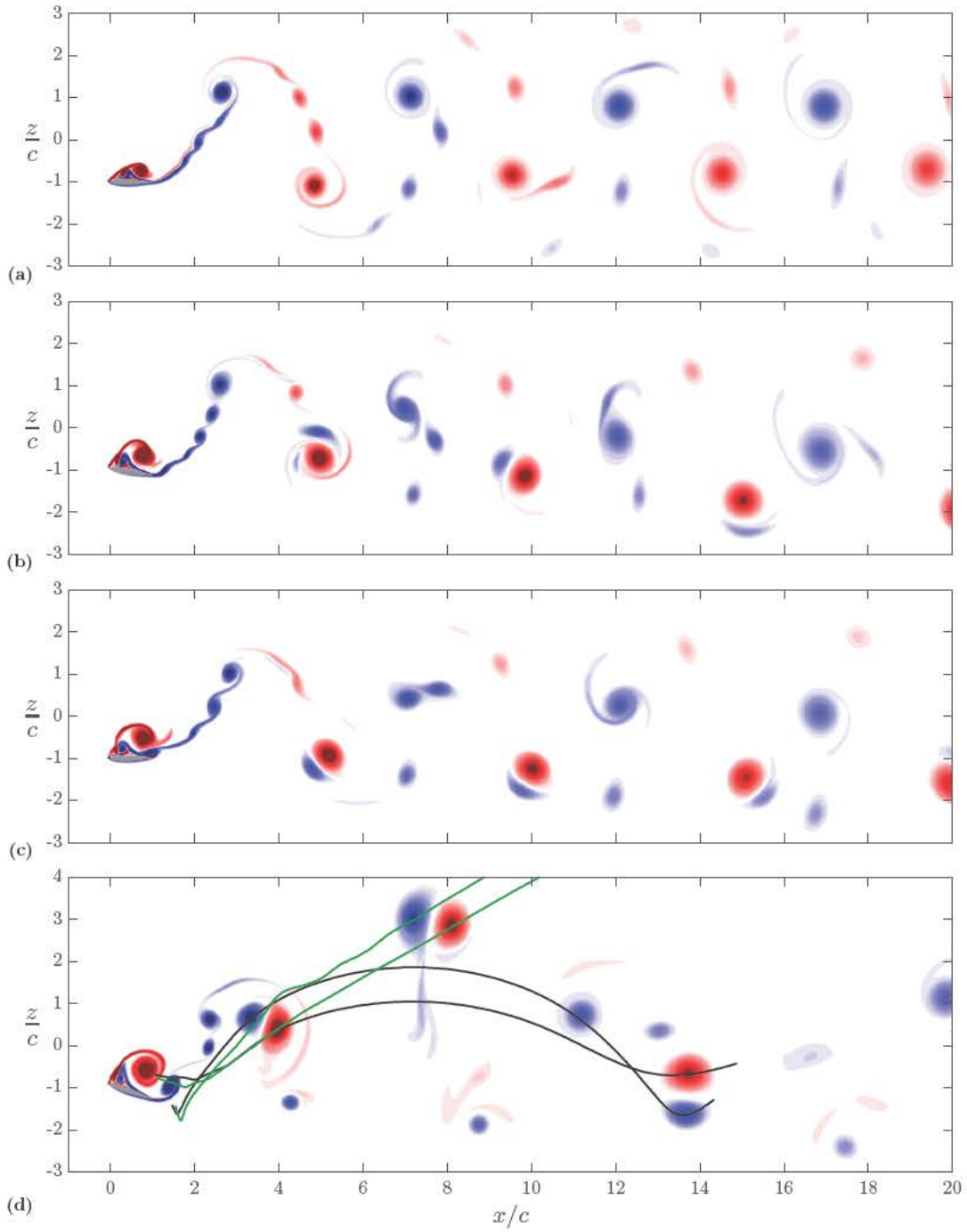

Figure 6.1: Flow visualization of spanwise vorticity at the end of the downstroke ($t/T = 0.5$) for the 2D cases. Blue corresponds to $\omega_y c/U_\infty = -15$ and red corresponds to $\omega_y c/U_\infty = 15$. a) Case A090, b) case B090, c) case B070 and d) case C090. Lines shown in *d*) correspond to the paths followed by LEV/TEV dipoles on alternate cycles: Odd periods (———) and even periods (———).

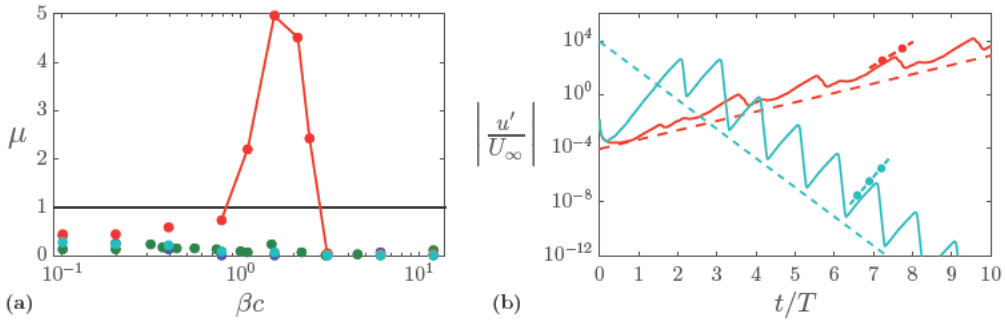

Figure 6.2: a) Floquet multiplier versus spanwise wavenumber and b) norm of the perturbation velocity time history for the most unstable spanwise wavenumber of case C090 ($\beta c = 1.54$) and the wavenumber with highest local growth rate of case B070 ($\beta c = 12$). Dashed line represents the overall growth given by the Floquet multiplier and dashed-dotted line the local growth of the vortices. (●) Case A090, (●) case B090, (●) case C090 and (●) case B070.

6.2.2 Stability analysis

In order to determine whether the complex wakes observed in the 2D DNS are prone to 3D instabilities, we have analyzed them using Floquet stability analysis. This analysis is performed following the methodology discussed in section 6.1, where the periodic base flows are obtained from the 2D simulations discussed in sections 6.2.1 and previously in 4.3. Recall that in case C090 the base flow period is $2T$ while in the other three cases the base flow period is T. In order to obtain converged Floquet multipliers, the linearised 2D problem associated to each spanwise wavenumber is run for at least $10T$. Note that, using the period of the base flow in the definition of the Floquet multiplier, equation (6.4), would lead to much larger μ in C090 than in the other cases, even if the growth of the perturbations in t were comparable. In order to avoid this, the period used in the definition of μ is equal to the period of the motion (T) for all cases.

Figure 6.2a shows the Floquet multiplier μ versus the spanwise wavenumber $\beta\, c$ for all cases. It can be seen that cases A090, B090 and B070 are linearly stable for all the $\beta\, c$ considered here. However, case C090 shows instability in a range of $0.94 \lesssim \beta\, c \lesssim 2.8$, which in terms of spanwise wavelengths becomes $6.7 \gtrsim \lambda/c \gtrsim 2.24$.

We now turn our attention to the evolution in time of the perturbations. Although not shown here, the analysis of the complete database shows that in some of the cases that are linearly stable, the energy of the perturbations grows locally at a high rate, even if it eventually decays for long times. This behaviour is observed for short wavelengths in cases B090, C090 and B070, particularly strong in case B070. In case A090 this local growth is not observed and the energy of the perturbations decays monotonically

for all spanwise wavelengths. In order to illustrate the difference between the unstable case, C090, and one of the cases with local growth, figure 6.2b displays the perturbation velocity norm as a function of time for the most unstable wavenumber of case C090 ($\beta\, c = 1.54$) and for the wavenumber with highest local growth rate of case B070 ($\beta\, c = 12$). For long times, the energy in case C090 increases while the energy in case B070 decreases, this is indicated in the figure by dashed lines whose slope corresponds to the Floquet multipliers. Furthermore, the time history of each case's perturbation shows periodic drops and high growth rates, specially in case B070. This local growth of the perturbation is associated with a convective instability and is represented with dashed-dotted lines in the figure. Flow visualization shown in figures 6.3b and d indicates that when the LEVs are shed periodically into the wake, the instability associated to them travels downstream and grows. Once these vortices leave the computational domain the norm of the perturbation drops. From this point of view, in case C090 the growth of the convective and absolute instabilities are comparable (see figures 6.3a and c), as also observed by Robichaux et al. [1999] for the flow over a square cylinder. However, in case B070 the convective instability is much stronger, presenting a local growth rate of $2.5 \cdot 10^3$ per motion period.

Given the range of wavelength of the instability of case C090, it is tempting to relate it to the instability mode A (long wavelength) observed in the wakes of cylinders Williamson [1996a], Barkley and Henderson [1996]. In order to evaluate the similarity, we consider a superposition of the base flow and the critical Floquet mode, where the intensity of the latter is selected arbitrarily for visualization purposes. Figure 6.4 shows a visualization of the reconstructed flow field at three time instants for a mode of case C090 with spanwise wavelength $\lambda/c = 3$, that corresponds to a Floquet multiplier of $\mu = 4.51$. For the visualization an iso-surface of the second invariant of the velocity gradient tensor, Q, is used. It can be observed that the instability consists of the bending of the TEV as it rotates around the LEV, which is consistent with mode A observed in flow over cylinders Williamson [1996a]. Note that there is little three-dimensionality in the vicinity of the airfoil. Figure 6.5 shows the corresponding visualization for the high frequency analysis ($\beta\, c = 12$) of case B070. In this case, the convective instability consists of pairs of streamwise vortices that wrap the LEVs. As it was mentioned before, similar convective instabilities are found in cases B090 and C090, but with considerably smaller growth rates.

6.2.3 3D case

The character of the instability observed in the wake of case C090 rise the question of to what extent the flow and the aerodynamic forces on the airfoil are affected by the 3D instabilities of the wake. In order to evaluate this effect, a 3D DNS of case C090

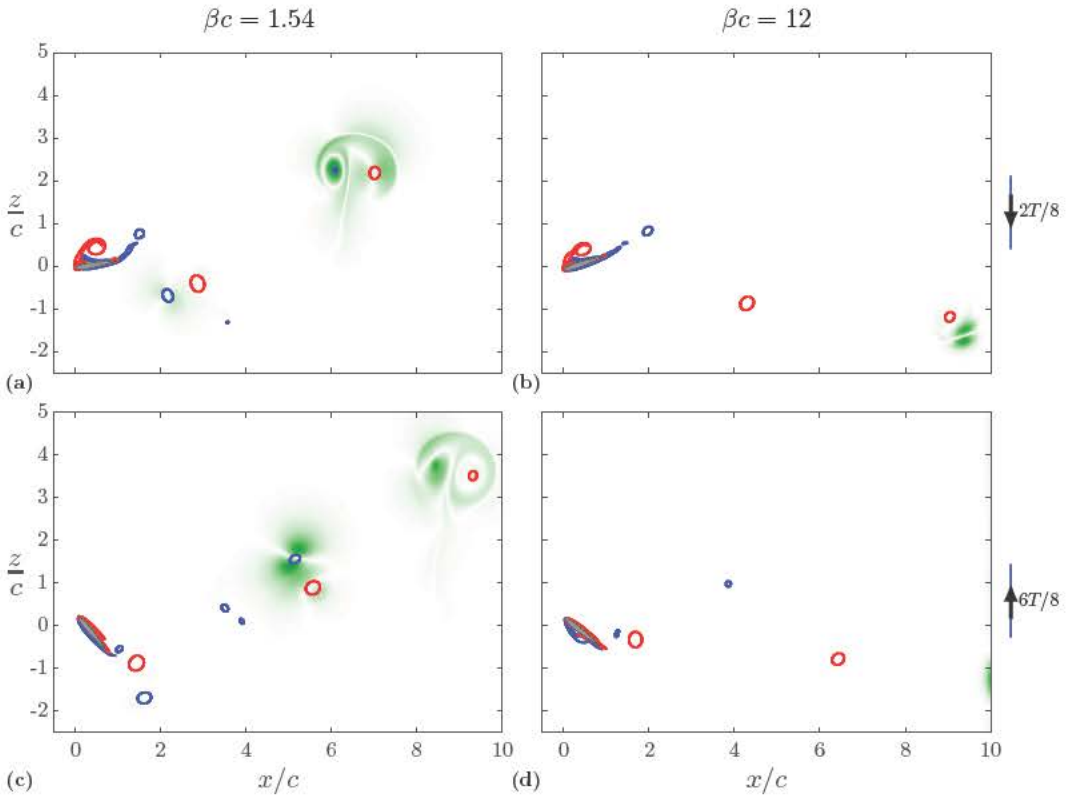

Figure 6.3: Line contours of spanwise vorticity $\omega_y c/U_\infty = -15$ (———) and $\omega_y c/U_\infty = 15$ (———) of case C090 for two spanwise wavenumbers at the middle of the downstroke and upstroke. Also, filled green contours of the absolute value of the spanwise perturbation velocity $|u_y'|$ are represented.

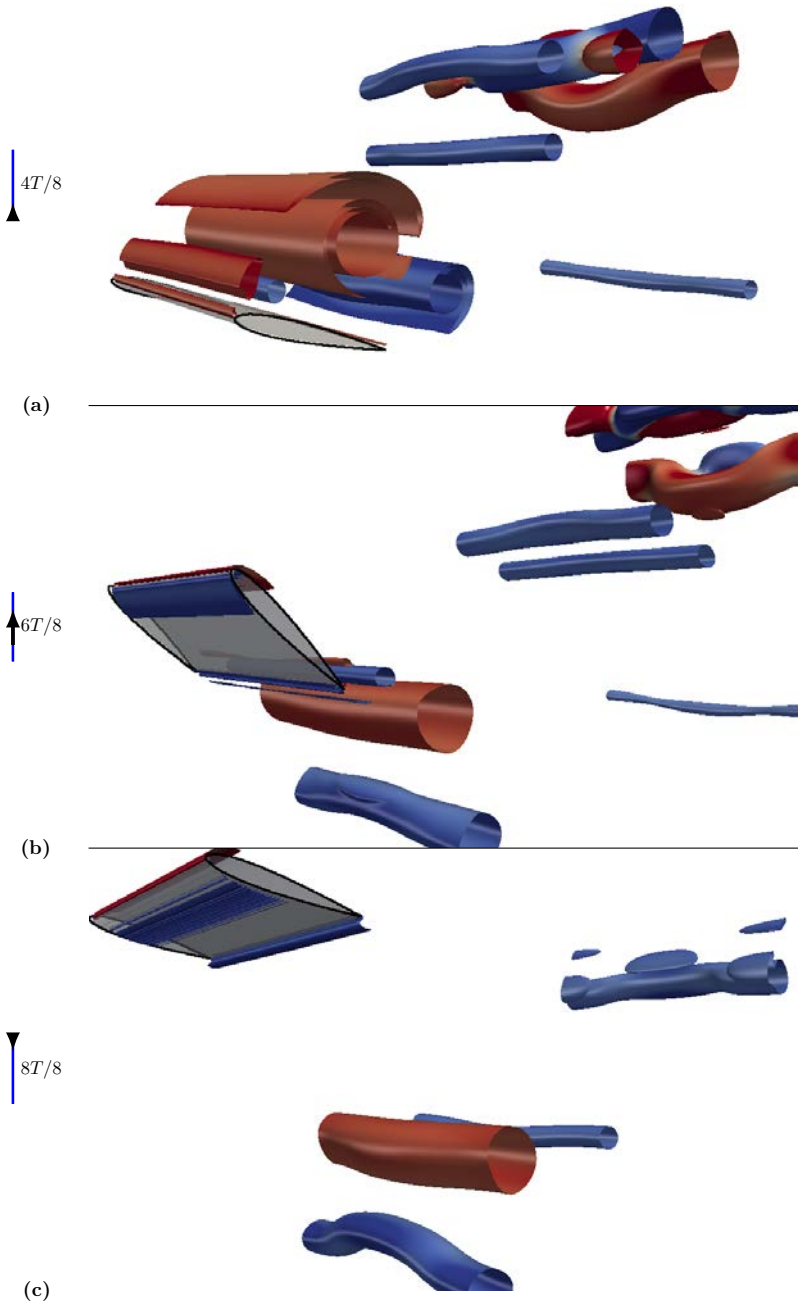

Figure 6.4: Isosurfaces of Q for the Floquet mode with $\lambda/c = 3$ of case C090. The surface is colored with the spanwise vorticity, ranging from $\omega_y c/U_\infty = -15$ (blue) to $\omega_y c/U_\infty = 15$ (red). The spanwise size of the visualization is equal to the wavelength of the mode. *a*) End of downstroke $t/T = 0.5$, *b*) middle of upstroke $t/T = 0.75$ and *c*) end of upstroke $t/T = 1$.

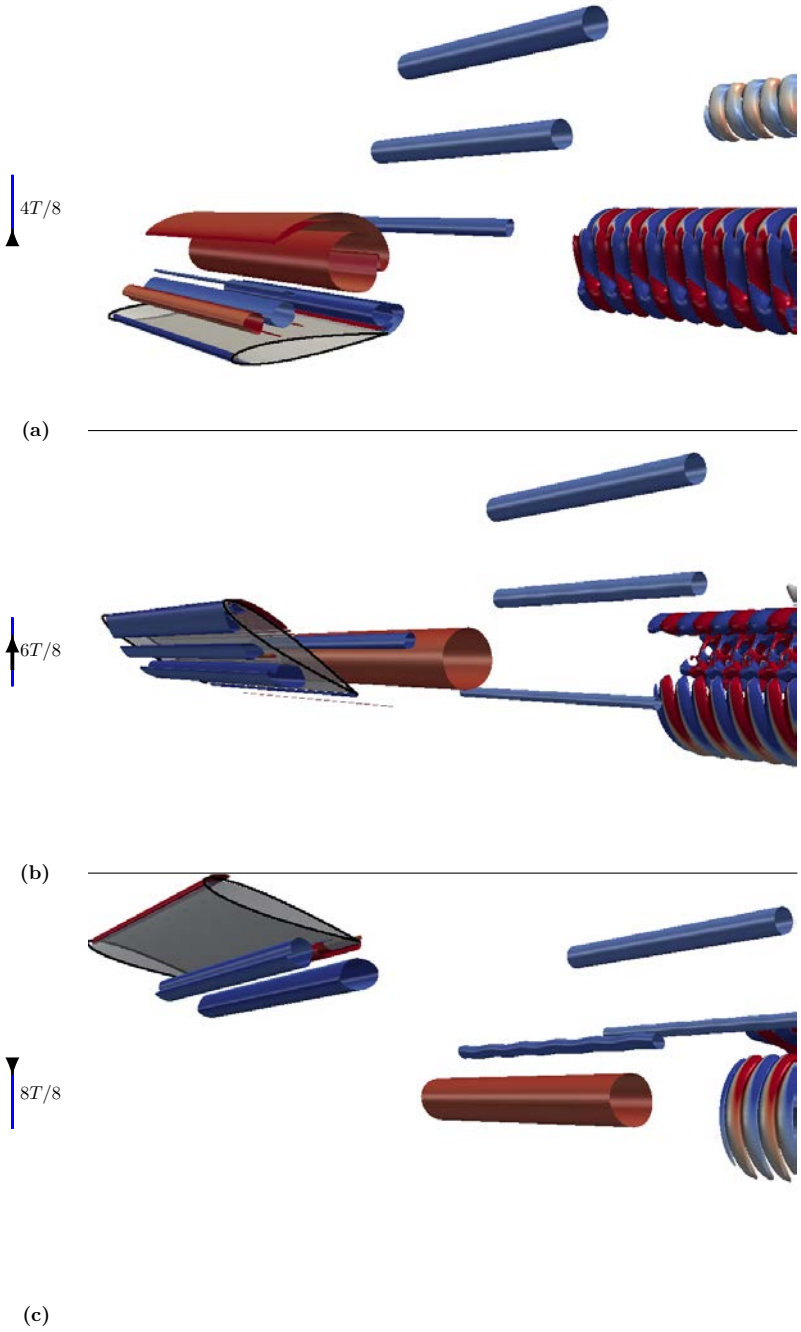

Figure 6.5: Isosurfaces of Q for the Floquet mode with $\lambda/c = 0.52$ of case B070. The surface is colored with the spanwise vorticity, ranging from $\omega_y c/U_\infty = -15$ (blue) to $\omega_y c/U_\infty = 15$ (red). The spanwise size of the visualization is six times the wavelength of the mode. *a*) End of downstroke $t/T = 0.5$, *b*) middle of upstroke $t/T = 0.75$ and *c*) end of upstroke $t/T = 1$.

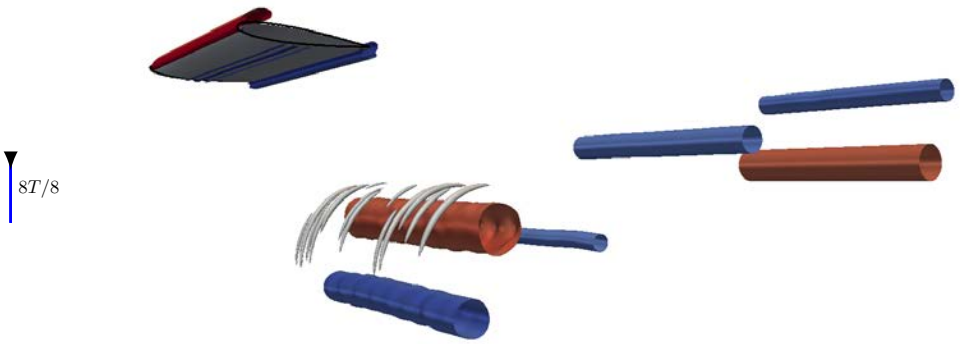

Figure 6.6: Isosurfaces of Q or case C090D3 at $t/T = 0.3215$ (second motion period). The surface is colored with the spanwise vorticity, ranging from $\omega_y c/U_\infty = -15$ (blue) to $\omega_y c/U_\infty = 15$ (red).

is performed, denoted case C090D3 in the following. As discussed in section 6.1, the computational domain is $12c$ in the streamwise direction and $8c$ in the vertical direction. The spanwise size of the computational domain is $3c$, corresponding to the wavelength of the mode visualized in figure 6.4.

Case C090D3 was initialised with the base flow of C090, adding random 3D perturbations localised around the airfoil. These random perturbations were projected into a solenoidal velocity field, and their intensity adjusted so that the maximum amplitude of the perturbation velocity is approximately $0.1U_\infty$. This perturbation is relatively large in order to ensure that the instability is quickly triggered, saving computational time. Note, however, that a perturbation of $0.1U_\infty$ in velocity represents just a perturbation of 1% in energy. A total of 15 periods have been run to reach a quasi-periodic flow from a statistical point of view.

Figure 6.6 shows isosurfaces of the second invariant of the velocity gradient tensor, Q, for a time instant corresponding to the beginning of the simulation. It can be observed how a convective instability is triggered by the initial noise, with similar wavelength and shape as the one showed in figure 6.5. After these vortices leave the computational domain, the instability associated with the bending of the TEV develops, repeating periodically in each oscillation cycle. This final state is shown in figure 6.7, where it can be seen that right after being shed, the LEV and TEV are essentially 2D vortices, figure 6.7a. However, as they are advected away from the airfoil the TEV bends as it rotates around the LEV, figure 6.7b. By the end of the upstroke, figure 6.7c, the LEV

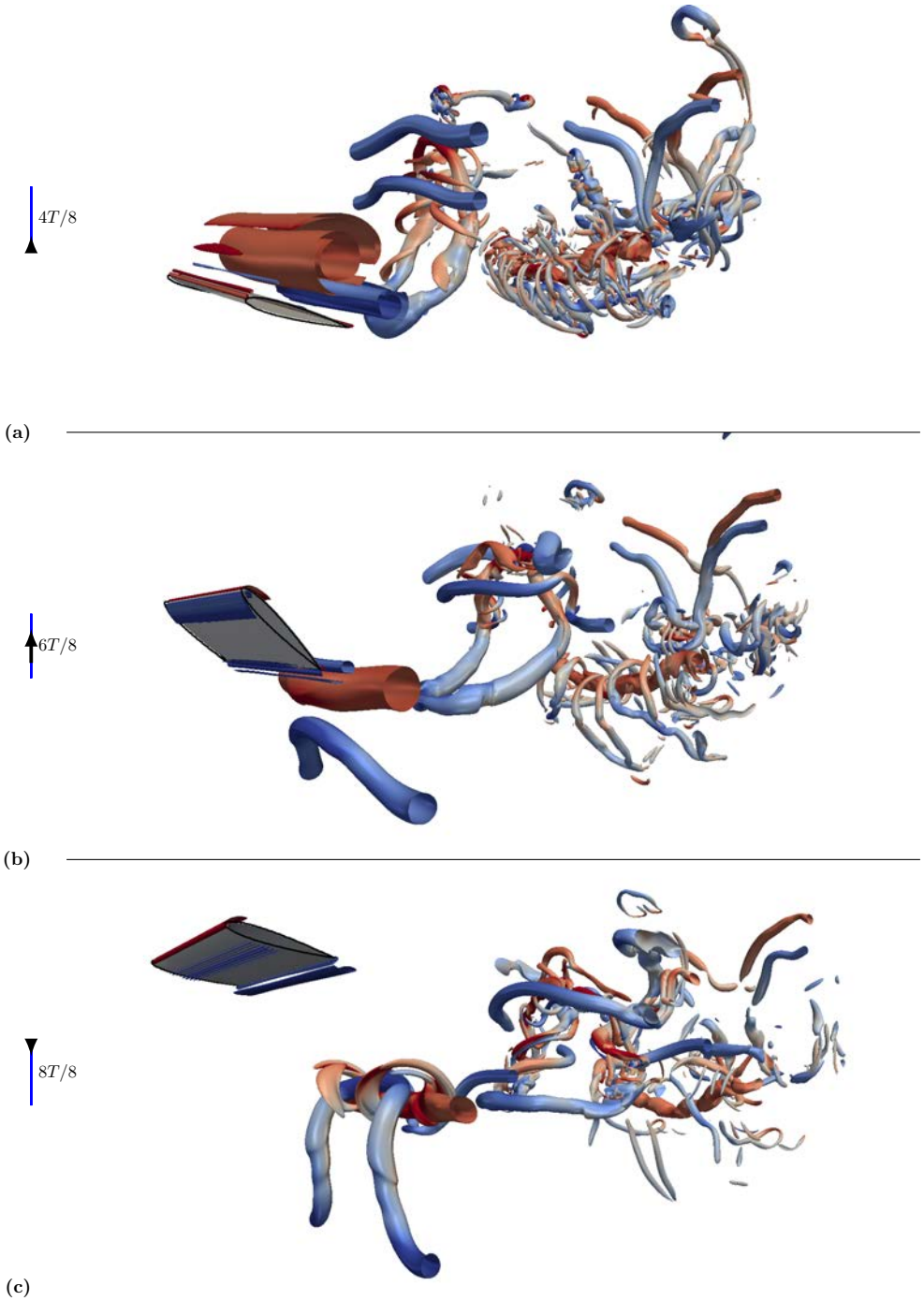

Figure 6.7: Isosurfaces of Q for case C090D3. The surface is colored with the spanwise vorticity, ranging from $\omega_y c/U_\infty = -15$ (blue) to $\omega_y c/U_\infty = 15$ (red). *a*) End of downstroke $t/T = 0.5$, *b*) middle of upstroke $t/T = 0.75$ and *c*) end of upstroke $t/T = 1$.

Table 6.2: Mean and rms force coefficients for cases C090 and C090D3.

Case	$\overline{C_x}$	$\overline{C_z}$	${C_x}^{\mathrm{rms}}$	${C_z}^{\mathrm{rms}}$
C090	0.1419	2.7850	0.9550	2.9417
C090D3	−0.0258	2.3494	0.8794	2.8090

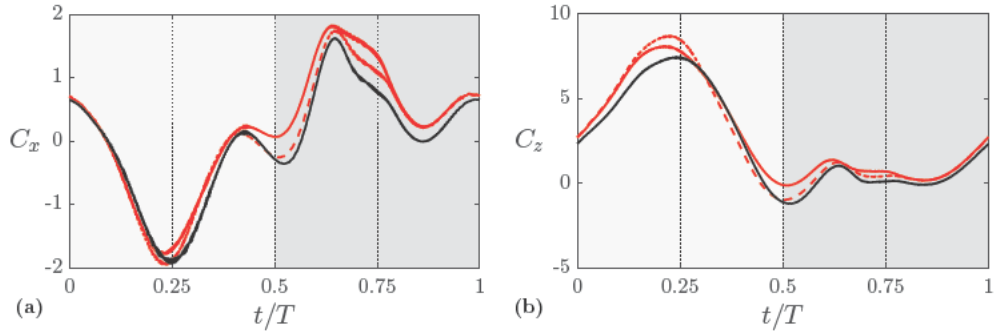

Figure 6.8: Comparison of the non-dimensional force coefficients between cases C090 and C090D3. a) C_x, b) C_z. Odd periods of C090 (——), even periods of C090 (- - -) and the averaging of the last five motion periods of case C090D3 (——) are represented. Ligher gray regions represent the downstroke and darker gray the upstroke.

has started engulfing the TEV, which eventually results in the complex vortex fields observed further downstream. This evolution is consistent with the Floquet modes shown in figure 6.4, where only the linear (small amplitude) part of the evolution can be observed (i.e. bending of the TEV).

The influence that the presence of 3D structures in the wake has on the aerodynamic forces on the airfoil is analysed in figure 6.8 and table 6.2, which show the evolution of the non-dimensional coefficients of the aerodynamic forces of cases C090 and C090D3 and their time averaged and rms values, respectively. The non-dimensional coefficients of the aerodynamic forces are defined as

$$C_x = \frac{2\,D}{\rho {U_\infty}^2\, b\, c}, \tag{6.5a}$$

$$C_z = \frac{2\,L}{\rho {U_\infty}^2\, b\, c}, \tag{6.5b}$$

where D and L are the total drag and lift, respectively, and b the span of the wing. The results for C090D3 are phase-averaged values over the last five periods of the simulation. For C090 the difference between odd and even periods is represented with solid and dashed lines. It can be observed that, despite the strong 3D character of the wake just

a few chords downstream of the airfoil, the aerodynamic forces of C090 and C090D3 are very similar. The variation in the rms of the force coefficients is small, less than 5%. Concerning the mean values, case C090D3 shows a decrease of 15% in the mean lift with respect to C090, and a change in the sign of the horizontal force, so instead of being a drag producing case, C090D3 generates a small amount of thrust. Since the horizontal force is much smaller than the vertical force, this change can be understood as a 15% change in magnitude of the total force and a small tilting upstream of the force vector of approximately 2°. The differences on the streamwise force are more pronounced in the upstroke ($0.5 < t/T < 1.0$) while differences in the vertical force are more noticeable in the downstroke ($0 < t/T < 0.5$).

Figure 6.9 shows contours of the spanwise vorticity of cases C090 and C090D3. Filled contours in red represent case C090 and line contours represent C090D3 (The color indicating the spanwise position). At the end of the downstroke figure (6.9a) the LEV of case C090D3 is 2D and its size and position very similar to the LEV of case C090 while the TEV has started to bend. Once the LEV and TEV are shed and advected into the wake the differences between case C090 and C090D3 are more obvious: the TEV of case C090D3 bends figure (6.9b) and the LEV and the TEV finally merge figure (6.9c). During the downstroke figure (6.9d) the flow of case C090D3 near the airfoil is again 2D as it is shown by the collapse of line contours for different spanwise positions. Overall, 3D instabilities are produced after detachment and, relatively far from the airfoil, so the similarities in the aerodynamic forces are consistent with the fact that the 3D flow near the airfoil resembles that of the 2D case.

In summary, we have observed small variations in the force coefficients comparing the 2D and 3D cases. Furthermore, previous results on finite aspect-ratio wings, e.g. Taira and Colonius [2009], have shown that interactions between wing tip vortices with leading-edge and trailing-edge vortices have a significant influence on the aerodynamic forces. Therefore, it might be concluded that finite aspects-ratio effects are more important than the 3D instability of the 2D flow on the modification of the aerodynamic forces on 3D wings with respect to 2D airfoils.

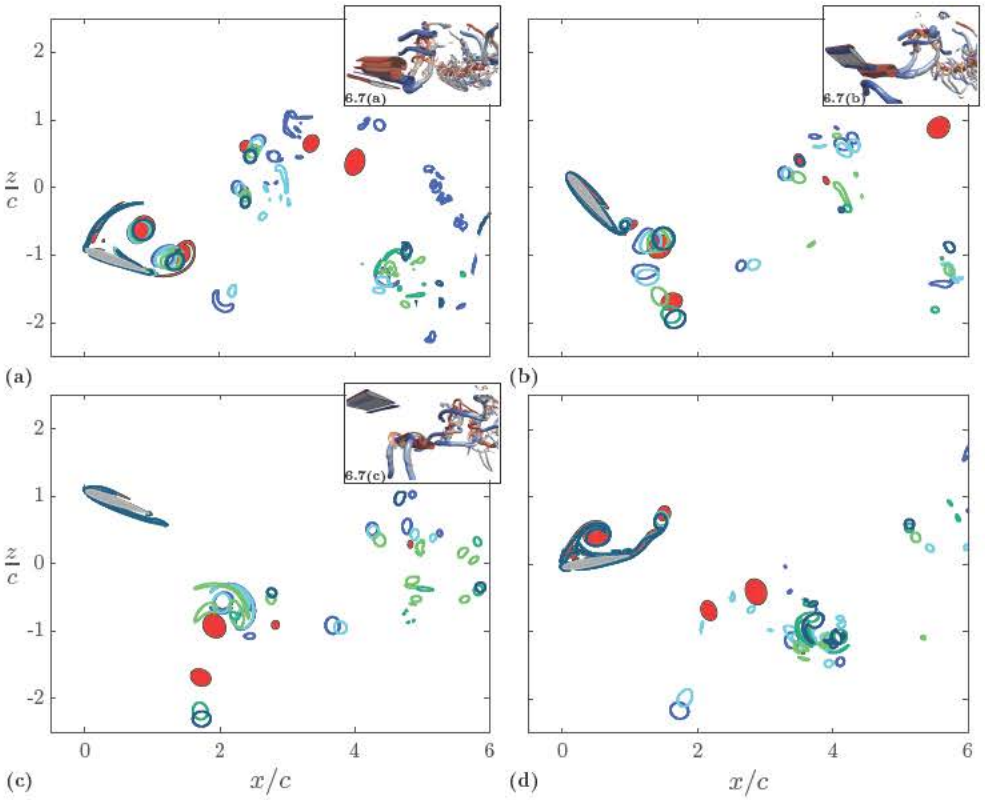

Figure 6.9: Contours of spanwise vorticity $\omega_y c/U_\infty = \pm 15$ for cases C090 and C090D3. Case C090 is represented with filled contours in red and case C090D3 with line contours coloured from green to blue indicating the spanwise position of the xz plane represented. Five equally spaced y/c coordinates have been selected in half of the spanwise domain ($1.5c$). a) End of downstroke $t/T = 0.5$, b) middle of upstroke $t/T = 0.75$, c) end of upstroke $t/T = 1$ and d) middle downstroke $t/T = 0.25$. Upper left corner of a, b and c is filled with thumbnails of figures 6.7 a, b and c for reference.

CHAPTER
SEVEN

Summary, conclusions and future work

The aim of the present work was to obtain a deeper insight in the unsteady aerodynamics of flapping wings. This chapter brings together the main areas covered in this thesis as well as final comments on the main findings provided through the document. Also, some recommendations for future work are outlined.

7.1 Summary

The first part of this thesis consisted in the development of TUCAN, an in-house code to perform DNS of incompressible flow around moving bodies with arbitrary shape. TUCAN is a parallel code written in Fortran 90 that uses an IBM to model the presence of bodies in the flow. TUCAN has been validated against numerous tests, so its capability to represent physics has been demonstrated. Furthermore, TUCAN has been successfully used in three external computing centers belonging to the TOP500 list [TOP500, 2016] published in June 2016. A parallel efficiency higher than 80% was achieved up to 8192 processors.

After the implementation and validation of TUCAN, we performed 2D DNS of heaving and pitching airfoils in order to obtain insight into the unsteady aerodynamics of flapping flight. Although the problem was simplified (for example, by imposing sinusoidal motion laws or fixing the Re) the parameter space to cover was still huge. Consequently, we only varied two motion parameters: the mean pitch angle θ_m and the phase shift φ between the heaving and pitching motions, resulting in a database of 18 cases. The averaged and instantaneous values of the aerodynamic forces of these cases were analyzed, and the main features of the flow were studied by visualization techniques. The long term goal of the project in which this work is enclosed is to be able to obtain accurate predictions of the forces produced in flapping flight, so we evaluated the capability of reduced order models to estimate these forces. For that, we decided that the best approach to use was to decompose the total aerodynamic force in different contributions and analyze them separately. The algorithm used in this work separates the total aerodynamic force in contributions from body motion, vorticity within the flow and surface vorticity. This algorithm was selected based on specific features that make

it very attractive for the current work needs.

The previous findings enhance our understanding of the generation of aerodynamic forces by flapping airfoils, but actual flapping flight takes place in the 3D world. Therefore, the final part of this work is dedicated to the analysis of the 3D character of the flow around infinite AR wings. We focused on two aspects. First, we analyzed the stability of the 2D flow subjected to 3D perturbations on four cases from the database. Second, we studied the effect that the 3D character of the flow has on the aerodynamic forces for one linearly unstable case. For the first analysis we used Floquet theory and for the second we performed 3D DNS. Finally, the main features of the fully developed 3D wake were commented.

7.2 Conclusions

We start drawing conclusions from the aerodynamic forces generated by the 2D cases. Concerning the two motion parameters modified in this work, the mean pitch angle has a clear effect on the aerodynamic forces whereas the phase shift influence is less intuitive. For symmetric motions ($\theta_m = 0$) thrust is generated in both downstroke and upstroke and, therefore, these cases present maximum thrust and propulsive efficiency compared to cases with non-zero θ_m (except for cases with $\varphi = 30°$). If the mean pitch angle is increased, positive lift is produced at the cost of reducing the thrust. A moderate value of $\theta_m = 10°$ result in airfoils that generate thrust and lift while higher values ($\theta_m = 20°$) result in a degeneration of the thrust but very large lift. In fact, some cases with $\theta_m = 20°$ do generate drag. Modifying the phase shift affects the flow around the airfoil and this is translated in different performance in terms of forces. For the parameters studied in this work, a phase shift of $\varphi = 90°$ gives the highest propulsive efficiency. If the phase shift is increased to $\varphi = 110°$, higher forces are produced, but the propulsive efficiency is slightly deteriorated. Reducing the phase shift to $\varphi = 70°$ is detrimental for both the forces and the propulsive efficiency.

Regarding the analysis of the different contributions to the total aerodynamic force, it is clear that the most important part of the force is the contribution of vorticity within the flow, followed by the contribution of body motion. The contribution of surface vorticity to the total aerodynamic force is approximately one order of magnitude smaller than the aforementioned contributions. The most valuable finding from this analysis is that the force produced by the vorticity within the flow tends to be perpendicular to the chord. This observation is in agreement with the empirical model of Dickinson et al. [1999].

The next topic covered in this work was the modelling of the aerodynamic forces. The advantage of having decomposed the aerodynamic force in three different contributions is that modelling each of them separately is simpler than modelling its total value. The

total force was then obtained as the sum of the contribution from the body motion and the estimation of the contribution from vorticity within the flow, neglecting the effect of surface vorticity. One of the advantages of the decomposition algorithm used in this work is that the contribution of body motion can be calculated without integrating Navier-Stokes equations, so needs not to be modelled. Conversely, the contribution from vorticity within the flow is estimated with a small modification of available models from the literature. The modulus of the force is given by the quasi-steady model for the circulation of Pesavento and Wang [2004] and the direction of the force is set normal to the chord, based on the observations made in this work. The predicted forces with the procedure described in this work show remarkable results in the case of the thrust. In the case of lift, the predicted values are less accurate, but there is a clear improvement compared to the widely used Kutta-Joukowsky theorem to predict the direction of the force.

Finally, we highlight the main findings from studying the 3D character of the flow of four of the cases from the database. Among these cases, there is one that is linearly unstable for a specific range of spanwise wavenumbers, so the flow will eventually become 3D. Interestingly, one of the cases which is linearly stable for the frequencies studied here, presents a strong convective instability. Therefore, the flow in this case will remain 2D, but any perturbation will convect downstream with a high growth rate. The linearly unstable case was studied also by 3D DNS to analyze the influence of fully developed 3D structures on the aerodynamic forces. Results indicate that, since the flow is almost 2D in the vicinity of the airfoil, so are the forces. This result is in agreement with the flow visualization analysis of the force density, which indicates that flow structures generate negligible force when they are not close to the airfoil.

7.3 Future work

The versatility of the code developed in this thesis, TUCAN, opens up many possibilities for future projects inside the research group. For example, some work to study the flow inside the human heart where the computations are performed with TUCAN, is currently being done in the group. Furthermore, different industries like the automotive or the aerospace can benefit from the current capabilities of TUCAN. Regarding its implementation, it would be interesting if future projects using TUCAN include some work load to improve it, either by optimizing the performance of the code or by adding new features to it. A natural progression would be the use of non-uniform grids. This would allow the use of less grid points far from the body (where the required resolution is lower) while keeping the same resolution in the body. The first advantage of this would be the reduced memory usage at execution time and the smaller size of the output files. Unfortunately, this will affect the solvers used for the linear systems and,

therefore, work needs to be done in order to find an efficient implementation in terms of computing time. Another improvement would be to overcome the requirement of the current IBM algorithm to use uniform grids within the scope of the delta function.

Regarding the motion of rigid bodies, although it is not mentioned in this document, TUCAN is capable of advancing the equations of motion for a rigid body. This feature of the code allows the study of different problems, namely free falling objects, an insect flying free on a uniform stream or the sedimentation of multiple bodies with arbitrary shape. Additionally, a fruitful area for future work would be the inclusion of control theory in the motion of the aerodynamic surfaces or body parts of aerial vehicles. The main difficulty to overcome in this area of knowledge is that the time scale of the flapping motion is of the same order of the system response time to the equations of motion.

More related to the physics studied in this work, it would be interesting to see how the observations made in this work are affected by changes in the reduced frequency and/or non-dimensional amplitude of the motion. Also, a more extensive evaluation of the fitting parameters used in the quasi-steady model for the circulation would provide useful data for engineering applications.

Finally, we restricted the stability analysis presented in this document to periodic flows in order to take advantage of Floquet theory. However, the linear stability tool developed here in combination with TUCAN is a suitable tool to analyze the stability of different and much more complex flows. Flows that can be studied with this tool need not to fulfill the requirements needed to apply Floquet theory.

Bibliography

Andersen, A., Pesavento, U., and Wang, Z. J. Unsteady aerodynamics of fluttering and tumbling plates. *J. Fluid Mech.*, 541:65–90, 2005.

Anderson, J.M., Streitlien, K., Barret, K. S., and Triantafyllou, M. S. Oscillating foils of high propulsive efficiency. *J. Fluid Mech.*, 360:41–72, 1998.

Ansari, R., Zbikowski, R., and Knowles, K. Aerodynamic modelling of insect-like flapping flight for micro air vehicles. *Prog. Aerosp. Sci.*, 42:129–172, 2006.

Ashraf, M.A., Young, J., and Lai, J.C.S. Reynolds number, thickness and camber effects on flapping airfoil propulsion. *J. Fluids Struct.*, 27(2):145–160, 2011.

Baker, A. H., Falgout, R. D., Kolev, T. V., and Yang, U. M. Scaling hypre's multigrid solvers to 100,000 cores. In *High-Performance Scientific Computing*, pages 261–279. Springer, 2012.

Barkley, D. and Henderson, R. D. Three-dimensional Floquet stability analysis of the wake of a circular cylinder. *J. Fluid Mech.*, 322:215–241, 1996.

Betz, A. Ein beitrag zur erklaerung des segelfluges. *Zeitschrift für Flugtechnik und Motorluftschiffahrt*, 3(21):269–272, 1912.

Brown, D. L., Cortez, R., and Minion, M. L. Accurate projection methods for the incompressible Navier–Stokes equations. *J. Comp. Phys.*, 168(2):464–499, 2001.

Carr, L. W. Progress in analysis and prediction of dynamic stall. *J Aircraft*, 25(1):6–17, 1988.

Chang, C.-C. Potential flow and forces for incompressible viscous flow. In *Proc. R. Soc. Lond. A*, volume 437, pages 517–525, 1992.

Choi, J., Colonius, T., and Williams, D. R. Surging and plunging oscillations of an airfoil at low Reynolds number. *J. Fluid Mech.*, 763:237–253, 2015.

Dagum, L. and Menon, R. Openmp: an industry standard api for shared-memory programming. *IEEE Comput. Sci. Eng.*, 5(1):46–55, 1998.

del Álamo, J. C. and Jiménez, J. Spectra of the very large anisotropic scales in turbulent channels. *Phys. Fluids*, 15(6):L41–L44, 2003.

Deng, J. and Caulfield, C. P. Three-dimensional transition after wake deflection behind a flapping foil. *Phys. Rev. E*, 91(4):043017, 2015.

Deng, J., Sun, L., and Shao, X. Dynamical features of the wake behind a pitching foil. *Phys. Rev. E*, 92(6):063013, 2015.

Dickinson, M. H., Lehmann, F.-O., and Sane, S. P. Wing rotation and the aerodynamic basis of insect flight. *Science*, 284(5422):1954–1960, 1999.

Dong, H., Mittal, R., and Najjar, F. M. Wake topology and hydrodynamic performance of low-aspect-ratio flapping foils. *J. Fluid Mech.*, 566:309–343, 2006.

Ellington, C. P., Van Den Berg, C., Willmott, A. P., and Thomas, A.L.R. Leading-edge vortices in insect flight. *Nature*, 384:626–630, 1996.

Fluid Dynamics Group. Turbulence Database, 2016. URL http://torroja.dmt.upm.es/channels/data/fields/re180/.

Forum, Message P. Mpi: A message-passing interface standard. Technical report, Knoxville, TN, USA, 1994.

Garrick, I.E. Propulsion of a flapping and oscillating airfoil. 1937.

Glauert, H. The force and moment on an oscillating aerofoil. In *Vorträge aus dem Gebiete der Aerodynamik und verwandter Gebiete*, pages 88–95. Springer, 1930.

Hernández-Hurtado, E., Moriche, M., Flores, O., and García-Villalba, M. The flow around a flapping-wing micro air vehicle in free flight. In *11th European Fluid Mechanics Conference, Sevilla, Spain*, 2016.

Hoarau, Y., Braza, M., Ventikos, Y., Faghani, D., and Tzabiras, G. Organized modes and the three-dimensional transition to turbulence in the incompressible flow around a NACA0012âĹń wing. *J. Fluid Mech.*, 496:63–72, 2003.

Hypre. High performance preconditioners, 2016 June. URL http://www.llnl.gov/CASC/hypre/.

Jones, K. D. and Platzer, M. F. Numerical computation of flapping-wing propulsion and power extraction. AIAA paper AIAA-97-0826, 1997.

Katzmayr, R. Effect of periodic changes of angle of attack on behavior of airfoils. 1922.

Kim, J., Moin, P., and Moser, R. Turbulence statistics in fully developed channel flow at low Reynolds number. *J. Fluid Mech.*, 177:133–166, 1987.

Knoller, R. *Die gesetze des luftwiderstandes*. Verlag des Österreichischer Flugtechnischen Vereines, 1909.

Lai, M.-C. and Peskin, C. S. An immersed boundary method with formal second-order accuracy and reduced numerical viscosity. *J. Comp. Phys.*, 160(2):705–719, 2000.

Leontini, J. S., Thompson, M. C., and Hourigan, K. Three-dimensional transition in the wake of a transversely oscillating cylinder. *J. Fluid Mech.*, 577:79–104, 2007.

Lewin, G. C. and Haj-Hariri, H. Modelling thrust generation of a two-dimensional heaving airfoil in a viscous flow. *J. Fluid Mech.*, 492:339–362, 2003.

Linnick, M. N. and Fasel, H. F. A high-order immersed interface method for simulating unsteady incompressible flows on irregular domains. *J. Comp. Phys.*, 204(1):157–192, 2005.

Liu, C., Zheng, X., and Sung, C.H. Preconditioned multigrid methods for unsteady incompressible flows. *Journal of Computational Physics*, 139(1):35 – 57, 1998. ISSN 0021-9991. doi: 10.1006/jcph.1997.5859.

Lu, X.-Y. and Dalton, C. Calculation of the timing of vortex formation from an oscillating cylinder. *J. Fluids Struct.*, 10(5):527–541, 1996.

Lua, K. B., Lim, T. T., Yeo, K. S., and Oo, G. Y. Wake-structure formation of a heaving two-dimensional elliptic airfoil. *AIAA J.*, 45:1571–1583, 2007.

Martín-Alcántara, A., Fernandez-Feria, R., and Sanmiguel-Rojas, E. Vortex flow structures and interactions for the optimum thrust efficiency of a heaving airfoil at different mean angles of attack. *Phys. Fluids*, 27(7):073602, 2015.

Mittal, R. and Iaccarino, G. Immersed boundary methods. *Annu. Rev. Fluid Mech.*, 37: 239–261, 2005.

Mittal, R., Dong, H., Bozkurttas, M., Najjar, F.M., Vargas, A., and Von Loebbecke, A. A versatile sharp interface immersed boundary method for incompressible flows with complex boundaries. *J. Comp. Phys.*, 227(10):4825–4852, 2008.

Moriche, M., Flores, O., and García-Villalba, M. Flapping airfoil simulations at very low Reynolds. In *10th European Fluid Mechanics Conference, Copenhagen, Denmark*, 2014.

Moriche, M., Flores, O., and García-Villalba, M. Generation of thrust and lift with airfoils in plunging and pitching motion. In *J. Phys.: Conf. Ser.*, volume 574, page 012163, 2015.

Moriche, M., Flores, O., and García-Villalba, M. Analysis of the aerodynamivc forces on having and pitching airfoils at low Reynolds number. In *11th European Fluid Mechanics Conference, Sevilla, Spain*, 2016a.

Moriche, M., Flores, O., and García-Villalba, M. Three-dimensional instabilities in the wake of a flapping wing at low Reynolds number. In *Int. J. Heat Fluid Flow*, 2016b.

Moriche, M., Flores, O., and García-Villalba, M. On the aerodynamic forces on heaving and pitching airfoils at low Reynolds number. In *J. Fluid Mech.*, 2017, Submitted.

Noca, F., Shiels, D., and Jeon, D. A comparison of methods for evaluating time-dependent fluid dynamic forces on bodies, using only velocity fields and their derivatives. *J. Fluids Struct.*, 13(5):551–578, 1999.

Pesavento, U. and Wang, Z.J. Falling paper: Navier-stokes solutions, model of fluid forces, and center of mass elevation. *Phys. Rev. Lett.*, 93(14):144501, 2004.

Peskin, C. S. The immersed boundary method. *Acta Numer.*, 11:479–517, 0 2002. ISSN 1474-0508. doi: 10.1017/S0962492902000077.

Platzer, M. F., Jones, K. D., Young, J., and Lai, J. C. S. Flapping-wing aerodynamics: Progress and challenges. *AIAA J.*, 46(9):2136–2149, 2008.

Rai, M.M. and Moin, P. Direct simulations of turbulent flow using finite-difference schemes. *J. Comp. Phys.*, 96(1):15–53, 1991.

Raiola, M., Ianiro, A., Discetti, S., Moriche, M., Flores, O., and García-Villalba, M. Flow over flapping airfoils: qualitative and quantitative comparison between experiments and simulations. In *11th European Fluid Mechanics Conference, Sevilla, Spain*, 2016.

Robichaux, J., Balachandar, S., and Vanka, S.P. Three-dimensional Floquet instability of the wake of square cylinder. *Phys. Fluids*, 11:560–578, 1999.

Roma, A. M., Peskin, C. S., and Berger, M. J. An adaptive version of the immersed boundary method. *J. Comp. Phys.*, 153(2):509–534, 1999.

Rozhdestvensky, K. V. and Ryzhov, V. A. Aerohydrodynamics of flapping-wing propulsors. *Prog. Aerospace Sci.*, 39:585–633, 2003.

Sedov, L. I., Chu, C.K., Cohen, H., Seckler, B., and Gillis, J. Two-dimensional problems in hydrodynamics and aerodynamics. *Phys. Today*, 18:62, 1965.

Shyy, W., Berg, M., and Ljungqvist, D. Flapping and flexible wings for biological and micro air vehicles. *Prog. Aerospace Sci.*, 35(5):455–505, 1999.

Shyy, W., Aono, H., K., Chimakurthi S., Trizila, P., Kang, C. K., Cesnik, C. E. S., and Liu, H. Recent progress in flapping wing aerodynamics and aeroelasticity. *Prog. Aerospace Sci.*, 46:284–327, 2010.

Shyy, W., Aono, H., Kang, C.-K., and Liu, H. *An introduction to flapping wing aerodynamics*. Cambridge Univ. Press, 2013.

Spalart, P. R., Moser, R. D., and Rogers, M. M. Spectral methods for the navier-stokes equations with one infinite and two periodic directions. *J. Comp. Phys.*, 96(2):297 – 324, 1991. ISSN 0021-9991. doi: 10.1016/0021-9991(91)90238-G.

Taha, H. E., Hajj, M. R., and Nayfeh, A. H. Flight dynamics and control of flapping-wing mavs: a review. *Nonlinear Dyn.*, 70(2):907–939, 2012.

Taha, H. E., Hajj, M. R., and Beran, P. S. State-space representation of the unsteady aerodynamics of flapping flight. *Aerosp. Sci. Technol.*, 34:1–11, 2014.

Taira, K. and Colonius, T. Three-dimensional flows around low-aspect-ratio flat-plate wings at low Reynolds numbers. *J. Fluid Mech.*, 623:187–207, 2009.

The HDF Group. Hierarchical Data Format, version 5, 1997-2016. http://www.hdfgroup.org/HDF5/.

TOP500. TOP500 Supercomputer Site, 2016. URL http://www.top500.org.

Uhlmann, M.˙ First experiments with the simulation of particulate flows. Technical Report No. 1020, CIEMAT, Madrid, Spain, 2003. ISSN 1135-9420.

Uhlmann, M. An immersed boundary method with direct forcing for the simulation of particulate flows. *J. Comp. Phys.*, 209(2):448–476, 2005.

Uhlmann, M.˙Direct numerical simulation of sediment transport in a horizontal channel. Technical Report No. 1088, CIEMAT, Madrid, Spain, 2006. ISSN 1135-9420.

Visbal, M., Yilmaz, T. O., and Rockwell, D. Three-dimensional vortex formation on a heaving low-aspect-ratio wing: Computations and experiments. *J. Fluids Struct.*, 38: 58–76, 2013.

Visbal, M. R. Numerical investigation of deep dynamic stall of a plunging airfoil. *AIAA J.*, 49(10):2152–2170, 2011.

von Ellenrieder, K. D., Parker, K., and Soria, J. Flow structures behind a heaving and pitching finite-span wing. *J. Fluid Mech.*, 490:129–138, 2003.

von Ellenrieder, K. D., Parker, K., and Soria, J. Fluid mechanics of flapping wings. *Exp. Thermal Fluid Sci.*, 32:1578–1589, 2008.

Wang, S., Zhang, X., He, G., and Liu, T. Evaluation of lift formulas applied to low-Reynolds-number unsteady flows. *AIAA J.*, 53(1):161–175, 2014.

Wang, Z. Vortex shedding and frequency selection in flapping flight. *J. Fluid Mech.*, 410:323–341, 2000.

Wang, Z. J. Dissecting insect flight. *Annu. Rev. Fluid Mech.*, 37:183–210, 2005.

Wei, Z. and Zheng, Z. C. Mechanisms of wake deflection angle change behind a heaving airfoil. *J. Fluids Struct.*, 48:1–13, 2014.

Weis-Fogh, T. Energetics of hovering flight in hummingbirds and in drosophila. *J. Exp. Biol.*, 56(1):79–104, 1972.

Widmann, A. and Tropea, C. Parameters influencing vortex growth and detachment on unsteady aerodynamic profiles. *J. Fluid Mech.*, 773:432–459, 2015.

Williamson, C. H. K. Three-dimensional wake transition. *J. Fluid Mech.*, 328:345–407, 1996a.

Williamson, C. H. K. Vortex dynamics in the cylinder wake. *Annu. Rev. Fluid Mech.*, 28:477–539, 1996b.

APPENDIX

A

Complementary data of 2D cases

This chapter contains complementary information of the 2D cases presented in chapters 4 and 5 that supports the relevant results shown in them.

A.1 Periodicity of 2D cases

In this section the periodicity of each of the 2D cases presented in chapter 4 is analyzed in detail. We evaluate the periodicity of each case by looking at the evolution of the work required to move the airfoil in the downstroke and in the upstroke. The work used in each stroke is obtained by integrating the power needed to move the airfoil

$$W_d(i) = -\int_{iT}^{(i+0.5)T} \left(F_z\dot{h} + M_{y,x_p}\dot{\theta}\right) \mathrm{d}t, \tag{A.1a}$$

$$W_u(i) = -\int_{(i+0.5)T}^{(i+1)T} \left(F_z\dot{h} + M_{y,x_p}\dot{\theta}\right) \mathrm{d}t, \tag{A.1b}$$

where i is the index of the motion period in which the work is calculated. Figure A.1 shows the evolution of the work per stroke required to move the airfoil for each of the 2D cases from the database. Most of the cases are periodic with a period equal to the motion period $TU_\infty/c = 4.44$. For the symmetric cases ($\theta_m = 0°$) only the case with $\varphi = 30°$ presents an aperiodic behavior. Note that for the rest of the cases with $\theta_m = 0°$ the work required to move the airfoil in the upstroke is the same as in the downstroke. If the mean pitch value is increased to $\theta_m = 10°$ all the cases become periodic. Interestingly, for $\theta_m = 20°$ the cases with $\varphi = 90°, 130°$ are periodic with a period of twice the motion period. The case with $\theta_m = 20°$ and $\varphi = 30°$ presents small differences between consecutive periods, whereas the case with $\varphi = 70°$ presents a strong aperiodic behavior.

Figure A.2 shows the evolution of thrust versus lift. It can be seen that the periodicity evaluated in terms of work needed per stroke is in agreement with the evolution of the forces. Periodic cases present an unique cycle of thrust versus lift, whereas aperiodic cases present multiple cycles.

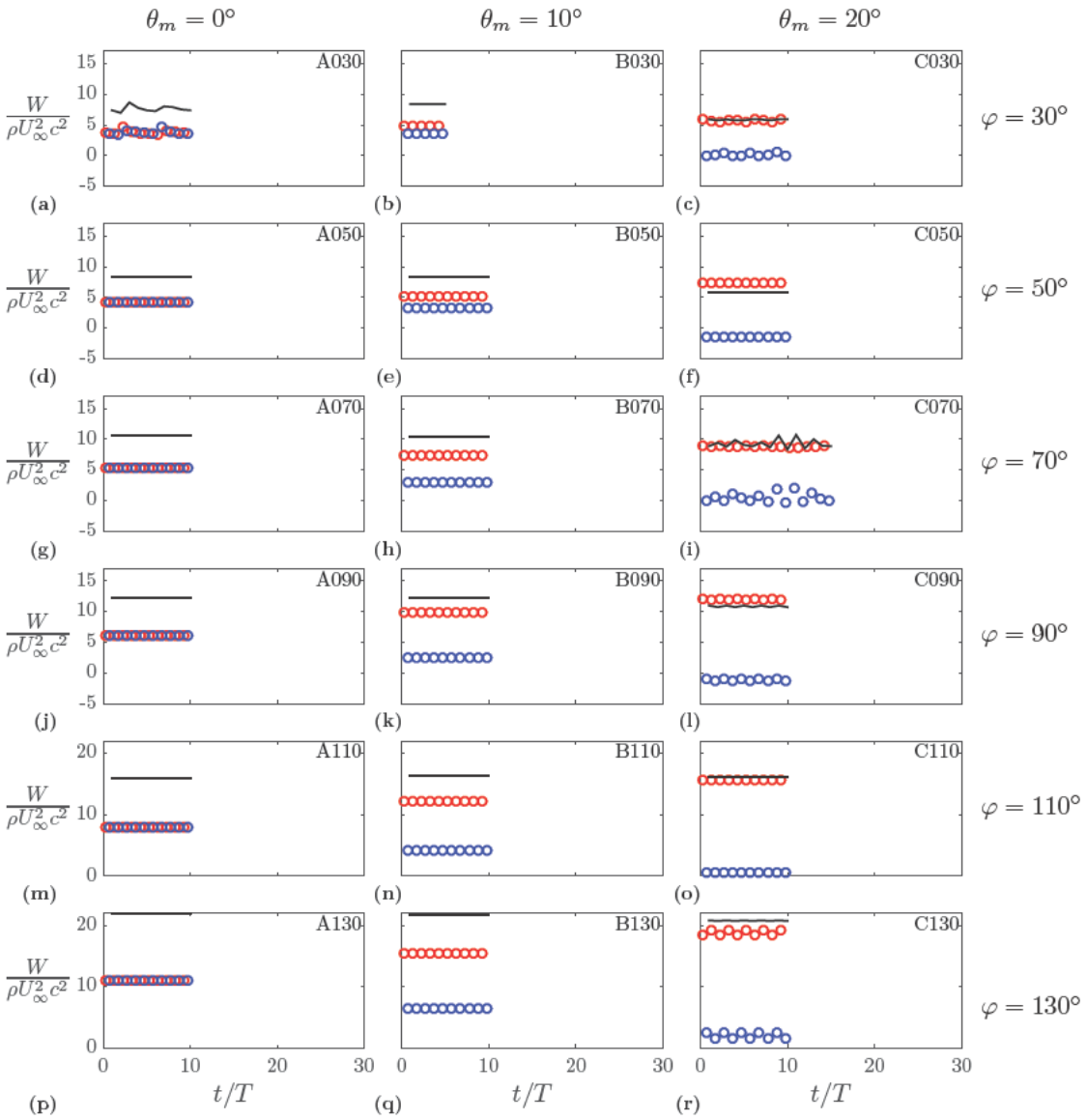

Figure A.1: Work needed to move the airfoil for each downstroke (○), upstroke (○) and the complete period (——) for the whole database of 2D cases presented in chapters 4 and 5.

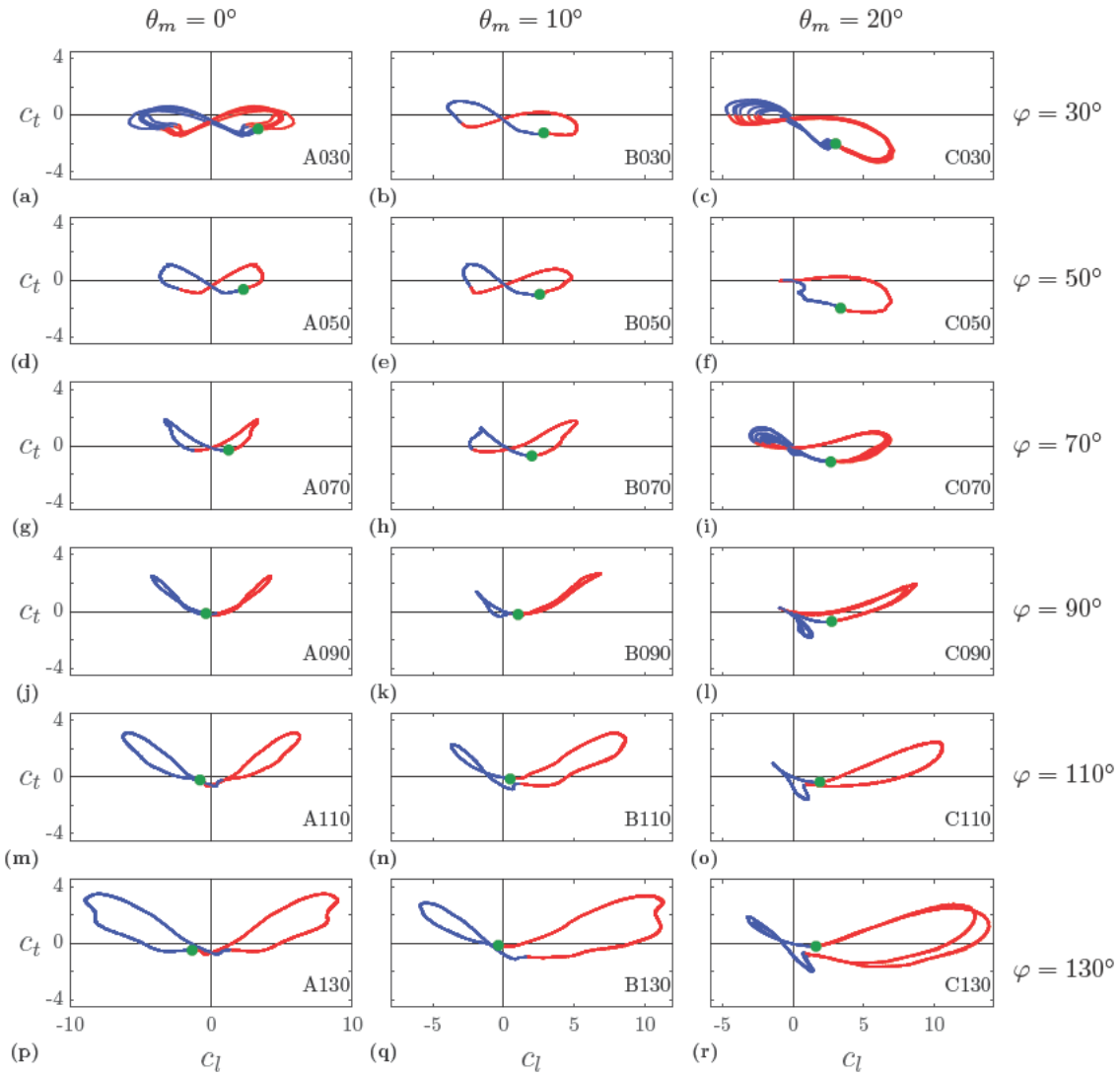

Figure A.2: Thrust versus lift for the whole database of 2D cases presented in chapters 4 and 5. The downstroke is represented in red (———) and the upstroke in blue (———). The begining of the downstroke ($t/T = 0$) is marked with a green circle (●).

A.2 Deviation from Kutta-Joukowsky

In chapter 5 the orthogonality of the contribution from vorticity within the flow with respect to the airfoil chord of case B090 was presented. In this section, we show the evolution of the angle σ (figure 5.4) for all the periodic cases of the database, except case B030. Figures A.3, A.4 and A.5 show the evolution of the angle σ with time for cases with θ_m of 0°, 10° and 20°, respectively. Also, an outline of the contribution from vorticity with in the flow at four time instants and the evolution of the modulus of the force in coefficient form

$$c_f = \sqrt{{c_t}^2 + {c_l}^2} \tag{A.2}$$

are shown for completeness. The streamwise coordinate in the frame used for the outline is given by $x' = x - U_\infty t$. Also, the line representing the angle σ and the modulus of the force is coloured in grey scale to avoid confusion to the reader when the modulus of the force is small and, therefore, the angle σ is ill defined.

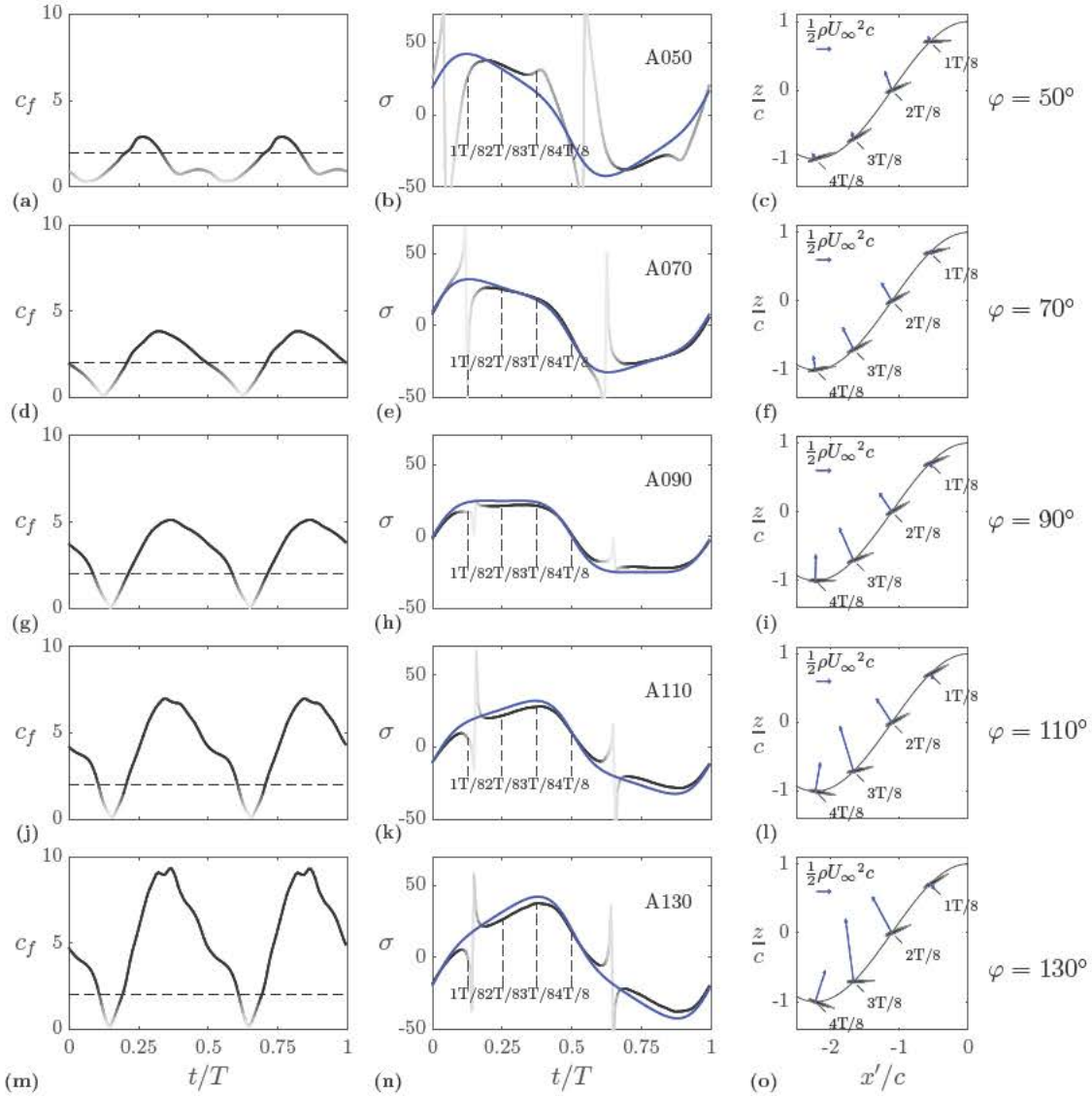

Figure A.3: Characterization of contribution within the flow to the total aerodynamic force for cases with $\theta_m = 0°$. Modulus of the force in coefficient form (left column), deviation angle σ (in degrees, middle column) and outline of the forces seen by an observer (right column). The effective angle of attack α_e (——) is represented together with the angle σ to support the results.

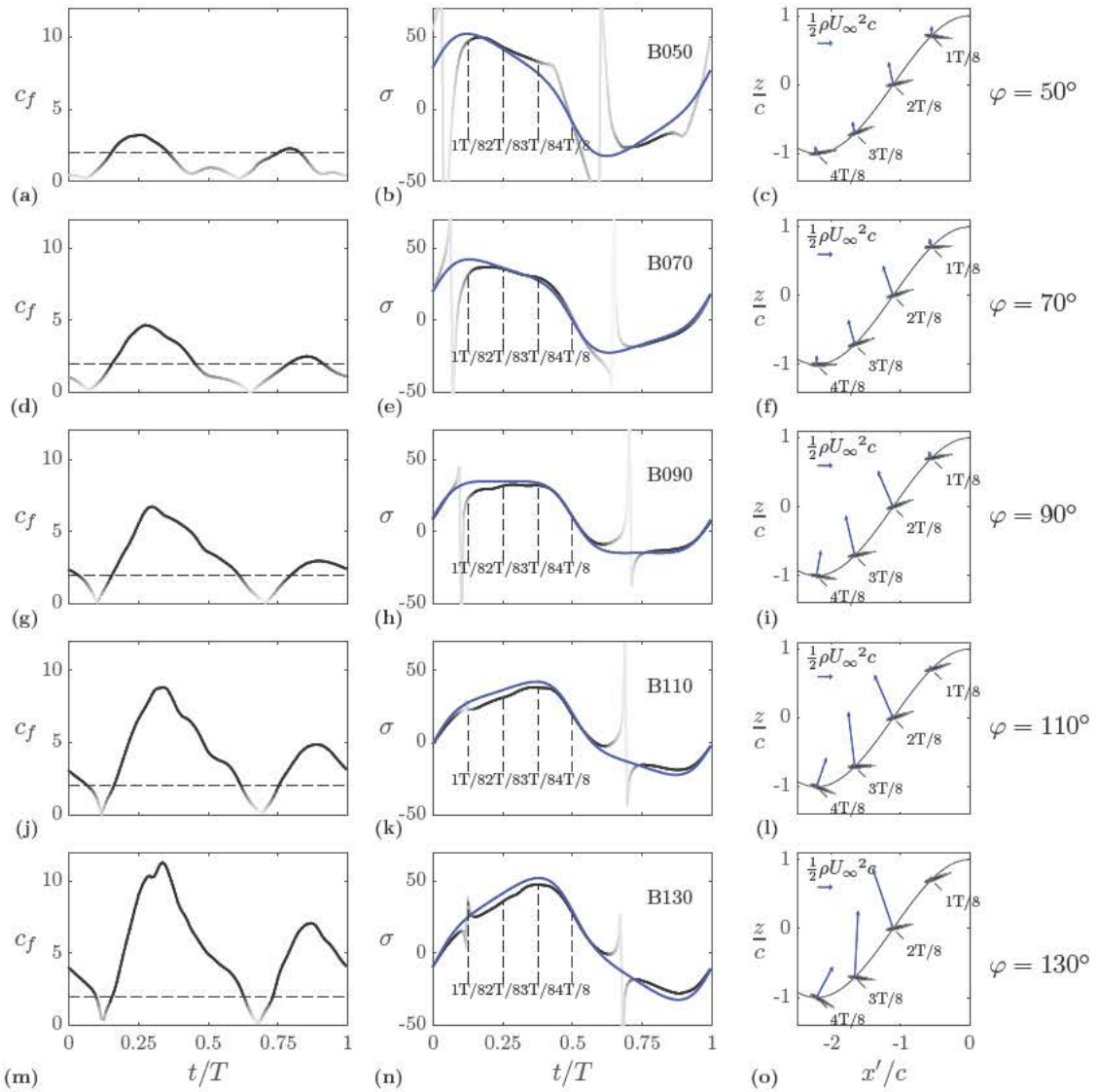

Figure A.4: Characterization of contribution within the flow to the total aerodynamic force for cases with $\theta_m = 10°$. Modulus of the force in coefficient form (left column), deviation angle σ (in degrees, middle column) and outline of the forces seen by an observer (right column). The effective angle of attack α_e (——) is represented together with the angle σ to support the results.

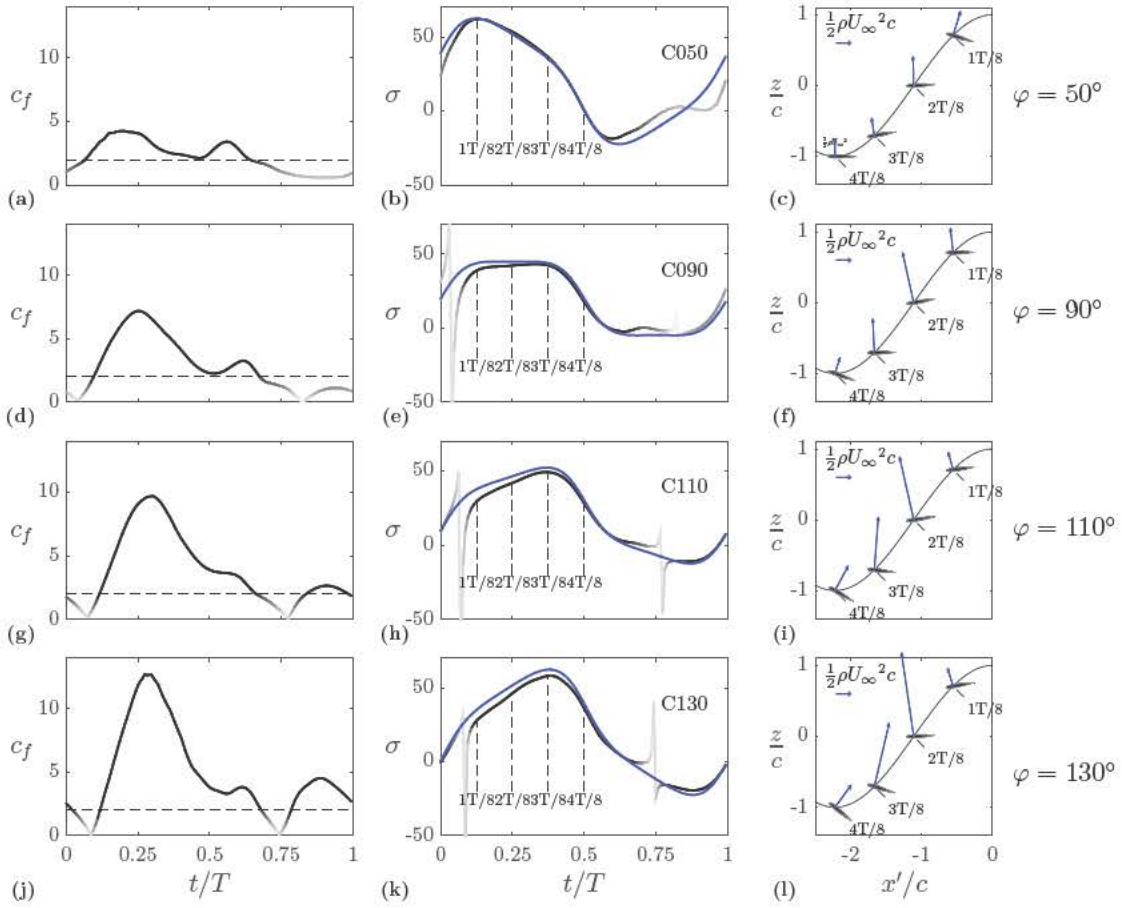

Figure A.5: Characterization of contribution within the flow to the total aerodynamic force for cases with $\theta_m = 20°$. Modulus of the force in coefficient form (left column), deviation angle σ (in degrees, middle column) and outline of the forces seen by an observer (right column). The effective angle of attack α_e (——) is represented together with the angle σ to support the results.

APPENDIX

B

Validation of Floquet stability analysis

Floquet stability analysis is carried out with a code developed in this work. This code is based on TUCAN, so the same time marching and spatial discretization are used. Some modifications are implemented to include the base flow solution and the calculations with complex numbers. In this appendix we evaluate the capability of the code developed here to perform Floquet stability analysis by comparing our results against cases from the literature for stationary and moving geometries. The first validation case is taken from Barkley and Henderson [1996], which consists of a fixed cylinder in a free stream U_∞ with $\mathrm{Re}_D = U_\infty D/\nu = 280$, where D is the diameter of the cylinder and ν is the kinematic viscosity of the fluid. For this case, we have computed the leading Floquet multipliers for three modes with spanwise wavenumbers $\beta D = 1.8$, 8 and 12. The second validation case is taken from Leontini et al. [2007]: a cylinder in a free-stream U_∞ with $Re_D = 350$, oscillating in the vertical direction with a sinusodal law

$$h = h_0 \cos(2\pi\, f\, t), \tag{B.1}$$

where $h_0/D = 0.3$ is the amplitude of the motion and f is the frequency of motion, which is set to $f\, D/U_\infty = 0.2$. In this test, the leading Floquet multiplier has been computed for a range of spanwise wavelengths $\lambda = 2\pi/\beta = [0.6D - 3D]$.

Figure B.1a shows the evolution of the L_2 norm of the perturbation velocity for some of the wavelengths evaluated of the oscillating cylinder from Leontini et al. [2007]. It can be seen that the L_2 norm of the perturbation grows exponentially with time for the unstable modes selected. It is also observed a small oscillatory component in the signal. Figure B.1b shows the evolution of the leading Floquet multiplier with time for the same cases shown in figure B.1a. The value of the leading Floquet multiplier shown in the figure is calculated by tracking the L_2 norm of the perturbation (equation (6.4)), instead of carrying out an eigenvalue problem. This approximation is good because of the exponential growth of the Floquet modes. After approximately $4 - 5$ periods, the most unstable mode dominates over the rest of the modes, resulting in a converged value for the leading Floquet multiplier. Therefore, equation (6.4) is a good approximation of the leading Floquet multiplier.

Figure B.2 shows the leading Floquet multipliers of the validation cases from Barkley

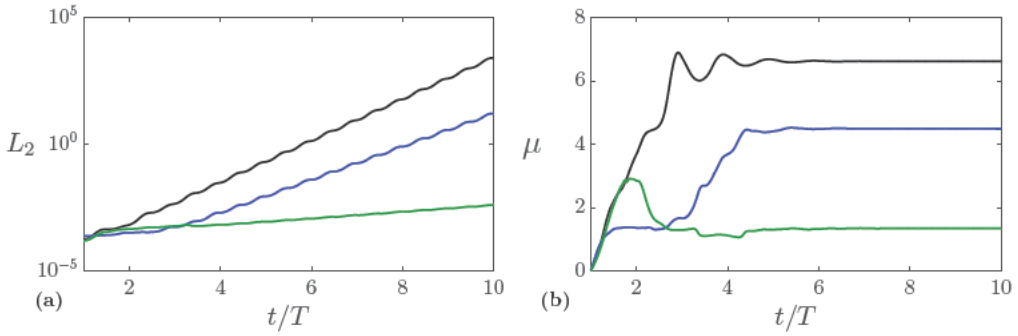

Figure B.1: Evolution of a) the L_2 norm of the perturbation velocity and b) the leading Floquet multiplier for a transverse oscillating cylinder at Re = 350. The cases shown correspond to a spanwise wavelength of $\lambda/D = 0.90$ (——), $\lambda/D = 1.20$ (——) and $\lambda/D = 1.50$ (——).

and Henderson [1996] and Leontini et al. [2007] together with the results obtained in this work. The results of the stationary cylinder are compared with the data from Barkley and Henderson [1996] in figure B.2a. The first two modes are unstable and the latter is stable, in good agreement with the reference data. Our results for the oscillating cylinder are plotted together with the data from Leontini et al. [2007] in figure B.2b. It can be observed that the same behaviour is captured with a slight quantitative difference, which can be attributed to differences in the computational domain size and resolution.

Finally, figure B.3 shows the Floquet modes of the stationary cylinder case taken from Barkley and Henderson [1996] for two spanwise wavenumbers. The results obtained in this work are in qualitative agreement with the reference. Overall, the validation tests for the Floquet analysis are satisfactory.

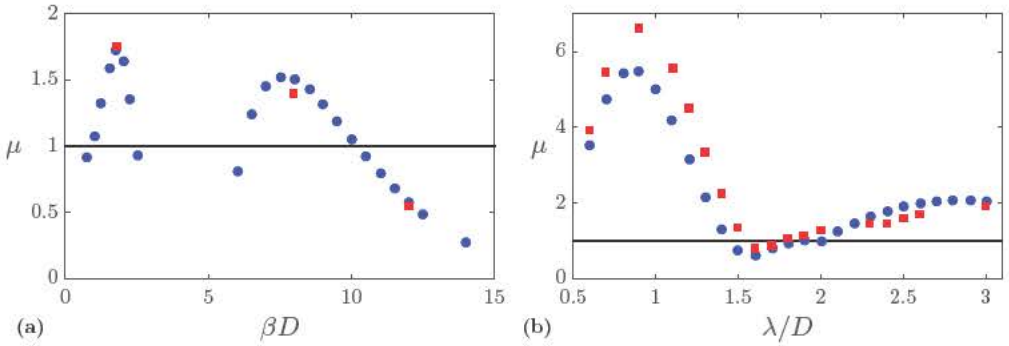

Figure B.2: Leading Floquet multiplier for a) stationary cylinder [Barkley and Henderson, 1996] versus spanwise wavenumber and b) oscillating cylinder [Leontini et al., 2007] versus spanwise wavelength. Red squares represent the present results (■) and blue circles the reference data (●).

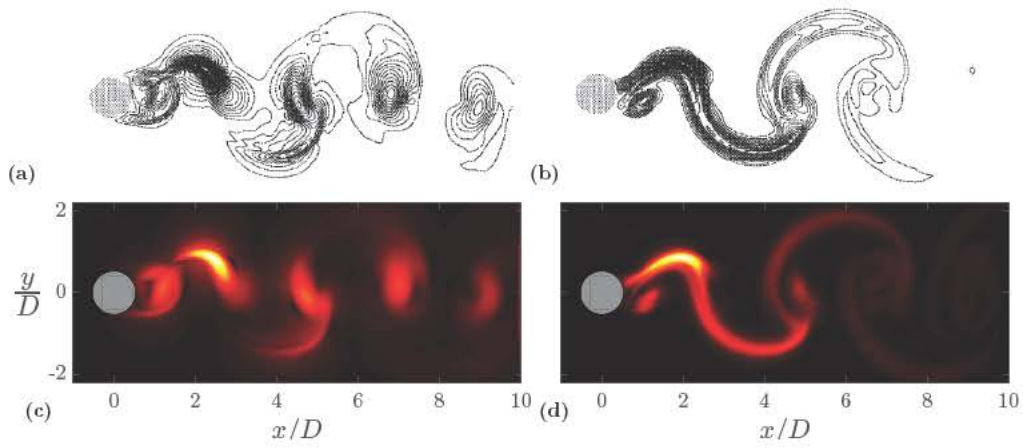

Figure B.3: Contours of $\|\hat{u}\|$ for the Floquet modes with spanwise wavenumber a) $\beta D = 0.8$ and b) $\beta D = 1.8$ from Barkley and Henderson [1996] and c) $\beta D = 0.8$ and d) $\beta D = 1.8$ obtained in this work.

APPENDIX
C

Details on the force decomposition algorithm

This appendix contains details of the algorithm used in chapter 5 to decompose the total aerodynamic force in contributions from body motion, vorticity within the flow and surface vorticity.

C.1 Definition of the auxiliary potentials

The force decomposition algorithm used in this work was first introduced by Chang [1992] and later used by Martín-Alcántara et al. [2015]. The algorithm makes use of the auxiliary potentials ϕ_x and ϕ_z (see equation (5.1)), which are calculated as

$$\nabla^2 \phi_x = 0 \tag{C.1a}$$
$$\nabla \phi_x \cdot \vec{n} = -\vec{n} \cdot \vec{e}_x U_\infty \qquad \text{At the body surface} \tag{C.1b}$$
$$\phi_x \to 0 \qquad \text{At infinity,} \tag{C.1c}$$

$$\nabla^2 \phi_z = 0 \tag{C.2a}$$
$$\nabla \phi_z \cdot \vec{n} = -\vec{n} \cdot \vec{e}_z U_\infty \qquad \text{At the body surface} \tag{C.2b}$$
$$\phi_z \to 0 \qquad \text{At infinity,} \tag{C.2c}$$

where $\vec{n}$ is the unitary normal vector pointing towards the fluid and U_∞ is the reference velocity. These potentials have analytical solution for simple geometries like ellipses, but in order to keep the capability of TUCAN of handling complex geometries with arbitrary motions, we use a numerical algorithm where the normal derivative on the surface of the body can be imposed. We decided to use the sharp interface method proposed by Mittal et al. [2008], which is based on a formulation where normal derivatives on the solid boundary are imposed by using image and ghost points.

The auxiliary potential functions ϕ_x and ϕ_z are needed at every time step in which the force decomposition is to be applied. These potential functions depend on the shape of the airfoil and on the directions in which they are computed. Note that the dependency

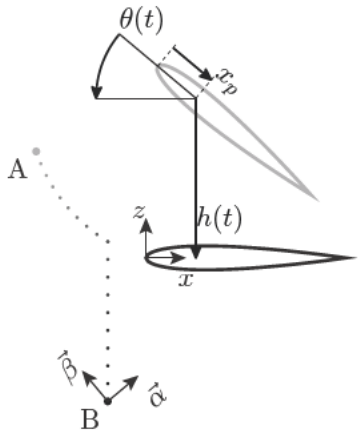

Figure C.1: Outline to represent the calculation of the auxiliary potentials ϕ_x and ϕ_z for a moving airfoil from the potentials calculated once with the airfoil at rest.

with the orientation is linear, so it is possible to show that, if $\phi_\alpha = \alpha_1\phi_x + \alpha_2\phi_z$, then ϕ_α satisfies

$$\nabla^2\phi_\alpha = 0 \tag{C.3a}$$

$$\nabla\phi_\alpha \cdot \vec{n} = -\vec{n} \cdot \vec{\alpha}\, U_\infty \qquad \text{At the body surface} \tag{C.3b}$$

$$\phi_\alpha \to 0 \qquad \text{At infinity,} \tag{C.3c}$$

where $\vec{\alpha} = \alpha_1\vec{e}_x + \alpha_2\vec{e}_z$. The linearity with the orientation eliminates the problem of having to compute the auxiliary potential functions at different time instants. Instead, the auxiliary potential functions are computed for a reference position of the airfoil, and then rotated (using (C.3)) and translated to the position of the airfoil at each time instant. Therefore, the potentials ϕ_x and ϕ_z at a point A are given by

$$\phi_x(A) = \Phi_\alpha(B) = \vec{\alpha} \cdot \vec{e_x}\, \Phi_x(B) + \vec{\alpha} \cdot \vec{e_z}\, \Phi_z(B), \tag{C.4}$$

$$\phi_z(A) = \Phi_\beta(B) = \vec{\beta} \cdot \vec{e_x}\, \Phi_x(B) + \vec{\beta} \cdot \vec{e_z}\, \Phi_z(B). \tag{C.5}$$

where the potentials Φ_x and Φ_z (figure C.2) are the auxiliary potentials calculated when the airfoil is at rest, the coordinates of B are the coordinates of A in a reference frame fixed to the airfoil (see figure C.1) and the unitary vectors $\vec{\alpha}$ and $\vec{\beta}$ are the unitary vectors $\vec{e}_x$ and $\vec{e}_z$, respectively, expressed in a reference frame fixed to the airfoil.

C.2 Algebra behing the algorithm

This section contains the details to obtain the expressions used in chapter 5 (equation (5.1)) to decompose the total aerodynamic force in contributions from body motion,

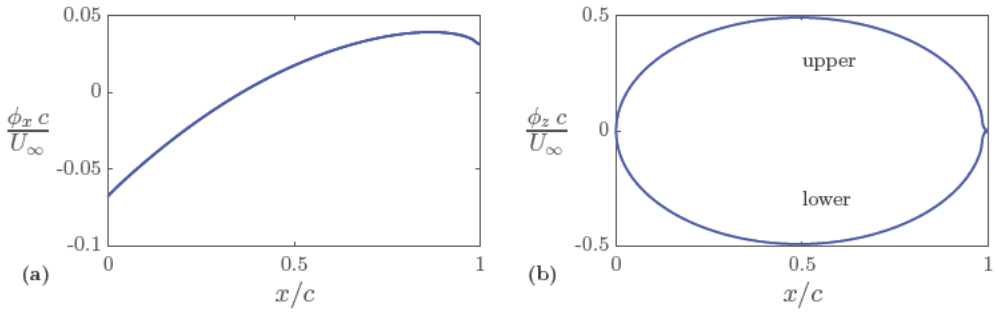

Figure C.2: Auxiliary potentials a) ϕ_x and b) ϕ_z for a NACA0012 airfoil of chord c at the reference position ($h = 0$, $\theta = 0$)

vorticity within the flow and surface vorticity. The procedure consists in manipulating Navier Stokes momentum equation

$$\frac{\partial \vec{u}}{\partial t} + (\vec{u} \cdot \nabla)\, \vec{u} = -\nabla p + \nu \nabla^2 \vec{u}, \tag{C.6}$$

to get an expression of the pressure force in one direction and, then, add the viscous force, also in this direction. First, we express the convective and diffusion terms as

$$(\vec{u} \cdot \nabla)\, \vec{u} = \frac{1}{2}\nabla(|\vec{u}|^2) - \vec{u} \times \vec{\omega}, \tag{C.7}$$

$$\nabla^2 \vec{u} = -\nabla \times \vec{\omega}. \tag{C.8}$$

Second, the pressure gradient term is isolated

$$-\nabla p = \frac{\partial \vec{u}}{\partial t} + \frac{1}{2}\nabla(|\vec{u}|^2) - \vec{u} \times \vec{\omega} + \nu \nabla \times \vec{\omega}, \tag{C.9}$$

and then we take inner product of the equation with $\nabla\phi_x$ to obtain the expressions for the force in the x direction and integrate over the whole volume:

$$-\int_V \frac{\nabla\phi_x}{U_\infty} \cdot \nabla p \, \mathrm{d}V = \underbrace{\int_V \frac{\nabla\phi_x}{U_\infty} \cdot \frac{\partial \vec{u}}{\partial t} \, \mathrm{d}V + \frac{1}{2}\int_V \frac{\nabla\phi_x}{U_\infty} \cdot \nabla(|\vec{u}|^2) \, \mathrm{d}V}_{\text{body motion (m)}}$$
$$\underbrace{-\int_V \frac{\nabla\phi_x}{U_\infty} \cdot (\vec{u} \times \vec{\omega}) \, \mathrm{d}V}_{\text{vorticity in the flow (v)}} + \underbrace{\nu \int_V \frac{\nabla\phi_x}{U_\infty} \cdot (\nabla \times \vec{\omega}) \, \mathrm{d}V}_{\text{surface vorticity (s)}}, \tag{C.10}$$

where ϕ_x is the auxiliary potential defined in equation (C.1). We only show here the calculations to obtain $\vec{F}_x$ since the procedure to obtain $\vec{F}_z$ is analogous. We proceed now by manipulating each of the terms in equation (C.10) except for the term corresponding to the vorticity within the flow. We use here the divergence theorem and the following

tensor identities

$$\nabla \cdot \left(f \vec{A} \right) = f \nabla \cdot \vec{A} + \vec{A} \cdot \nabla f, \tag{C.11}$$

$$\vec{A} \times \vec{B} \cdot \vec{C} = \vec{C} \times \vec{A} \cdot \vec{B}, \tag{C.12}$$

$$\nabla \cdot \left(\vec{A} \times \vec{B} \right) = \vec{B} \cdot \nabla \times \vec{A} - \vec{A} \cdot \nabla \times \vec{B}, \tag{C.13}$$

where f represent a scalar field and $\vec{A}$, $\vec{B}$ and $\vec{C}$ represent vector fields. The integrand of the pressure term (left hand side in equation (C.10)) is expressed as

$$\underbrace{\frac{\nabla \phi_x}{U_\infty} \cdot \nabla p}_{\text{(C.11)}: f = p,\ \vec{A} = \frac{\nabla \phi_x}{U_\infty}} = \nabla \cdot (p \frac{\nabla \phi_x}{U_\infty}) - p \nabla \cdot \cancelto{0}{\frac{\nabla \phi_x}{U_\infty}} = \nabla \cdot (p \frac{\nabla \phi_x}{U_\infty}). \tag{C.14}$$

The integrand of the first of the body motion terms (first term in the right hand side of equation (C.10)) is expressed as

$$\underbrace{\frac{\nabla \phi_x}{U_\infty} \cdot \frac{\partial \vec{u}}{\partial t}}_{\text{(C.11)}: f = \frac{\phi_x}{U_\infty},\ \vec{A} = \frac{\partial \vec{u}}{\partial t}} = \nabla \cdot (\frac{\phi_x}{U_\infty} \frac{\partial \vec{u}}{\partial t}) - \frac{\phi_x}{U_\infty} \nabla \cdot \cancelto{0}{\frac{\partial \vec{u}}{\partial t}} = \nabla \cdot (\frac{\phi_x}{U_\infty} \frac{\partial \vec{u}}{\partial t}). \tag{C.15}$$

The integrand of the second term in the body motion terms (second term in the right hand side of equation (C.10)) is expressed as

$$\underbrace{\frac{\nabla \phi_x}{U_\infty} \cdot \nabla (|\vec{u}|^2)}_{\text{(C.11)}: f = |\vec{u}|^2,\ \vec{A} = \frac{\nabla \phi_x}{U_\infty}} = \nabla \cdot (|\vec{u}|^2 \frac{\nabla \phi_x}{U_\infty}) - |\vec{u}|^2 \nabla \cdot \cancelto{0}{\frac{\nabla \phi_x}{U_\infty}} = \nabla \cdot (|\vec{u}|^2 \frac{\nabla \phi_x}{U_\infty}). \tag{C.16}$$

Finally, the surface vorticity term (last term in the right hand side of equation (C.10)) is expressed as

$$\underbrace{\frac{\nabla \phi_x}{U_\infty} \cdot \nabla \times \vec{\omega}}_{\text{(C.13)}: \vec{A} = \vec{\omega},\ \vec{B} = \frac{\nabla \phi_x}{U_\infty}} = \nabla \cdot (\vec{\omega} \times \frac{\nabla \phi_x}{U_\infty}) - \vec{\omega} \cdot \nabla \times \cancelto{0}{\frac{\nabla \phi_x}{U_\infty}} = \nabla \cdot (\vec{\omega} \times \frac{\nabla \phi_x}{U_\infty}). \tag{C.17}$$

After having expressed these terms as the divergence of a vector field, we apply the divergence theorem $\int_V \nabla \cdot \vec{F} \mathrm{d}V = \int_S \vec{n}_{out} \cdot \vec{F} \mathrm{d}A = - \int_S \vec{n} \cdot \vec{F} \mathrm{d}A$ to express these terms

as surface integrals instead of volume integrals [1]

$$\int_S p\frac{\nabla\phi_x}{U_\infty}\cdot\vec{n}\,\mathrm{d}A = \underbrace{-\int_S \frac{\phi_x}{U_\infty}\frac{\partial\vec{u}}{\partial t}\cdot\vec{n}\,\mathrm{d}A - \frac{1}{2}\int_S |\vec{u}|^2\frac{\nabla\phi_x}{U_\infty}\cdot\vec{n}\,\mathrm{d}A}_{\text{body motion (m)}} \\ \underbrace{-\int_V \frac{\nabla\phi_x}{U_\infty}\cdot(\vec{u}\times\vec{\omega})\,\mathrm{d}V}_{\text{vorticity in the flow (v)}} \underbrace{-\nu\int_S \vec{\omega}\times\frac{\nabla\phi_x}{U_\infty}\cdot\vec{n}\,\mathrm{d}A}_{\text{surface vorticity (s)}}. \tag{C.18}$$

Finally, the surface vorticity term is rewritten using identity (C.12)

$$\int_S p\frac{\nabla\phi_x}{U_\infty}\cdot\vec{n}\,\mathrm{d}A = \underbrace{-\int_S \frac{\phi_x}{U_\infty}\frac{\partial\vec{u}}{\partial t}\cdot\vec{n}\,\mathrm{d}A - \frac{1}{2}\int_S |\vec{u}|^2\frac{\nabla\phi_x}{U_\infty}\cdot\vec{n}\,\mathrm{d}A}_{\text{body motion (m)}} \\ \underbrace{-\int_V \frac{\nabla\phi_x}{U_\infty}\cdot(\vec{u}\times\vec{\omega})\,\mathrm{d}V}_{\text{vorticity in the flow(v)}} \underbrace{-\nu\int_S \vec{n}\times\vec{\omega}\cdot\frac{\nabla\phi_x}{U_\infty}\,\mathrm{d}A}_{\text{surface vorticity (s)}}. \tag{C.19}$$

The left hand side of equation (C.19) is the pressure force in the direction $\vec{e}_x$ [2], so equation (C.19) is an expression to decompose the x component of the pressure force in contributions from body motion, vorticity within the flow and surface vorticity. Also, note that the surface vorticity term (last term in equation (C.19)) is a fraction of the x component of the viscous force. Therefore, if we add the viscous force to equation (C.19), we get the x component of the total aerodynamic force decomposed in contributions from body motion, vorticity within the flow and surface vorticity

$$\begin{aligned} F_x &= \underbrace{-\int_S p\,\overbrace{\vec{n}\cdot\vec{e}_x}^{-\frac{\nabla\phi_x}{U_\infty}\cdot\vec{n}}\,\mathrm{d}A}_{\text{pressure}} + \underbrace{\nu\int_S \vec{\omega}\times\vec{n}\cdot\vec{e}_x\,\mathrm{d}A}_{\text{viscous}} \\ &= \underbrace{-\int_S \frac{\phi_x}{U_\infty}\frac{\partial\vec{u}}{\partial t}\cdot\vec{n}\,\mathrm{d}A + \frac{1}{2}\int_S |\vec{u}|^2\vec{n}\cdot\vec{e}_x\,\mathrm{d}A}_{\text{body motion (m)}} \\ &\quad \underbrace{-\int_V (\vec{u}\times\vec{\omega})\cdot\frac{\nabla\phi_x}{U_\infty}\mathrm{d}V}_{\text{vorticity in the flow (v)}} + \underbrace{\nu\int_S (\vec{\omega}\times\vec{n})\cdot(\frac{\nabla\phi_x}{U_\infty}+\vec{e}_x)\,\mathrm{d}A}_{\text{surface vorticity (s)}}. \end{aligned} \tag{C.20}$$

[1] Note that the divergence theorem is applied to the fluid domain and that we define $\vec{n}$ as the unitary normal vector pointing from the solid to the fluid

[2] $\vec{e}_x\cdot\vec{n} = -\frac{\nabla\phi_x}{U_\infty}\cdot\vec{n}$ on the surface of the airfoil (equation (C.1b))

We write the expression for the z component for completness

$$\begin{aligned} F_z =& \underbrace{-\int_S p \overbrace{\vec{n}\cdot\vec{e}_z}^{-\frac{\nabla\phi_x}{U_\infty}\cdot\vec{n}} \,\mathrm{d}A}_{\text{pressure}} + \underbrace{\nu\int_S \vec{\omega}\times\vec{n}\cdot\vec{e}_z\,\mathrm{d}A}_{\text{viscous}} \\ =& \underbrace{-\int_S \frac{\phi_z}{U_\infty}\frac{\partial\vec{u}}{\partial t}\cdot\vec{n}\,\mathrm{d}A + \frac{1}{2}\int_S |\vec{u}|^2\,\vec{n}\cdot\vec{e}_z\,\mathrm{d}A}_{\text{body motion (m)}} \\ & \underbrace{-\int_V (\vec{u}\times\vec{\omega})\cdot\frac{\nabla\phi_x}{U_\infty}\mathrm{d}V}_{\text{vorticity in the flow (v)}} + \underbrace{\nu\int_S (\vec{\omega}\times\vec{n})\cdot\left(\frac{\nabla\phi_x}{U_\infty}+\vec{e}_z\right)\mathrm{d}A}_{\text{surface vorticity (s)}}. \end{aligned} \tag{C.21}$$

The integrand of the contribution of the vorticity within the flow can be interpreted as force density

$$\delta_x = \frac{-2\,(\vec{u}\times\vec{\omega})\cdot\nabla\phi_x}{{U_\infty}^3 c^2}, \tag{C.22a}$$

$$\delta_z = \frac{-2\,(\vec{u}\times\vec{\omega})\cdot\nabla\phi_z}{{U_\infty}^3 c^2}. \tag{C.22b}$$

C.3 Potential code validation

In this section we present some tests to validate the tool developed to calculate the auxiliary potentials ϕ_x and ϕ_z. It was decided that the best method to use in order to keep the versatility of TUCAN of handling complex geometries in motion was the sharp interface IBM described by Mittal et al. [2008]. The validation process has been divided into three parts. First, we have done a quantitative evaluation of the numerical solution obtained for ϕ_x and ϕ_z for elliptic airfoils. Then, we have performed a qualitative analysis of the spatial gradients of the potentials obtained for a circular cylinder and, also, the volume thrust density obtained for the initial stages of the cross flow over this cylinder. Finally, we have reproduced the analysis of Martín-Alcántara et al. [2015] for an elliptic airfoil set in pure heaving and compared our results against theirs.

In the following sections we use the analytical solution of the auxiliary potentials for an ellipse of major axis c

$$\phi_x = \frac{cU_\infty}{2}\sqrt{\frac{1+\epsilon}{1-\epsilon}}\mathrm{e}^{-\xi}\left(\sin\theta\sin\eta + \epsilon\cos\theta\cos\eta\right), \tag{C.23a}$$

$$\phi_z = \frac{cU_\infty}{2}\sqrt{\frac{1+\epsilon}{1-\epsilon}}\mathrm{e}^{-\xi}\left(\cos\theta\sin\eta - \epsilon\sin\theta\cos\eta\right), \tag{C.23b}$$

where ξ and η are the radial and angular elliptic coordinates, respectively, ϵ is the ratio of the major axes and the minor axes, U_∞ is the free stream velocity and θ is the angle of attack. The cartesian coordinates in a reference frame fixed to the airfoil (figure C.3)

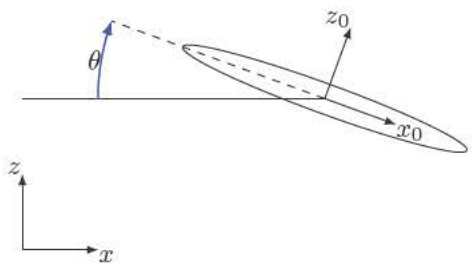

Figure C.3: Outline of the cartesian coordiantes in a reference frame fixed to the airfoil

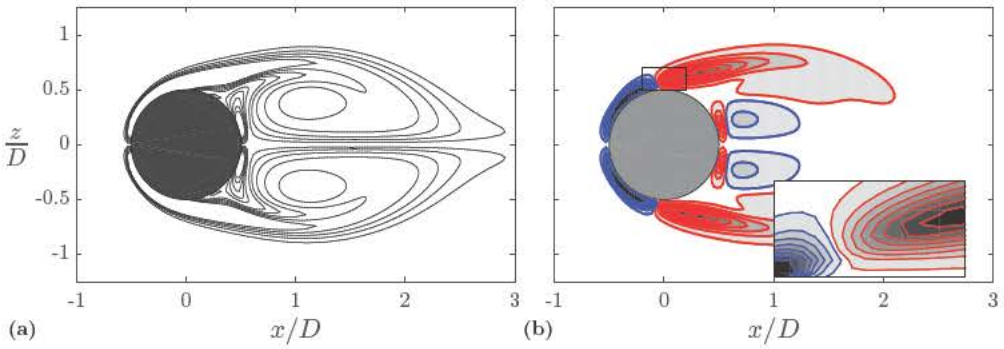

Figure C.4: a) Vorticity and b) thrust density contours for cross flow over a circular cylinder at Re = 300. Filled contours in b) are obtained with the numerical solution of the potential ϕ_x and line countours of thrust (——) and drag (——) density with the exact solution for an ellipse with $\epsilon \to 1$.

are given in terms of the elliptic coordinates as

$$x_0 = \frac{c}{2}\sqrt{1-\epsilon^2}\cosh\xi\cos\eta, \tag{C.24a}$$

$$z_0 = \frac{c}{2}\sqrt{1-\epsilon^2}\sinh\xi\sin\eta. \tag{C.24b}$$

C.3.1 Cross flow over circular cylinder

The next validation case is the flow around a circular cylinder at a Reynolds number Re = 300. Although the solution for this case is unsteady, resulting in the classical Von-Karman vortex street once the problem is statistically converged, we only analyze here the solution before the vortex street is formed. Figure C.4a shows isocontours of spanwise vorticity ω_y at $tU_\infty/D = 6$, when the circulation bubble behind the cylinder is growing, but still vortex are not being shed into the wake. Figure C.4b shows isocontours of the volumetric thrust density generated with the auxiliary potential ϕ_x obtained numerically

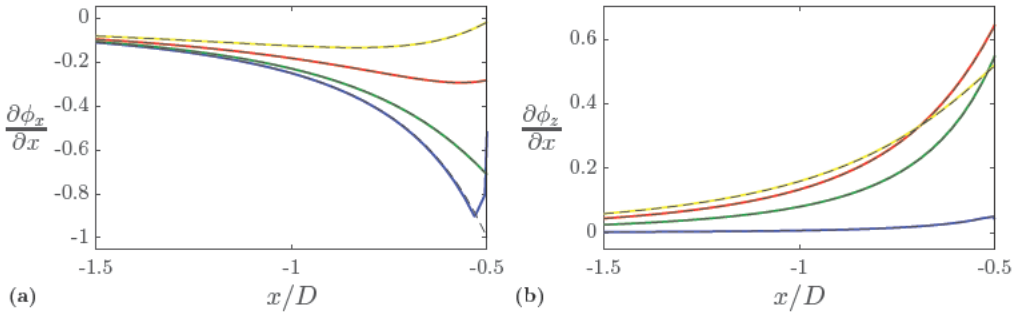

Figure C.5: Comparison of the spatial derivatives a) $\frac{\partial \phi_x}{\partial x}$ and b) $\frac{\partial \phi_z}{\partial x}$ for a circular cylinder of diameter D obtained numerically against the exact solution (- - -). The curves correspond to different vertical positions $z/D = 0.01$ (———), $z/D = 0.17$ (———), $z/D = 0.33$ (———) and $z/D = 0.48$ (———).

(filled contours in grey) and with the exact solution (line contours). It can be seen that both fields, the thrust density obtained numerically and the exact solution of ϕ_x are in very good agreement.

The spatial gradients of the potentials ($\frac{\partial \phi_x}{\partial x}$ and $\frac{\partial \phi_z}{\partial x}$) for the cylinder case are shown in figure C.5. It can be seen that the gradients calculated with the potentials obtained numerically are in agreement with the gradients calculated with the exact solution of the potentials.

C.3.2 Cross flow over elliptic airfoil in pure heaving

The validation case presented in this section is taken from the work of Martín-Alcántara et al. [2015]. This test consists in the flow over an elliptic airfoil at a Reynolds number $\mathrm{Re} = U_\infty c/\nu = 500$ in pure heaving motion. The amplitude of the motion is $h_0/c = 0.32$ and the reduced frequency $k = 2\pi f c/U_\infty = \pi$. We proceed to carry out a qualitative evaluation of the results by generating the base flow, calculating the force density (equation (C.22a)) and, then, comparing our results against the results from the reference. Figure C.6 shows contours of streamwise force density δ_x obtained in this work (yellow-green line contours) and the results from the reference (red-blue filled contours). The filled contours are taken directly from figure 5 of the work of Martín-Alcántara et al. [2015]. The small differences between our results and the references can be attributed to differences in the base flow because of the different transients of the solution and the different numerical methods used. We consider this validation test as successful.

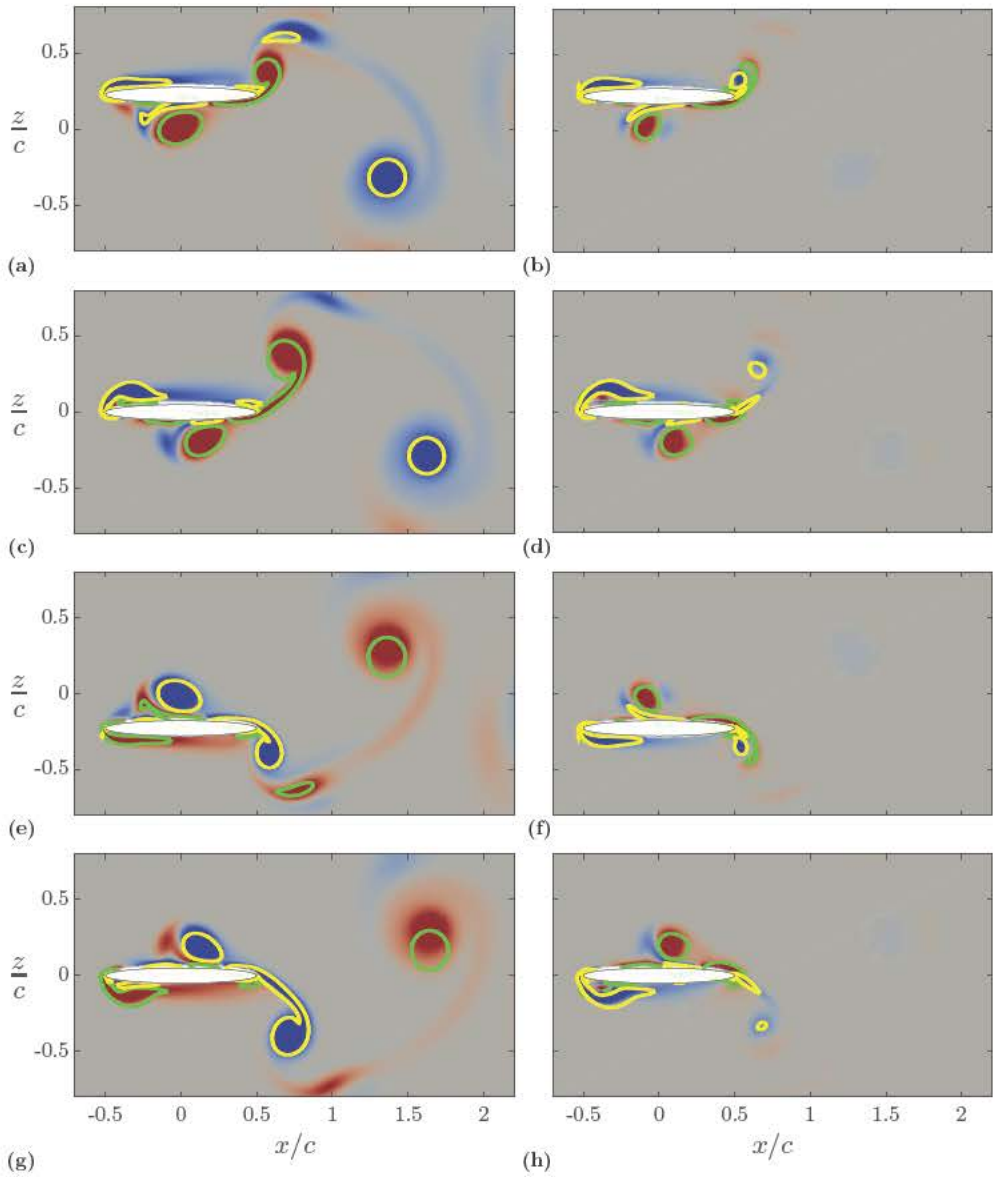

Figure C.6: Snapshots of spanwise vorticity (left) and streamwise force density at different instants durint the motion period. Filled contours are taken from the work of Martín-Alcántara et al. [2015] and line contours are calculated with TUCAN. The values of spanwise vorticity represented are $\omega_y\, c/U_\infty = -15$ ( ) and $\omega_y\, c/U_\infty = 15$ ( ). The values of force density represented are $\delta_x = -2.5$ ( ) and $\delta_x = 2.5$ ( ).

C.4 Analytic solution of body motion contribution for a flat plate

In this section we obtain an analytical solution for the body motion contribution to the total aerodynamic force (equation (C.20)) for a flat plate of length c in heaving and pitching motion. The pivoting point is the middle of the plate. We use the analytical solution of the potentials ϕ_x and ϕ_z for an ellipse with thickness ratio $\epsilon = 0$.

The solution of the potentials on the surface of the ellipse are given by

$$\phi_x = \frac{cU_\infty}{2}\left(\sin\theta\sin\eta + \epsilon\cos\theta\cos\eta\right) \tag{C.25a}$$

$$\phi_z = \frac{cU_\infty}{2}\left(\cos\theta\sin\eta - \epsilon\sin\theta\cos\eta\right) \tag{C.25b}$$

A flat plate si obtained when $\epsilon = 0$, so the coordinates

$$x_0 = \frac{c}{2}\cos\eta \tag{C.26a}$$

$$z_0 = 0 \tag{C.26b}$$

And the solutions of the potentials on the ellipse in elliptic coordinates are

$$\phi_x = \frac{cU_\infty}{2}\sin\theta\sin\eta, \tag{C.27a}$$

$$\phi_z = \frac{cU_\infty}{2}\cos\theta\sin\eta. \tag{C.27b}$$

The potentials ϕ_x and ϕ_z in cartesian coordinates are given by

$$\phi_x = \begin{cases} \frac{cU_\infty}{2}\sin\theta\sqrt{1-4x^2} & 0<\eta<\pi \quad \text{Upper surface} \\ -\frac{cU_\infty}{2}\sin\theta\sqrt{1-4x^2} & \pi<\eta<2\pi \quad \text{Lower surface} \end{cases}, \tag{C.28a}$$

$$\phi_z = \begin{cases} \frac{cU_\infty}{2}\cos\theta\sqrt{1-4x^2} & 0<\eta<\pi \quad \text{Upper surface} \\ -\frac{cU_\infty}{2}\cos\theta\sqrt{1-4x^2} & \pi<\eta<2\pi \quad \text{Lower surface} \end{cases}. \tag{C.28b}$$

The acceleration on the flat plate is given by

$$\ddot{x}(x_0) = -x_0\left(\ddot{\theta}\sin\theta + \dot{\theta}^2\cos\theta\right) \tag{C.29a}$$

$$\ddot{z}(x_0) = \ddot{h} - x_0\left(\ddot{\theta}\cos\theta - \dot{\theta}^2\sin\theta\right) \tag{C.29b}$$

The unitary normal vector is given by

$$\vec{n} = \begin{cases} (\sin\theta, \cos\theta) & 0<\eta<\pi \quad \text{Upper surface} \\ (-\sin\theta, -\cos\theta) & \pi<\eta<2\pi \quad \text{Lower surface} \end{cases} \tag{C.30}$$

We have ${\phi_x}^U = -{\phi_x}^L$, ${\phi_z}^U = -{\phi_z}^L$ and $\vec{n}^U = -\vec{n}^L$, where the superindices U and L indicate upper and lower surface, respectively. Therefore, we only need to evaluate the

upper surface of the plate

$$\int_S \frac{\phi_x}{U_\infty}\frac{d\vec{v}}{dt}\cdot\vec{n}\mathrm{d}A = 2\int_U \frac{{\phi_x}^U}{U_\infty}\frac{d\vec{v}}{dt}\cdot\vec{n}^U\mathrm{d}A, \tag{C.31}$$

$$\int_S \frac{\phi_z}{U_\infty}\frac{d\vec{v}}{dt}\cdot\vec{n}\mathrm{d}A = 2\int_U \frac{{\phi_z}^U}{U_\infty}\frac{d\vec{v}}{dt}\cdot\vec{n}^U\mathrm{d}A. \tag{C.32}$$

First, let as develop the integrand

$${\phi_x}^U\frac{d\vec{u}}{dt}\cdot\vec{n}^U = C_x\sqrt{1-4x_0^2}\left(-A\,x_0+\ddot{h}\cos\theta\right), \tag{C.33}$$

$${\phi_z}^U\frac{d\vec{u}}{dt}\cdot\vec{n}^U = C_z\sqrt{1-4x_0^2}\left(-A\,x_0+\ddot{h}\cos\theta\right), \tag{C.34}$$

$$\tag{C.35}$$

where $C_x = \frac{c}{2}\sin\theta$, $C_z = \frac{c}{2}\cos\theta$ and $A = \left(\ddot{\theta}\sin\theta+\dot{\theta}^2\cos\theta\right)\sin\theta+\left(\ddot{\theta}\cos\theta-\dot{\theta}^2\sin\theta\right)\cos\theta$. We continue integrating the equation

$$\begin{aligned}\int_U {\phi_x}^U\frac{d\vec{v}}{dt}\cdot\vec{n}^U\mathrm{d}A =& C_x\cos\theta\ddot{h}\int_{-c/2}^{c/2}\sqrt{1-4x_0^2}\mathrm{d}A - A\,C_x\int_{-c/2}^{c/2}x_0\sqrt{1-4x_0^2}\mathrm{d}A\\ =& C_x\cos\theta\ddot{h}\frac{\pi\,c}{4} = \frac{\pi c^2}{8}\sin\theta\cos\theta\,\ddot{h},\end{aligned} \tag{C.36a}$$

$$\begin{aligned}\int_U {\phi_z}^U\frac{d\vec{v}}{dt}\cdot\vec{n}^U\mathrm{d}A =& C_z\cos\theta\ddot{h}\int_{-c/2}^{c/2}\sqrt{1-4x_0^2}\mathrm{d}A - A\,C_z\int_{-c/2}^{c/2}x_0\sqrt{1-4x_0^2}\mathrm{d}A\\ =& C_z\cos\theta\ddot{h}\pi/4 = \frac{\pi}{8}\cos^2\theta\,\ddot{h}.\end{aligned} \tag{C.36b}$$

So finally, the term we are interested in reads:

$${F_x}^m = -2\rho\int_U \frac{{\phi_x}^U}{U_\infty}\frac{d\vec{v}}{dt}\cdot\vec{n}^U\mathrm{d}A = -\frac{\pi c^2}{4}\sin\theta\cos\theta\,\ddot{h} = -\frac{\pi c^2}{8}\sin 2\theta\,\ddot{h} \tag{C.37a}$$

$${F_z}^m = -2\rho\int_U \frac{{\phi_z}^U}{U_\infty}\frac{d\vec{v}}{dt}\cdot\vec{n}\mathrm{d}A = -\frac{\pi c^2}{4}\cos^2\theta\,\ddot{h}. \tag{C.37b}$$

The last step is express the value of the force as non-dimensional coefficients

$${c_t}^m = -\frac{2{F_x}^m}{\rho c{U_\infty}^2} = \frac{\pi}{4}\frac{\ddot{h}}{{U_\infty}^2/c}\sin(2\theta) \tag{C.38a}$$

$${c_l}^m = \frac{2{F_z}^m}{\rho c{U_\infty}^2} = -\frac{\pi}{2}\frac{\ddot{h}}{{U_\infty}^2/c}\cos^2\theta \tag{C.38b}$$

APPENDIX

D

Added mass modelling from potential theory

This chapter contains the expressions from Sedov et al. [1965] used to compute added mass terms in chapter 5 for modelling purposed.

The formulas from Sedov read

$$X_0 = -\lambda_x \dot{U_0} - \lambda_{xy} \dot{V_0} - \lambda_{xw} \dot{\Omega} + \Omega \left(\lambda_{xy} U_0 + \lambda_y V_0 + \lambda_{yw} \Omega \right) \tag{D.1a}$$

$$Y_0 = -\lambda_{xy} \dot{U_0} - \lambda_y \dot{V_0} - \lambda_{yw} \dot{\Omega} - \Omega \left(\lambda_x U_0 + \lambda_{xy} V_0 + \lambda_{xw} \Omega \right) \tag{D.1b}$$

Where λ_* are the coefficients for virtual mass and U_0, V_0 and Ω are the translational velocity in x and y directions and the angular velocity, respectively, of the center of gravity of the airfoil in a reference frame fixed to the airfoil. The values of the virtual mass coefficients for a flat plate of chord c are taken from Sedov et al. [1965]

$$\lambda_x = \lambda_{xy} = \lambda_{xw} = 0 \tag{D.2a}$$

$$\lambda_y = \rho \pi \frac{c}{2}^2 \tag{D.2b}$$

$$\lambda_{yw} = \rho \pi \frac{c}{3}^2 \tag{D.2c}$$

$$\lambda_w = \frac{9}{8} \rho \pi \frac{c}{4}^2 . \tag{D.2d}$$

Taking into account the coefficients for a flat plate, equation (D.1) is simplified

$$X_0 = \Omega \left(\lambda_y \, V_0 + \lambda_{yw} \Omega \right) \tag{D.3a}$$

$$Y_0 = -\lambda_y \dot{V_0} - \lambda_{yw} \dot{\Omega}. \tag{D.3b}$$

The velocity of the center of gravity of the plate are given by

$$U_0 = -\dot{h} \sin \theta \tag{D.4a}$$

$$V_0 = \quad \dot{h} \cos \theta - \dot{\theta} (\xi - x_p) \tag{D.4b}$$

$$\Omega = -\dot{\theta}, \tag{D.4c}$$

and their time derivatives by

$$\dot{U}_0 = -\ddot{h}\sin\theta - \dot{h}\dot{\theta}\cos\theta \tag{D.5a}$$

$$\dot{V}_0 = \quad \ddot{h}\cos\theta - \dot{h}\dot{\theta}\sin\theta - \ddot{\theta}(\xi - x_p) \tag{D.5b}$$

$$\dot{\Omega} = -\ddot{\theta}. \tag{D.5c}$$

So the forces in a reference frame fixed to the airfoil are given by

$$X_0 = -\lambda_y \dot{h}\dot{\theta}\sin\theta + \lambda_{yw}\ddot{\theta} \tag{D.6a}$$

$$Y_0 = \lambda_y\left(\dot{h}\dot{\theta}\sin\theta - \ddot{h}\cos\theta + \ddot{\theta}^2 r\right) + \lambda_{yw}\ddot{\theta}, \tag{D.6b}$$

where $r = (\xi - x_p)$.

The forces in the reference coordinate frame are given by

$$\begin{aligned} {F_x}^a =& X_0\cos\theta + Y_0\sin\theta \\ =& -\lambda_y\ddot{h}\left(\cos\theta\sin\theta\right) + \lambda_y\dot{h}\dot{\theta}\left(\sin^2\theta - \cos^2\theta\right) + \lambda_y\ddot{\theta}r\sin\theta \\ &+ \lambda_{yw}\left(\dot{\theta}^2\cos\theta + \ddot{\theta}\sin\theta\right) \\ =& -\frac{\lambda_y}{2}\ddot{h}\sin(2\theta) - \lambda_y\dot{h}\dot{\theta}\cos(2\theta) + \lambda_y\ddot{\theta}r\sin\theta \\ &+ \lambda_{yw}\left(\dot{\theta}^2\cos\theta + \ddot{\theta}\sin\theta\right), \end{aligned} \tag{D.7a}$$

$$\begin{aligned} {F_y}^a =& -X_0\sin\theta + Y_0\cos\theta \\ =& -\lambda_y\ddot{h}\cos^2\theta + \lambda_y\dot{h}\dot{\theta}\sin(2\theta) + \lambda_y\ddot{\theta}r\cos\theta \\ &+ \lambda_{yw}\left(\ddot{\theta}\cos\theta - \dot{\theta}^2\sin\theta\right). \end{aligned} \tag{D.7b}$$

And finally in non-dimensional form of thrust and lift

$$\begin{aligned} {c_t}^a =& -\frac{2{F_x}^a}{\rho c {U_\infty}^2} \\ =& \frac{\pi}{4}\frac{\ddot{h}}{{U_\infty}^2/c}\sin(2\theta) + \frac{\pi}{2}\frac{\dot{h}}{U_\infty}\frac{\dot{\theta}}{U_\infty/c}\cos(2\theta) + \frac{\pi}{2}\frac{\ddot{\theta}}{{U_\infty}^2/c^2}\frac{r}{c}\sin\theta \\ &- \frac{2\pi}{9}\left(\frac{\dot{\theta}^2}{{U_\infty}^2/c^2}\cos\theta + \frac{\ddot{\theta}}{{U_\infty}^2/c^2}\sin\theta\right), \end{aligned} \tag{D.8a}$$

$$\begin{aligned} {c_l}^a =& \frac{2{F_y}^a}{\rho c {U_\infty}^2} \\ =& -\frac{\pi}{2}\frac{\ddot{h}}{{U_\infty}^2/c}\cos^2\theta + \frac{\pi}{2}\frac{\dot{h}}{U_\infty}\frac{\dot{\theta}}{U_\infty/c}\sin(2\theta) + \frac{\pi}{2}\frac{\ddot{\theta}}{{U_\infty}^2/c^2}\frac{r}{c}\cos\theta \\ &+ \frac{\pi}{9}\left(\frac{\ddot{\theta}}{{U_\infty}^2/c^2}\cos\theta - \frac{\dot{\theta}^2}{{U_\infty}^2/c^2}\sin\theta\right). \end{aligned} \tag{D.8b}$$

Acknowledgments

The research presented in this thesis has been carried out in the department of Bioengineering and Aerospace engineering at Universidad Carlos III de Madrid. The financial support has been provided by Universidad Carlos III de Madrid through a PIF scholarship and by the Spanish Ministry of Economy and Competitiveness through grants TRA2012-37714 and TRA2013-41103-P.

Y para terminar me gustaría agradecer a todas las personas que han contribuido directa o indirectamente a esta tesis. Empezando por Óscar y a Manolo, gracias por confíar en mí, por enseñarme todo lo que se sobre mecánica de fluidos y por tener paciencia con todo lo que no sabía. Gracias por lidiar con las condiciones de contorno y mostrarme siempre vuestro apoyo. Gracias Óscar (tiembla porque aquí te puedo hacer la pelota tanto como quiera, que para eso es mi tesis) por todo el apoyo en el desarrollo del código, en el manejo del a veces odiado icaro y por alternar tu alta exigencia en el trabajo con un optimismo incondicional. A Manolo, gracias por aparecer un día con la niña bonita de mi tesis (ver capítulo 6) y motivarme siempre con los resultados obtenidos. Gracias por tratarme fuera del trabajo como a un igual, por llevarme al Vogel Brau y por introducirme al grupo de Markus.

A mi familia, que siempre me ha apoyado en este camino universitario. Gracias a mi padre por transmitirme una filosofía de vida única, en la que portarse mal y disfrutar es tan importante como ser responsable. A mi madre, por inculcarme una afición por el deporte que forma parte de mi día a día y de la cual me beneficio en muchos aspectos de mi vida. A mi hermano por, básicamente, todo. Por siempre poder contar contigo y porque una escapada en bici o corriendo contigo vale mucho! A Vero por estar pendiente, por apoyarme en momentos críticos y, como no, por ese Ángel que has traído al mundo.

A Leti, gracias por ser una pieza clave en todos estos años. Por todo el apoyo académico y, sobre todo, el personal. Por descubrirme a Florence en nuestro primer despacho (y seguramente el más grande de nuestras vidas), por las noches de fiesta, por escucharme y por mil cosas que podría escribir en varias páginas. No puedo esperar a ver tu tesis, mucho ánimo con la recta final. Sweet love.

Quiero agradecer especialmente a Alex todo su trabajo y apoyo en estos años. Por hacer un TUCAN mejor y por dar contunuidad a toda la maquinaria creada para procesar resultados. No concibo un compañero de trabajo mejor (ni nadie capaz de entender los códigos que hacen códigos que no hacen comentarios).

Gracias a Susana y a Reyes por haber sido parte de la mesa redonda en la que se decidió que hacer esta tesis era una buena idea. Además, por la mezcla de risas, juergas y conversaciones para arreglar tanto el mundo como nuestras vidas cada vez que nos

juntamos. Gracias también a Elena, por ser parte de esos cafés interminables en los que se mezclan trabajo y amistad, y con los que la toma de decisiones difíciles se hace mucho más fácil.

Y de una empresa de Derby, de cuyo nombre no quiero acordarme, llegó alguien que junto con Sara, Dani (el grande), David y Carlos, habéis sido muy importantes en estos años. Espero que esto sea el principio de una larga amistad. Quiero agradecer especialmente a Sara todas esas conversaciones cargadas de humor absurdo que hemos alternado con la seriedad de la política, la ciencia y, como no, el amor.

Gracias Tamara por ser una parte imprescindible de mi vida durante estos 28 años de amistad. No se me ocurre mejor manera de pasar un viernes que con mala TV y comida basura. Si tengo que destacar algo de todos estos años es la capacidad de celebrar todo lo bueno que nos pasa en la vida y de reírnos de todo lo malo. Gracias por supuesto también a Isra por formar parte de esos viernes (y por aguantarnos).

Gracias a amigos como Alber, por compartir piso, risas, resacas y tener la genial idea de cuantificar la programación. A Alvaro y a Maite, amigos de hace muchos años con los que siempre se puede contar. No me puedo olvidar de mis amigas de Maristas. De María, que con muy poco, me ayudó mucho. Y ni mucho menos de Chus y su conquista de Alemania. Gracias también a Alex por ser la persona más divertida que conozco y Manu por haber vivido todos estos años universitarios.

Gracias a todos los compañeros de Aero. Especialmente, gracias a Manuel por formar parte de esto desde el principio. También me gustaría dar las gracias a Javi por su pasión por la ciencia y su constante buen humor.

I also want to thank Markus, Agathe, Todor, Yoshi and Aman for hosting me during my stays at KIT. Thank you for the scientific support and for the great moments at Vogel Brau or replacing lunch by skating time.

Quiero también dar las gracias a Beatriz y María Jesús por vuestro apoyo desde que os conozco (hace ya unos cuantos años), ya sea en una charla fugaz por los pasillos o en una conversación profunda sobre la docencia o mi futuro. Gracias Guadalupe por enseñarme mis primeros pasos en el camino del numérico. Ojalá hubiese más profesores en la Universidad con vuestra implicación en el trabajo.

También quiero dar la gracias a los alumnos que han formado parte del grupo de CFD, especialemente a Gonzalo y a Enri por su implicación con TUCAN. Espero Enri que toda esa motivación te lleve a donde quieras!.

Gracias a Marcos, Eva, Carlos y sobre todo a Noe por todo lo que he aprendido con vosotros. Por llenar mis paseos de complicaciones que sólo la personalinad de Orión podría compensar. Sin la parte perruna esta tesis no habría sido tan cognitivo-emocionante.

Y Germán, no te libras. Gracias por las risas, los Netflix, los cacharritos, por aceptar a Orión (aunque no haya puesto mucho de su parte) y muy especialmente por saber quitarle hierro (o magnesio) a las cosas.